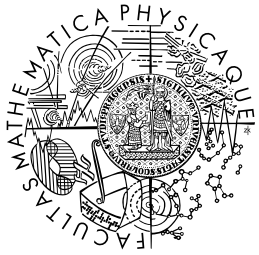

FACULTY
OF MATHEMATICS
AND PHYSICS
Charles University

MASTER THESIS

Bc. Jakub Cach

Viscoelastic rate-type fluids: a study of the effect of stress diffusion by means of numerical simulations

Mathematical Institute of Charles University

Supervisor of the master thesis: RNDr. Karel Tůma, Ph.D.

Study programme: Mathematical and Computational Modelling in Physics (N0533A110020)

Study branch: Mathematical and Computational Modelling in Physics (NFMPMOD20N)

Prague 2023

I declare that I carried out this bachelor thesis independently, and only with the cited sources, literature and other professional sources. It has not been used to obtain another or the same degree.

I understand that my work relates to the rights and obligations under the Act No. 121/2000 Sb., the Copyright Act, as amended, in particular the fact that the Charles University has the right to conclude a license agreement on the use of this work as a school work pursuant to Section 60 subsection 1 of the Copyright Act.

Prague, 3 May 2023 Jakub Cach

I would like to thank the supervisor of my master's thesis, RNDr. Karel Tůma, Ph.D., for his kindness, patience, willingness to consult, and valuable advice and comments.
I am grateful to the consultant of my master's thesis, prof. RNDr. Josef Málek, CSc., DSc., for his invaluable support and guidance. Thank you for your expertise and insightful feedback.

Title: Viscoelastic rate-type fluids: a study of the effect of stress diffusion by means of numerical simulations

Author: Bc. Jakub Cach

Institute: Mathematical Institute of Charles University

Supervisor: RNDr. Karel Tůma, Ph.D., Mathematical Institute of Charles University

Abstract: Describing viscoelastic fluids is a difficult task, as the viscoelastic phenomena are not fully understood. This work follows a method for deriving viscoelastic models that accurately capture the behavior of fluids with polymeric substances, which macroscopically manifest as the stress diffusion, within a consistent thermodynamic framework. We implemented these models using the open-source computing platform FEniCS as a finite element library for Python, and we provide a numerical study of the stress diffusion as a stabilization. By extending our implementation using the arbitrary Lagrangian-Eulerian method, we are able to simulate well-known non-Newtonian phenomena, in particular the Weissenberg effect, demonstrating the effectiveness of our approach in enabling a better understanding of these complex fluids.

Keywords: Viscoelasticity, rate-type fluid, stress diffusion, finite element method, Weissenberg effect.

Contents

Preface

Viscoelastic fluids are complex fluids that exhibit both viscous and elastic behaviors. They are ubiquitous in nature and have a wide range of industrial and biomedical applications. These fluids are characterized by their ability to store and release energy, which gives rise to a variety of non-Newtonian phenomena. Understanding the behavior of viscoelastic fluids is a challenging task, and the development of accurate models of their behavior is an active area of research.

In this work, we follow a consistent thermodynamic framework for which is sufficient to provide only two mentioned informations – how the body stores the energy and how the body dissipates the energy in the form of scalar functions that dependent on the internal variables. This framework has ability to generate plethora of viscoelastic models, which allows us to capture the complex behavior of viscoelastic fluids, for example the stress diffusion, stress relaxation, non-linear creep, or non-zero normal stress differences in a simple shear flow.

We focus on the implementation of viscoelastic models using the finite element method. The finite element method is a numerical technique for solving partial differential equations, and is widely used in the simulation of fluid dynamics problems. Using the open-source computing platform FEniCS as a finite element library for Python, we investigate the effect of the stress diffusion as a stabilization on benchmark flow past the cylinder.

Moreover, we numerically simulate well-known non-Newtonian phenomena in axisymmetric setting. The most complex computation is the simulation of rod-climbing (Weissenberg) effect, for which we use the arbitrary Lagrangian-Eulerian method, the non-symmetric stabilized Nitsche method, and the Implicit Glowinski three-step time scheme. The stress diffusion is not considered in these simulations.

Overall, the work presented in this paper provides an insight for understanding viscoelastic fluids and their behavior, using numerical simulations. It demonstrates that simulations of complex non-Newtonian phenomena in a computationally efficient manner are possible, which makes a contribution to the field of computational fluid dynamics.

1. Continuum mechanics introduction

In this section, we introduce essential concepts for derivation of the variants of rate-type viscoelastic fluid models. We will follow the approach by Rajagopal and Srinivasa [2000], who introduce a notion of natural configuration related to the relaxation mechanisms that viscoelastic materials exhibit, and the approach of Rajagopal and Srinivasa [2004], that uses thermodynamic framework to derive such models consistently with the second law of thermodynamic.

1.1 Kinematic quantities

Let us introduce basic concept of continuum mechanics. As usual, let $t \in [0, T]$ denote time, where $T > 0$ is a fixed constant. Let B denote an abstract three-dimensional body, and for any $t \in [0, T]$ we define $\kappa_t : B \longrightarrow \mathbb{R}^3$ a placer which maps B into the configuration $\kappa_t(B)$, and which is assumed to be one-to-one mapping. Configuration $\kappa_t(B)$ represents a current configuration and $\{\kappa_t\}_{t\in[0,T]}$ is called motion. In behalf of convenience, we identify the initial configuration $\kappa_0(B)$ with the reference configuration $\kappa_R(B)$, see Figure 1.1. Next, we define the so-called deformation mapping $\chi_{\kappa_R} : [0, T] \times \kappa_R(B) \longrightarrow \kappa_t(B)$ by setting:

$$x = \chi_{\kappa_R}(t, X) \quad \text{for } X \in \kappa_R(B) \text{ and } x \in \kappa_t(B). \tag{1.1}$$

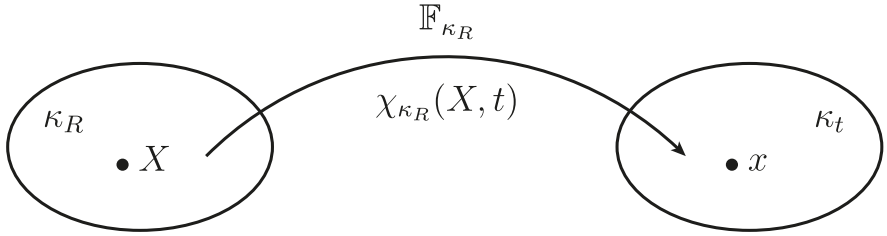

Figure 1.1: Sketch of the reference configuration $\kappa_R(B)$ and the current configuration $\kappa_t(B)$. The deformation gradient $\mathbb{F}_{\kappa_R}$ maps an infinitesimal filament from the $\kappa_R(B)$ to the $\kappa_t(B)$.

Using the deformation mapping, we introduce the Lagrangian velocity $\mathbf{V}$, the (Eulerian) velocity $\mathbf{v}$ and the deformation gradient $\mathbb{F}_{\kappa_R}$:

$$\mathbf{V}(t, X) = \frac{\partial \chi_{\kappa_R}}{\partial t}(t, X), \tag{1.2}$$

$$\mathbf{v}(t, x) = \frac{\partial x}{\partial t} \quad (\iff \mathbf{v} = \mathbf{V}(t, \chi^{-1}_{\kappa_R}(t, x))), \tag{1.3}$$

$$\mathbb{F}_{\kappa_R} = \nabla \chi_{\kappa_R}(t, X). \tag{1.4}$$

Note that the deformation gradient and the velocity gradient $\mathbb{L} := \nabla \mathbf{v}$ are linked through the following relation describing the evolution of $\mathbb{F}_{\kappa_R}$:

$$\mathbb{L} = \dot{\mathbb{F}}_{\kappa_R} \mathbb{F}^{-1}_{\kappa_R} \quad (\iff \dot{\mathbb{F}}_{\kappa_R} = \mathbb{L}\mathbb{F}_{\kappa_R}), \tag{1.5}$$

where we used the definition of the material time derivative, that for an arbitrary scalar function g takes the form:

$$\dot{g} = \frac{\partial g}{\partial t} + \mathbf{v} \cdot \nabla g, \tag{1.6}$$

and for a arbitrary vectorial function $\mathbf{g}$, tensorial function $\mathbb{G}$ respectively, analogical equation holds, i. e., the dot-product term takes the form:

$$(\mathbf{v} \cdot \nabla \mathbf{g})_i = \sum_{j=1}^{3} v_j \frac{\partial g_i}{\partial x_j}, \quad (\mathbf{v} \cdot \nabla \mathbb{G})_{ij} = \sum_{k=1}^{3} v_k \frac{\partial G_{ij}}{\partial x_k} \text{ respectively.} \tag{1.7}$$

Moreover let us introduce symmetric $\mathbb{D}$ and antisymmetric $\mathbb{W}$ parts of $\mathbb{L}$:

$$\mathbb{D} := \frac{1}{2}(\mathbb{L} + \mathbb{L}^T) \quad \text{and} \quad \mathbb{W} := \frac{1}{2}(\mathbb{L} - \mathbb{L}^T), \tag{1.8}$$

where $\mathbb{A}^T$ denotes the transpose of a tensor $\mathbb{A}$, and the left and right Cauchy-Green tensors:

$$\mathbb{B}_{\kappa_R} = \mathbb{F}_{\kappa_R} \mathbb{F}_{\kappa_R}^T \quad \text{and} \quad \mathbb{C}_{\kappa_R} = \mathbb{F}_{\kappa_R}^T \mathbb{F}_{\kappa_R}. \tag{1.9}$$

Using the chain rule, it follows from eq. (1.9) and eq. (1.5) that:

$$\dot{\mathbb{B}}_{\kappa_R} = \dot{\mathbb{F}}_{\kappa_R} \mathbb{F}_{\kappa_R}^T + \mathbb{F}_{\kappa_R} \dot{\mathbb{F}}_{\kappa_R}^T = \mathbb{L}\mathbb{B}_{\kappa_R} + \mathbb{B}_{\kappa_R} \mathbb{L}^T. \tag{1.10}$$

Then by introducing upper convected Oldroyd derivative (which will be later recognized as a member of the class of Gordon-Schowalter derivatives):

$$\overset{\nabla}{\mathbb{B}}_{\kappa_{p(t)}} = \dot{\mathbb{B}}_{\kappa_R} - \mathbb{L}\mathbb{B}_{\kappa_{p(t)}} - \mathbb{B}_{\kappa_{p(t)}} \mathbb{L}^T, \tag{1.11}$$

it is possible to rewrite preceding identity (1.10) as:

$$\overset{\nabla}{\mathbb{B}}_{\kappa_{p(t)}} = \mathbb{O}, \tag{1.12}$$

where $\mathbb{O}$ denotes the zero tensor.

In addition, it follows from eq. (1.10) and eq. (1.8) with the symmetry of $\mathbb{B}_{\kappa_R}$ and the definition of the trace of a tensor $\mathrm{tr}\mathbb{A} := \sum_{i=1}^{3} A_{ii}$ that:

$$\mathrm{tr}\dot{\mathbb{B}}_{\kappa_R} = 2\mathbb{D} \cdot \mathbb{B}_{\kappa_R}. \tag{1.13}$$

1.2 Setting of natural configuration

Let us introduce concept of natural configuration, which can be in words defined as a configuration that the body in the current configuration would take if the external stimuli were removed. Hence the natural configuration $\kappa_{p(t)}(B)$ is associated with the current configuration $\kappa_t(B)$ and it evolves with the body as the body produces entropy. This allows us to split the the total deformation $\mathbb{F}_{\kappa_R}$ into purely elastic (reversible) part $\mathbb{F}_{\kappa_{p(t)}} : \kappa_{p(t)}(B) \longrightarrow \kappa_t(B)$ and the rest (dissipation) $\mathbb{G} : \kappa_R(B) \longrightarrow \kappa_{p(t)}(B)$ so that:

$$\mathbb{F}_{\kappa_R} = \mathbb{F}_{\kappa_{p(t)}} \mathbb{G}, \tag{1.14}$$

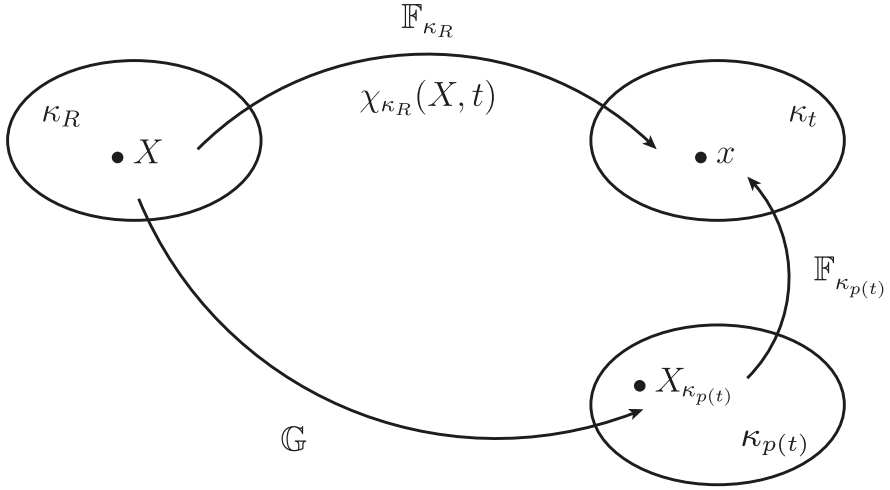

Figure 1.2: Sketch of the reference configuration $\kappa_R(B)$, the current configuration $\kappa_t(B)$ and the natural configuration $\kappa_{p(t)}(B)$. The deformation gradient $\mathbb{F}_{\kappa_R}$ is multiplicatively decomposed.

see Figure 1.2.

Next, we introduce quantities connected with the natural configuration $\kappa_{p(t)}$, see preceding section for comparison. Namely, identity for mapping $\mathbb{G}$ and $\mathbb{F}_{\kappa_{p(t)}}$:

$$\mathbb{G} = \mathbb{F}^{-1}_{\kappa_{p(t)}}\mathbb{F}_{\kappa_R} \quad \text{and} \quad \mathbb{F}_{\kappa_{p(t)}} = \mathbb{F}_{\kappa_R}\mathbb{G}^{-1}. \tag{1.15}$$

Motivated by the relation (1.5) we define the velocity gradient of the natural configuration $\mathbb{L}_{\kappa_{p(t)}}$, its symmetric $\mathbb{D}_{\kappa_{p(t)}}$ and antisymmetric $\mathbb{W}_{\kappa_{p(t)}}$ parts:

$$\mathbb{L}_{\kappa_{p(t)}} = \dot{\mathbb{G}}\mathbb{G}^{-1}, \quad \mathbb{D}_{\kappa_{p(t)}} := \frac{1}{2}(\mathbb{L}_{\kappa_{p(t)}} + \mathbb{L}^T_{\kappa_{p(t)}}), \quad \mathbb{W}_{\kappa_{p(t)}} := \frac{1}{2}(\mathbb{L}_{\kappa_{p(t)}} - \mathbb{L}^T_{\kappa_{p(t)}}), \tag{1.16}$$

the left Cauchy-Green tensor and the right Cauchy-Green tensor:

$$\mathbb{B}_{\kappa_{p(t)}} = \mathbb{F}_{\kappa_{p(t)}}\mathbb{F}^T_{\kappa_{p(t)}} \quad \text{and} \quad \mathbb{C}_{\kappa_{p(t)}} = \mathbb{F}^T_{\kappa_{p(t)}}\mathbb{F}_{\kappa_{p(t)}}. \tag{1.17}$$

In order to compute material time derivative of $\mathbb{B}_{\kappa_{p(t)}}$, we compute a following identity from the eq. (1.5, 1.15, 1.16), the material time derivative of the eq. (1.15) and the material time derivative of the identity $\mathbb{G}\mathbb{G}^{-1} = \mathbb{I}$, where $\mathbb{I}$ stands for the identity tensor:

$$\begin{aligned}
\dot{\mathbb{F}}_{\kappa_{p(t)}} &= \dot{\mathbb{F}}_{\kappa_R}\mathbb{G}^{-1} + \mathbb{F}_{\kappa_R}\dot{\overline{\mathbb{G}^{-1}}} \\
&= \dot{\mathbb{F}}_{\kappa_R}\mathbb{F}^{-1}_{\kappa_R}\mathbb{F}_{\kappa_R}\mathbb{G}^{-1} - \mathbb{F}_{\kappa_R}\mathbb{G}^{-1}\dot{\mathbb{G}}\mathbb{G}^{-1} \\
&= \mathbb{L}\mathbb{F}_{\kappa_{p(t)}} - \mathbb{F}_{\kappa_{p(t)}}\mathbb{L}_{\kappa_{p(t)}}.
\end{aligned} \tag{1.18}$$

Hence by chain rule we obtain:

$$\dot{\mathbb{B}}_{\kappa_{p(t)}} = \dot{\mathbb{F}}_{\kappa_{p(t)}}\mathbb{F}^T_{\kappa_{p(t)}} + \mathbb{F}_{\kappa_{p(t)}}\dot{\mathbb{F}}^T_{\kappa_{p(t)}} = \mathbb{L}\mathbb{B}_{\kappa_{p(t)}} + \mathbb{B}_{\kappa_{p(t)}}\mathbb{L}^T - 2\mathbb{F}_{\kappa_{p(t)}}\mathbb{D}_{\kappa_{p(t)}}\mathbb{F}^T_{\kappa_{p(t)}}, \tag{1.19}$$

which can be expressed with the use of upper convected Oldroyd derivative (1.11) as:

$$\overset{\nabla}{\mathbb{B}}_{\kappa_{p(t)}} = -2\mathbb{F}_{\kappa_{p(t)}}\mathbb{D}_{\kappa_{p(t)}}\mathbb{F}^T_{\kappa_{p(t)}}. \tag{1.20}$$

Note that the setting with only one natural configuration leads to the rate-type fluid models of the first order. To obtain models for materials with multiple relaxation mechanisms, it is necessary to incorporate additional co-existing natural configurations. In the setting with two natural configurations, one can derive variants of the Burgers model for example, see work by Málek et al. [2018] for details.

1.3 Balance equations, thermodynamic framework

Finally in this chapter, we describe thermodynamic framework that will be used in the next chapter to derive variants of rate-type viscoelastic fluid models. We start with the set of balance equations, namely balance of mass:

$$\dot{\rho} = -\rho \operatorname{div} \mathbf{v}, \tag{1.21}$$

balance of linear momentum:

$$\rho \dot{\mathbf{v}} = \operatorname{div} \mathbb{T} + \rho \mathbf{b}, \tag{1.22}$$

balance of angular momentum:

$$\mathbb{T} = \mathbb{T}^T, \tag{1.23}$$

balance of energy:

$$\rho \dot{E} = \operatorname{div} (\mathbb{T}\mathbf{v} - \mathbf{j}_e) + \rho \mathbf{b} \cdot \mathbf{v}, \quad E = e + \frac{|\mathbf{v}|^2}{2}, \tag{1.24}$$

balance of entropy:

$$\rho \dot{\eta} + \operatorname{div} \mathbf{j}_\eta = \zeta, \quad \zeta \geq 0, \tag{1.25}$$

where ρ is the density, $\mathbf{b}$ is the specific density of the given body force, $\mathbb{T}$ is Cauchy stress tensor, e is internal energy, $\mathbf{j}_e$ is the energy flux, η is the entropy, $\mathbf{j}_\eta$ is the entropy flux and ζ is the entropy production.

Let us take further assumptions. Assuming incompressibility, eq. (1.21) reduces to:

$$\operatorname{div} \mathbf{v} = 0. \tag{1.26}$$

Note that in the case of inhomogeneous incompressible fluid, one still need to use the transport equation for the ρ. Moreover, later we will show another approach how to incorporate the incompressibility restriction into the models.

Next, we assume all processes to be isothermal, hence we postulate temperature Θ to be constant and we make special choice of entropy flux $\mathbf{j}_\eta = \mathbf{j}_e/\Theta$. Now, by introducing the Helmholtz free energy $\Psi := e - \Theta\eta$, taking its material derivative and using the balance of energy (1.24) subtracted by (1.22)$\cdot\mathbf{v}$:

$$\begin{aligned} \rho \dot{\Psi} = \rho \dot{e} - \rho\Theta\dot{\eta} = \mathbb{T} \cdot \mathbb{D} - \operatorname{div} \mathbf{j}_e - \rho\Theta\dot{\eta} \\ \iff \rho \dot{\eta} + \operatorname{div} \frac{\mathbf{j}_e}{\Theta} = \frac{1}{\Theta}(\mathbb{T} \cdot \mathbb{D} - \rho \dot{\Psi}), \end{aligned}$$

and comparing to the balance of entropy (1.25), we obtain the reduced thermodynamic identity (RTI):

$$\mathbb{T} \cdot \mathbb{D} - \rho\dot{\Psi} = \xi, \quad \xi = \rho\Theta\zeta \geq 0. \tag{1.27}$$

On the other hand, without special choice of the entropy flux, one can obtain the general form of the reduced thermodynamic identity:

$$\mathbb{T} \cdot \mathbb{D} - \rho\dot{\Psi} - \operatorname{div}(\mathbf{j}_e - \Theta\mathbf{j}_\eta) = \xi, \quad \xi = \rho\Theta\zeta \geq 0. \tag{1.28}$$

Therefore one of these identities together with balance of mass (1.21), balance of linear (1.22) and angular (1.23) momentum create a new set of the balance equations.

Also note that the assumption on a constant temperature is in contradiction with the heating due to the non-zero dissipation. Nevertheless, we can assume that the heat capacity of the body is large enough to ensure temperature changes to be insignificant or we can assume that the thermal conductivity of the body is large enough so that the dissipated energy (heat) is taken out instantaneously from the body into an external thermal reservoir surrounding the body.

Lastly, to outline derivation of the models in the next chapter, we will proceed accordingly to the following framework. To the set of the balance equations, we add assumption on how the material stores the energy by prescribing the Helmholtz free energy in the form:

$$\Psi = \widetilde{\Psi}(y_1, \ldots, y_n), \tag{1.29}$$

where $y_1, \ldots, y_n$ are the state variables. Then substituting the chosen energy (1.29) into the reduced thermodynamic identity (1.27), we arrive at the following equality:

$$\xi = \sum_{\alpha=1}^{k} J_\alpha A_\alpha, \tag{1.30}$$

where J_α stands for the terms that can be identified as thermodynamic fluxes, A_α stands for the terms that can be identified as thermodynamic affinities and each of the summands $J_1A_1, \ldots, J_kA_k$ represents a different dissipative mechanism. The term $\mathbb{T} : \mathbb{D}$ from the eq. (1.27) is also included in the sum.

Now, we add assumption on how the material dissipates the energy, which gives a full model and closes the system of equations. In order to satisfy restriction $\xi \geq 0$, we can proceed in two ways. We postulate the constitutive assumption on the rate of entropy production in the form:

$$\xi = \widetilde{\xi}(J_1, \ldots, J_k) \geq 0 \quad \text{or} \quad \xi = \widetilde{\xi}(A_1, \ldots, A_k) \geq 0, \tag{1.31}$$

Firstly, we can ensure that every product $J_\alpha A_\alpha, \alpha = 1, \ldots, k$ is non-negative based on comparison with the prescribed $\widetilde{\xi}$ by J_α, which then determines the constitutive equation for the Cauchy stress tensor $\mathbb{T}$. Secondly, we obtain the constitutive equation for the Cauchy stress tensor $\mathbb{T}$ by using assumption on maximization of $\widetilde{\xi}_{J_1,\ldots,J_k}(A_1, \ldots, A_k)$ with respect to $A_1, \ldots, A_k$ provided that $\widetilde{\xi}_{J_1,\ldots,J_k}(A_1, \ldots, A_k) - \sum_{\alpha=1}^{k} J_\alpha A_\alpha = 0$. If the prescribed $\widetilde{\xi}$ is quadratic in affinities $A_\alpha, \alpha = 1, \ldots, k$, then both procedures gives the same equation for tensor $\mathbb{T}$.

Note that the last assumption of maximization says that the body dissipates the energy in the fastest possible way. Moreover, one can prescribe entropy production in fluxes and maximize with respect to fluxes, since the expression is symmetric to the interchange of fluxes and affinities.

2. Derivation of the variants of the Oldroyd-B model with stress diffusion

In this chapter we derive classical Oldroyd-B model, presented by Oldroyd [1950], using mechanical analogs and discuss imperfections of such derivation. Then we derive variant of the Oldroyd-B model by the approach mentioned in the preceding chapter, following work of Málek et al. [2018]. And finally we derive generalized model with **stress diffusion** containing convex combination of Oldroyd-B and Giesekus model, which was proposed in work by Bathory et al. [2020].

2.1 Classical Oldroyd-B model due to the mechanical analog

To derive classical Oldroyd-B model in one spatial dimension one can use the mechanical analogs, which are mechanical systems consisting of springs and dashpots. On the one hand, spring characterizes the elasticity of the material well and describes reversible deformation. On the other hand, dashpot characterizes viscosity of the material well and describes irreversible (dissipative) deformation. From parallel and serial connection of such elements, one can obtain a plethora of models describing non-Newtonian phenomena such as stress relaxation, nonlinear creep or presence of non-zero normal stress differences in a simple shear flow (Phenomenas, that classical Oldroyd-B model is able to describe.). Note that this method leads to the stress-strain relations that are in the form of differential equations of arbitrary order.

We use combination of elements described in the Figure 2.1, that is a spring of the shear modulus G and a dashpot of the viscosity μ_2 on the lower branch (B) in a serial connection, and a dashpot of the viscosity μ_1 on the upper branch (A) connected in parallel to the first branch. Such mechanical analog must satisfy following conditions due to a basic physics: shear rate $\dot{\varepsilon}$ of the both branches is the same, total shear stress σ is a sum of stresses at each branch, displacement on each branch is a sum of displacements of elements located on that branch.

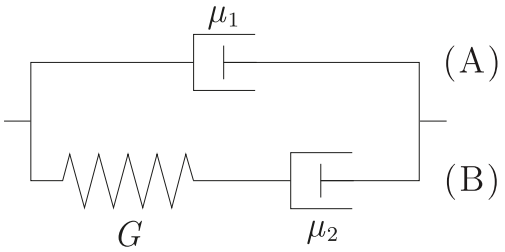

Figure 2.1: Mechanical analog for the classical Oldroyd-B model consisting of three elements located on the branches (A) and (B). Note that branch (B) correspond to the Mawxell element.

Preceeding physical conditions can be written in the same order as:

$$\dot{\varepsilon} = \dot{\varepsilon}_A = \dot{\varepsilon}_B, \tag{2.1}$$

$$\sigma = \sigma_A + \sigma_B, \tag{2.2}$$

$$\varepsilon_B = \varepsilon_{el,B} + \varepsilon_{vis,B}, \tag{2.3}$$

where subscript A, B coincide with the labels of branches (A), (B), subscript *el* refers to a spring and subscript *vis* refers to a dashpot. Basic relations that spring and dashpot for (incompressible) material satisfy:

$$\sigma = G\varepsilon, \tag{2.4}$$

$$\sigma = \mu\dot{\varepsilon}. \tag{2.5}$$

Now, we obtain model for each branch separately. Using condition (2.3), relations (2.4) and (2.5) modified for the branch (B), we obtain a well-known relation for the Maxwell element:

$$\sigma_B + \frac{\mu_2}{G}\dot{\sigma}_B = \mu_2\dot{\varepsilon}_B. \tag{2.6}$$

Also, we get simple a relation for dashpot modified for branch (A):

$$\sigma_A = \mu_1\dot{\varepsilon}_A. \tag{2.7}$$

Next, we use derivation trick proposed by Wineman and Rajagopal [2000]. We use condition (2.1) and formally rewrite obtained equation for each branch:

$$\left(1 + \frac{\mu_2}{G}\frac{d}{dt}\right) \cdot \sigma_B = \mu_2\dot{\varepsilon}, \tag{2.8}$$

$$1 \cdot \sigma_A = \mu_1\dot{\varepsilon}, \tag{2.9}$$

in the sense of differential operators. Finally, the last unused condition (2.2) dictates how to multiply each equation and sum them together. Hence we aplly differential operator from the left (2.9)$\cdot(1 + \frac{\mu_2}{G}\frac{d}{dt})$ and (2.8)$\cdot 1$, obtaining:

$$\left(1 + \frac{\mu_2}{G}\frac{d}{dt}\right) \cdot (\sigma_B + \sigma_B) = (\mu_1 + \mu_2)\dot{\varepsilon} + \frac{\mu_1\mu_2}{G}\ddot{\varepsilon}, \tag{2.10}$$

leading to the stress-strain relation for the Oldroyd-B model:

$$\sigma + \frac{\mu_2}{G}\dot{\sigma} = (\mu_1 + \mu_2)\dot{\varepsilon} + \frac{\mu_1\mu_2}{G}\ddot{\varepsilon}, \tag{2.11}$$

that is a first order differential equation for total shear stress and shear rate.

To generalize such model to three spatial dimensions, we identify shear stress σ as the Cauchy stress tensor $\mathbb{T}$ and the time derivative of shear rate as two times the symmetric part of the velocity gradient $\mathbb{D}$, motivated by the relations for the simple shear flow. Now, we need to take one more time derivative of these quantities, however material time derivative applied on such quantities is

not an objective quantity, as a quantity is objective if it transforms as: $s^* = s$, $\mathbf{w}^* = \mathbb{Q}(t)\mathbf{w}$, $\mathbb{U}^* = \mathbb{Q}(t)\mathbb{U}\mathbb{Q}^T(t)$, where superscript s^* denotes the euclidean change of observer, and $\mathbb{Q} : \mathbb{R} \to \mathrm{SO}(3)$. Hence, we use upper convected Oldroyd derivative, that is a special case ($a = 1$) of the Gordon-Schowalter family of objective derivatives:

$$\frac{\delta \mathbb{A}}{\delta t} := \dot{\mathbb{A}} - a(\mathbb{D}\mathbb{A} + \mathbb{A}\mathbb{D}) - (\mathbb{W}\mathbb{A} - \mathbb{A}\mathbb{W}), \quad a \in [-1, 1], \tag{2.12}$$

as it has favourable physical properties. But in principle, arbitrary member of the Gordon-Schowalter family could been used. That is why the generalization is not unique and is not suitable. Moreover, throughout the derivation it is not obvious that the model satisfies the second law of thermodynamics. Hence the derivation with the use of thermodynamic framework is preferred.

2.2 Variant of the Oldroyd-B model

In this section we derive variant of the Oldroyd-B model by following thermodynamic framework described in the preceeding chapter. This model includes models such as Maxwell model, Giesekus model and classical Oldroyd-B model as its special cases. Hence this derivation also shows hierarchy of viscoelastic models. Based on that, in the next section, we obtain Oldroyd-B model with stress diffusion by modification of the following procedure.

First of all, let us emphasise, that we derive an incompressible model, meaning that the whole deformation is isochoric, which was expressed by eq.(1.26):

$$\operatorname{div} \mathbf{v} = \operatorname{tr}\mathbb{D} = 0 \quad \text{and} \quad \det\mathbb{F}_{\kappa_R} = 1. \tag{2.13}$$

However, by the discussion of an instanteneous response of viscoelastic material by Málek et al. [2015], we suppose that splitted deformations $\mathbb{F}_{\kappa_{p(t)}}$ and $\mathbb{G}$ due to the natural configuration $\kappa_{p(t)}$ do not have to be isochoric, in other words, these deformations do not necessarily fulfill $\det\mathbb{F}_{\kappa_{p(t)}} = 1 = \det\mathbb{G}$.

Next, we assume that the energy of elastic deformation $\mathbb{F}_{\kappa_{p(t)}}$ corresponds to the compressible neo-Hookean solid:

$$\Psi(\mathbb{B}_{\kappa_{p(t)}}) = \frac{G}{2\rho}(\operatorname{tr}\mathbb{B}_{\kappa_{p(t)}} - 3 - \ln(\det \mathbb{B}_{\kappa_{p(t)}})), \tag{2.14}$$

where G is the elastic modulus. According to the framework, we insert this energy to the reduced thermodynamic identity (1.27), and using identity that can be found for example in Appendix A in the paper by Málek et al. [2015] (first equality):

$$\overline{\ln(\det \mathbb{B}_{\kappa_{p(t)}})} = \operatorname{tr}(\dot{\mathbb{B}}_{\kappa_{p(t)}}\mathbb{B}^{-1}_{\kappa_{p(t)}}) \overset{(1.11)}{=} 2\operatorname{tr}\mathbb{D} - 2\operatorname{tr}\mathbb{D}_{\kappa_{p(t)}}, \tag{2.15}$$

we obtain:

$$\begin{aligned} \xi = \mathbb{T} : \mathbb{D} - \rho\dot{\Psi} &= (\mathbb{T} - G\mathbb{B}_{\kappa_{p(t)}} + \mathbb{I}) : \mathbb{D} - (\mathbb{C}_{\kappa_{p(t)}} - \mathbb{I}) : \mathbb{D}_{\kappa_{p(t)}} \\ &\overset{(2.13)}{=} (\mathbb{T} - G\mathbb{B}_{\kappa_{p(t)}})^d : \mathbb{D}^d - (\mathbb{C}_{\kappa_{p(t)}} - \mathbb{I}) : \mathbb{D}_{\kappa_{p(t)}}, \end{aligned} \tag{2.16}$$

where we used incompressibility condition for the full deformation and following identity for the deviatoric parts $\mathbb{A} : \mathbb{D} = (\mathbb{A}^d + \frac{1}{3}(\mathrm{tr}A)\mathbb{I}) : (\mathbb{D}^d + (\mathrm{tr}\mathbb{D})\mathbb{I}) = \mathbb{A}^d : \mathbb{D}^d$ that also uses the incompressibility.

Let us now consider rate of entropy production $\widetilde{\xi}$ given by:

$$\widetilde{\xi}(\mathbb{D}, \mathbb{D}_{\kappa_{p(t)}}, \mathbb{C}_{\kappa_{p(t)}}) = 2\mu_2|\mathbb{D}^d|^2 + 2\mu_1 \mathbb{D}_{\kappa_{p(t)}} \mathbb{C}^{\lambda}_{\kappa_{p(t)}} : \mathbb{D}_{\kappa_{p(t)}}, \quad \mu_1, \mu_2 > 0, \lambda \geq 0, \tag{2.17}$$

where $\mu := \mu_1 + \mu_2$ is total viscosity of the material consisting of viscosities of polymeric and solvent components. Note that it holds $2\mu_1 \mathbb{D}_{\kappa_{p(t)}} \mathbb{C}^{\lambda}_{\kappa_{p(t)}} : \mathbb{D}_{\kappa_{p(t)}} = |\mathbb{D}_{\kappa_{p(t)}} \mathbb{U}^{\lambda}_{\kappa_{p(t)}}|^2$, where $\mathbb{U}_{\kappa_{p(t)}}$ comes from the polar decomposition of the deformation gradient $\mathbb{F}_{\kappa_{p(t)}} = \mathbb{R}_{\kappa_{p(t)}} \mathbb{U}_{\kappa_{p(t)}}$. Hence $\widetilde{\xi}$ is quadratic in affinities.

Finally, by comparison of the term with $\mathbb{D}$ in eq. (2.16) and eq. (2.17) we obtain:

$$\mathbb{T}^d = 2\mu_2 \mathbb{D}^d + G\mathbb{B}^d_{\kappa_{p(t)}}. \tag{2.18}$$

Hence by definition of deviatoric part $\mathbb{T} = -m\mathbb{I} + \mathbb{T}^d$ we get the constitutive equation for the Cauchy stress tensor $\mathbb{T}$:

$$\boxed{\mathbb{T} = -\phi\mathbb{I} + 2\mu_2 \mathbb{D}^d + G(\mathbb{B}^d_{\kappa_{p(t)}} - \mathbb{I}), \quad \phi = -(m - G\frac{\mathrm{tr}\mathbb{B}_{\kappa_{p(t)}}}{3}).} \tag{2.19}$$

Furhermore, comparing of the term with $\mathbb{D}$ in eq. (2.16) and eq. (2.17) leads to:

$$G(\mathbb{C}_{\kappa_{p(t)}} - \mathbb{I}) = 2\mu_1 \mathbb{D}_{\kappa_{p(t)}} \mathbb{C}^{\lambda}_{\kappa_{p(t)}}. \tag{2.20}$$

Now, multiplying this equation by $\mathbb{F}_{\kappa_{p(t)}}$ from the left and by $\mathbb{U}^{1-2\lambda}_{\kappa_{p(t)}} \mathbb{R}^T_{\kappa_{p(t)}}$ from the right, where we identify $\overset{\nabla}{\mathbb{B}}_{\kappa_{p(t)}}$, we obtain desired rate-type equation:

$$\boxed{\overset{\nabla}{\mathbb{B}}_{\kappa_{p(t)}} + \frac{G}{\mu_1}(\mathbb{B}_{\kappa_{p(t)}} - \mathbb{I})\mathbb{B}^{1-\lambda}_{\kappa_{p(t)}} = \mathbb{O}.} \tag{2.21}$$

Note that the case $\lambda = 0$ corresponds to the Giesekus model and case $\lambda = 1$ corresponds to the Oldroyd-B model, Maxwell model respectively, depending on whether μ_2 is positive or zero respectively.

2.3 Convex combination of the Oldroyd-B and Giesekus model with stress diffusion

Motivied by the derivation in the preceeding section, where it was sufficient to provide only two scalar functions to obtain the model, now we obtain convex combination of Oldroyd-B and Giesekus model with **stress diffusion**. To achieve it, we modify the first of scalar functions – the Helmholtz free energy Ψ. Then we prescribe rate-type equation with stress diffusion that we desire. This is a change of thinking compared to the preceeding procedure. However, immediately afterwards we verify validity of the second law of thermodynamic, and if one would like to obtain the second scalar function – the rate of entropy production, it can be read from this verification.

We postulate a modified constitutive equation for the Helmholtz free energy for the compressible neo-Hookean solid:

$$\Psi(\mathbb{B}_{\kappa_{p(t)}}) = \mu((1-\beta)(\mathrm{tr}\mathbb{B}_{\kappa_{p(t)}} - 3 - \ln(\det \mathbb{B}_{\kappa_{p(t)}})) + \frac{1}{2}\beta|\mathbb{B}_{\kappa_{p(t)}} - \mathbb{I}|^2), \tag{2.22}$$

where $\beta \in [0,1]$ is a parameter interpolating between two forms of the energy and one can identify constant $\mu = G/2\rho$ by comparison with the previous model if needed. The last newly introduced term $\frac{1}{2}\beta|\mathbb{B}_{\kappa_{p(t)}} - \mathbb{I}|^2$ depends only on the invariants of $\mathbb{B}_{\kappa_{p(t)}}$ and hence can be considered consistently with the principles of continuum thermodynamic. Furthermore, on the logaritmic scale in the asymptotic expansion of Ψ near $\mathbb{I}$ the last term does not effect the original form of the energy. For the full explanation of the new term, follow the work by Bathory et al. [2020].

Let us now add the last piece of information needed to derive this model, as was discussed above. Motivated by eq. (2.21), we postulate rate-type equation in the form:

$$\boxed{\frac{\delta \mathbb{B}_{\kappa_{p(t)}}}{\delta t} + \delta_1(\mathbb{B}_{\kappa_{p(t)}} - \mathbb{I}) + \delta_2(\mathbb{B}^2_{\kappa_{p(t)}} - \mathbb{B}_{\kappa_{p(t)}}) = \lambda \Delta \mathbb{B}_{\kappa_{p(t)}},} \tag{2.23}$$

where $\lambda > 0$, δ_1, $\delta_2 \geq 0$ are parameters and Gordon-Schowalter objective derivative (2.12) is used.

Next, we insert energy Ψ into the the general form of the reduced thermodynamic identity (1.28), as we will assume another relation for the entropy flux, which will naturaly arrise from the derivation. To evaluate it, we rewrite rate-type equation (2.23) as:

$$\begin{aligned} -\dot{\mathbb{B}}_{\kappa_{p(t)}} =& -\lambda \Delta \mathbb{B}_{\kappa_{p(t)}} - (\mathbb{W}\mathbb{B}_{\kappa_{p(t)}} - \mathbb{B}_{\kappa_{p(t)}}\mathbb{W}) + a(\mathbb{D}\mathbb{B}_{\kappa_{p(t)}} + \mathbb{B}_{\kappa_{p(t)}}\mathbb{D}) \\ &+ \delta_1(\mathbb{B}_{\kappa_{p(t)}} - \mathbb{I}) + \delta_2(\mathbb{B}^2_{\kappa_{p(t)}} - \mathbb{B}_{\kappa_{p(t)}}), \end{aligned} \tag{2.24}$$

and following the chain rule $\dot{\Psi} = \partial \Psi(\mathbb{B}_{\kappa_{p(t)}})/\partial \mathbb{B}_{\kappa_{p(t)}} \cdot \dot{\mathbb{B}}_{\kappa_{p(t)}}$ we compute:

$$\frac{\partial \Psi(\mathbb{B}_{\kappa_{p(t)}})}{\partial \mathbb{B}_{\kappa_{p(t)}}} = \mu(1-\beta)(\mathbb{I} - \mathbb{B}^{-1}_{\kappa_{p(t)}}) + \mu\beta(\mathbb{B}_{\kappa_{p(t)}} - \mathbb{I}) =: \mathbb{J}. \tag{2.25}$$

Therefore from the Green's first identity for tensors, we obtain:

$$\begin{aligned} -\dot{\Psi} =& a(\mathbb{D}\mathbb{B}_{\kappa_{p(t)}} + \mathbb{B}_{\kappa_{p(t)}}\mathbb{D}) \cdot \mathbb{J} + \delta_1(\mathbb{B}_{\kappa_{p(t)}} - \mathbb{I}) \cdot \mathbb{J} + \delta_2(\mathbb{B}^2_{\kappa_{p(t)}} - \mathbb{B}_{\kappa_{p(t)}}) \cdot \mathbb{J} \\ &- \lambda \Delta \mathbb{B}_{\kappa_{p(t)}} \cdot \mathbb{J} - (\mathbb{W}\mathbb{B}_{\kappa_{p(t)}} - \mathbb{B}_{\kappa_{p(t)}}\mathbb{W}) \cdot \mathbb{J} \\ =& a(\mathbb{D}\mathbb{B}_{\kappa_{p(t)}} + \mathbb{B}_{\kappa_{p(t)}}\mathbb{D}) \cdot \mathbb{J} + \delta_1(\mathbb{B}_{\kappa_{p(t)}} - \mathbb{I}) \cdot \mathbb{J} + \delta_2(\mathbb{B}^2_{\kappa_{p(t)}} - \mathbb{B}_{\kappa_{p(t)}}) \cdot \mathbb{J} \\ &- \lambda \,\mathrm{div}\,(\nabla \Psi(\mathbb{B}_{\kappa_{p(t)}})) + \lambda \nabla \mathbb{B}_{\kappa_{p(t)}} \cdot \nabla \mathbb{J}, \end{aligned} \tag{2.26}$$

where $\nabla \Psi(\mathbb{B}_{\kappa_{p(t)}}) = \mathbb{J} \cdot \nabla \mathbb{B}_{\kappa_{p(t)}}$ and skew-symmetric tensor $\mathbb{W}$ vanishes due to the obvious relation $\mathbb{B}_{\kappa_{p(t)}}\mathbb{J} = \mathbb{J}\mathbb{B}_{\kappa_{p(t)}}$. Now, we simplify each term from the last equality. Starting with:

$$\begin{aligned} (\mathbb{B}_{\kappa_{p(t)}} - \mathbb{I}) \cdot \mathbb{J} =& \mu(1-\beta)(\mathbb{B}^{\frac{1}{2}}_{\kappa_{p(t)}}(\mathbb{B}^{\frac{1}{2}}_{\kappa_{p(t)}} - \mathbb{B}^{-\frac{1}{2}}_{\kappa_{p(t)}})) \cdot (\mathbb{B}^{-\frac{1}{2}}_{\kappa_{p(t)}}(\mathbb{B}^{\frac{1}{2}}_{\kappa_{p(t)}} - \mathbb{B}^{-\frac{1}{2}}_{\kappa_{p(t)}})) \\ &+ \mu\beta(\mathbb{B}_{\kappa_{p(t)}} - \mathbb{I}) \cdot (\mathbb{B}_{\kappa_{p(t)}} - \mathbb{I}) \\ =& \mu(1-\beta)|\mathbb{B}^{\frac{1}{2}}_{\kappa_{p(t)}} - \mathbb{B}^{-\frac{1}{2}}_{\kappa_{p(t)}}|^2 + \mu\beta|\mathbb{B}_{\kappa_{p(t)}} - \mathbb{I}|^2, \end{aligned} \tag{2.27}$$

where we used symmetry, positive definiteness of the matrix $\mathbb{B}_{\kappa_{p(t)}}$ and identity $(\mathbb{A}\mathbb{B})\cdot(\mathbb{A}^{-1}\mathbb{B}) = A_{ij}(A^{-1})_{il}B_{jk}B_{lk} = |\mathbb{B}|^2$, where $\mathbb{A}$, $\mathbb{B}$ are arbitrary tensors. Hence in the same manner we obtain:

$$(\mathbb{B}^2_{\kappa_{p(t)}} - \mathbb{B}_{\kappa_{p(t)}}) \cdot \mathbb{J} = \mu(1-\beta)|\mathbb{B}_{\kappa_{p(t)}} - \mathbb{I}|^2 + \mu\beta|\mathbb{B}^{\frac{3}{2}}_{\kappa_{p(t)}} - \mathbb{B}^{\frac{1}{2}}_{\kappa_{p(t)}}|^2, \tag{2.28}$$

$$\begin{aligned}\nabla\mathbb{B}_{\kappa_{p(t)}} \cdot \nabla\mathbb{J} &= \mu\beta|\nabla\mathbb{B}_{\kappa_{p(t)}}|^2 - \mu(1-\beta)\nabla\mathbb{B}_{\kappa_{p(t)}} \cdot \nabla\mathbb{B}^{-1}_{\kappa_{p(t)}} \\ &= \mu\beta|\nabla\mathbb{B}_{\kappa_{p(t)}}|^2 + \mu(1-\beta)\nabla\mathbb{B}_{\kappa_{p(t)}} \cdot (\mathbb{B}^{-1}_{\kappa_{p(t)}}(\nabla\mathbb{B}_{\kappa_{p(t)}})\mathbb{B}^{-1}_{\kappa_{p(t)}}) \\ &= \mu\beta|\nabla\mathbb{B}_{\kappa_{p(t)}}|^2 + \mu(1-\beta)|\mathbb{B}^{-\frac{1}{2}}_{\kappa_{p(t)}}(\nabla\mathbb{B}_{\kappa_{p(t)}})\mathbb{B}^{-\frac{1}{2}}_{\kappa_{p(t)}}|^2,\end{aligned} \tag{2.29}$$

$$a(\mathbb{D}\mathbb{B}_{\kappa_{p(t)}} + \mathbb{B}_{\kappa_{p(t)}}\mathbb{D}) \cdot \mathbb{J} = 2a\mu\left((1-\beta)(\mathbb{B}_{\kappa_{p(t)}} - \mathbb{I}) + \beta(\mathbb{B}^2_{\kappa_{p(t)}} - \mathbb{B}_{\kappa_{p(t)}})\right) \cdot \mathbb{D}. \tag{2.30}$$

Finally using eq. (2.26), ..., (2.30) with the general form of the reduced thermodynamic identity (1.28), we obtain the rate of entropy production:

$$\begin{aligned}\xi = &- \operatorname{div}(\lambda\nabla\Psi(\mathbb{B}_{\kappa_{p(t)}}) + \mathbf{j}_e - \Theta\mathbf{j}_\eta) \\ &+ \left[\mathbb{T} - 2a\mu\left((1-\beta)(\mathbb{B}_{\kappa_{p(t)}} - \mathbb{I}) + \beta(\mathbb{B}^2_{\kappa_{p(t)}} - \mathbb{B}_{\kappa_{p(t)}})\right)\right] \cdot \mathbb{D} \\ &+ \mu\lambda\left(\beta|\nabla\mathbb{B}_{\kappa_{p(t)}}|^2 + (1-\beta)|\mathbb{B}^{-\frac{1}{2}}_{\kappa_{p(t)}}(\nabla\mathbb{B}_{\kappa_{p(t)}})\mathbb{B}^{-\frac{1}{2}}_{\kappa_{p(t)}}|^2\right) \\ &+ \mu\left((1-\beta)\delta_1|\mathbb{B}^{\frac{1}{2}}_{\kappa_{p(t)}} - \mathbb{B}^{-\frac{1}{2}}_{\kappa_{p(t)}}|^2 + \beta\delta_2|\mathbb{B}^{\frac{3}{2}}_{\kappa_{p(t)}} - \mathbb{B}^{\frac{1}{2}}_{\kappa_{p(t)}}|^2\right) \\ &+ \mu((1-\beta)\delta_2 + \beta\delta_1)|\mathbb{B}_{\kappa_{p(t)}} - \mathbb{I}|^2.\end{aligned} \tag{2.31}$$

To ensure the rate of entropy production to be non-negative, we assume entropy flux to satisfy:

$$\lambda\nabla\Psi(\mathbb{B}_{\kappa_{p(t)}}) + \mathbf{j}_e - \Theta\mathbf{j}_\eta = 0, \tag{2.32}$$

and we set

$$\boxed{\mathbb{T} = -m\mathbb{I} + 2\nu\mathbb{D} + 2a\mu((1-\beta)(\mathbb{B}_{\kappa_{p(t)}} - \mathbb{I}) + \beta(\mathbb{B}^2_{\kappa_{p(t)}} - \mathbb{B}_{\kappa_{p(t)}}))}, \tag{2.33}$$

where ν is a parameter and corresponds to the dynamic viscosity. Hence, using $\mathbb{I}\cdot\mathbb{D} = \operatorname{tr}\mathbb{D} = \operatorname{div}\mathbf{v} = 0$ (2.13), the rate of entropy production takes the form:

$$\begin{aligned}\xi = &2\nu|\mathbb{D}|^2 + \mu\lambda\left(\beta|\nabla\mathbb{B}_{\kappa_{p(t)}}|^2 + (1-\beta)|\mathbb{B}^{-\frac{1}{2}}_{\kappa_{p(t)}}(\nabla\mathbb{B}_{\kappa_{p(t)}})\mathbb{B}^{-\frac{1}{2}}_{\kappa_{p(t)}}|^2\right) \\ &+ \mu\left((1-\beta)\delta_1|\mathbb{B}^{\frac{1}{2}}_{\kappa_{p(t)}} - \mathbb{B}^{-\frac{1}{2}}_{\kappa_{p(t)}}|^2 + \beta\delta_2|\mathbb{B}^{\frac{3}{2}}_{\kappa_{p(t)}} - \mathbb{B}^{\frac{1}{2}}_{\kappa_{p(t)}}|^2\right) \\ &+ \mu((1-\beta)\delta_2 + \beta\delta_1)|\mathbb{B}_{\kappa_{p(t)}} - \mathbb{I}|^2.\end{aligned} \tag{2.34}$$

Clearly, the rate of entropy production in non-negative and the derived model is compatible with the second law of thermodynamic.

3. Weak formulation and Finite element method

In this chapter, we introduce coupled equations with initial and boundary conditions decribing homogeneous incompressible rate-type viscoelastic fluids with **stress diffusion** (model derived in the Section 2.3) flowing in a closed three-dimensional container. Then, following work by Bathory et al. [2020], we show an energy inequality, state a weak formulation and a existence theory theorem of such equations. Existence theory can be obtained due to the presence of stress-diffusive term and plays important role in the numerical simulations. However, later we will use configurations with inflow and outflow, which violate considered boundary conditions in the theory. Moreover, we will use weak formulation containing pressure. Nevertheless, other assumptions of the theorem remain valid. At the end of the section, we introduce basics of finite element method.

3.1 Definition of a closed system of equations

Let us start with the definition of the notation. For a bounded domain $\Omega \subset \mathbb{R}^3$ with the Lipschitz-continuous boundary $\partial\Omega$ and a finite time interval of the length $T > 0$, we define the time-space cylinder $Q := (0,T) \times \Omega$ and we set $\Sigma := (0,T) \times \partial\Omega$ as a part of its boundary. The symbol $\mathbf{n}$ denotes the outward unit normal vector on $\partial\Omega$ and, for arbitrary vector $\mathbf{z}$, the vector $\mathbf{z}_\tau$ denotes the projection of the vector to a tangent plane on $\partial\Omega$, which can be formulated as $\mathbf{z}_\tau := \mathbf{z} - (\mathbf{z}\cdot\mathbf{n})\mathbf{n}$. Then, for a given specific density of the given body forces $f : Q \longrightarrow \mathbb{R}^3$, a given initial velocity $\mathbf{v}_0 : \Omega \longrightarrow \mathbb{R}^3$ and a given initial extra stress tensor $\mathbb{B}_{\kappa_{p(t)},0} : \Omega \longrightarrow \mathbb{R}^{3\times3}_{>0}$ (where $\mathbb{R}^{3\times3}_{>0}$ denotes the set of symmetric positive definite (3×3)-matrices), we look for a vector field $\mathbf{v} : Q \longrightarrow \mathbb{R}^3$, a scalar field $p : Q \longrightarrow \mathbb{R}$ and a positive definite matrix field $\mathbb{B}_{\kappa_{p(t)}} : Q \longrightarrow \mathbb{R}^{3\times3}_{>0}$ solving the following system in Q:

$$\begin{aligned}
\operatorname{div}\mathbf{v} &= 0,\\
\rho\dot{\mathbf{v}} &= \operatorname{div}\mathbb{T} + \mathbf{b},\\
\mathbb{T} &= -p\mathbb{I} + 2\nu\mathbb{D} + 2a\mu((1-\beta)(\mathbb{B}_{\kappa_{p(t)}} - \mathbb{I}) + \beta(\mathbb{B}^2_{\kappa_{p(t)}} - \mathbb{B}_{\kappa_{p(t)}})),\\
\frac{\delta\mathbb{B}_{\kappa_{p(t)}}}{\delta t} &= -\delta_1(\mathbb{B}_{\kappa_{p(t)}} - \mathbb{I}) - \delta_2(\mathbb{B}^2_{\kappa_{p(t)}} - \mathbb{B}_{\kappa_{p(t)}}) + \lambda\Delta\mathbb{B}_{\kappa_{p(t)}},
\end{aligned} \tag{3.1}$$

which consists of the balance of mass (1.26), the balance of linear momentum (1.22), the constitutive law for the Cauchy stress tensor (2.33) and the rate-type equation with stress diffusion (2.23). Note that for the sake of simlicity, in this chapter we set $\rho = 1$. This system is completed by the following boundary conditions on Σ:

$$\begin{aligned}
\mathbf{v}\cdot\mathbf{n} &= 0,\\
(\mathbb{T}\mathbf{n})_\tau &= -\sigma\mathbf{v}_\tau,\\
(\mathbf{n}\cdot\nabla)\mathbb{B}_{\kappa_{p(t)}} &= \mathbb{O},
\end{aligned} \tag{3.2}$$

where $\sigma > 0$ is a parameter of the Navier slip boundary condition that allows more comprehensive description of the boundary interaction, and by the initial conditions in Ω:

$$\begin{aligned} \mathbf{v}(0,\cdot) &= \mathbf{v}_0, \\ \mathbb{B}_{\kappa_{p(t)}}(0,\cdot) &= \mathbb{B}_{\kappa_{p(t)},0}. \end{aligned} \tag{3.3}$$

3.2 Formal a priori estimates

To identify suitable spaces for the proper concept of weak solution, we show the basic energy estimates. By taking scalar product of velocity with the balance of linear momentum (1.22)$\cdot\mathbf{v}$, we obtain kinetic energy identity:

$$\frac{1}{2}\frac{\partial|\mathbf{v}|^2}{\partial t} + \frac{1}{2}\operatorname{div}(|\mathbf{v}|^2\mathbf{v}) - \operatorname{div}(\mathbb{T}\mathbf{v}) - \mathbb{T}\cdot\mathbb{D} = \mathbf{b}\cdot\mathbf{v}, \tag{3.4}$$

where we used symmetry of $\mathbb{T}$, identity $\operatorname{div}(\mathbb{T}\mathbf{v}) = \mathbf{v}\cdot\operatorname{div}\mathbb{T} + \mathbb{T}\cdot\mathbb{L}$ and identity with incompressibility condition (1.26): $\operatorname{div}(|\mathbf{v}|^2\mathbf{v})/2 = (\mathbf{v}\cdot\nabla\mathbf{v})\cdot\mathbf{v} + |\mathbf{v}|^2\operatorname{div}(\mathbf{v})/2 = (\mathbf{v}\cdot\nabla\mathbf{v})\cdot\mathbf{v}$. Now, using general form of the reduced thermodynamic identity (1.28), and assumption on fluxes (2.32), we obtain:

$$\frac{\partial}{\partial t}\left(\Psi + \frac{1}{2}|\mathbf{v}|^2\right) + \operatorname{div}\left((\Psi + \frac{1}{2}|\mathbf{v}|^2)\mathbf{v}\right) - \operatorname{div}(\mathbb{T}\mathbf{v} + \lambda\nabla\Psi) + \xi = \mathbf{b}\cdot\mathbf{v}. \tag{3.5}$$

Finally, use of the final form of the rate of entropy production (2.34) leads to:

$$\begin{aligned} &\frac{\partial}{\partial t}\left(\Psi + \frac{1}{2}|\mathbf{v}|^2\right) + \operatorname{div}\left((\Psi + \frac{1}{2}|\mathbf{v}|^2)\mathbf{v}\right) - \operatorname{div}(\mathbb{T}\mathbf{v} + \lambda\nabla\Psi) + 2\nu|\mathbb{D}|^2 \\ &+ \mu\lambda\left(\beta|\nabla\mathbb{B}_{\kappa_{p(t)}}|^2 + (1-\beta)|\mathbb{B}_{\kappa_{p(t)}}^{-\frac{1}{2}}(\nabla\mathbb{B}_{\kappa_{p(t)}})\mathbb{B}_{\kappa_{p(t)}}^{-\frac{1}{2}}|^2\right) \\ &+ \mu\left((1-\beta)\delta_1|\mathbb{B}_{\kappa_{p(t)}}^{\frac{1}{2}} - \mathbb{B}_{\kappa_{p(t)}}^{-\frac{1}{2}}|^2 + \beta\delta_2|\mathbb{B}_{\kappa_{p(t)}}^{\frac{3}{2}} - \mathbb{B}_{\kappa_{p(t)}}^{\frac{1}{2}}|^2\right) \\ &+ \mu((1-\beta)\delta_2 + \beta\delta_1)|\mathbb{B}_{\kappa_{p(t)}} - \mathbb{I}|^2 = \mathbf{b}\cdot\mathbf{v}. \end{aligned} \tag{3.6}$$

Finally, by integrating this identity over Ω, using Gauss theorem and the boundary conditions (3.2), we get an energy equality:

$$\begin{aligned} &\frac{\partial}{\partial t}\int_\Omega\left(\Psi + \frac{1}{2}|\mathbf{v}|^2\right) + \sigma\int_{\partial\Omega}|\mathbf{v}|^2 + 2\nu\int_\Omega|\mathbb{D}|^2 \\ &+ \mu\lambda\int_\Omega\left(\beta|\nabla\mathbb{B}_{\kappa_{p(t)}}|^2 + (1-\beta)|\mathbb{B}_{\kappa_{p(t)}}^{-\frac{1}{2}}(\nabla\mathbb{B}_{\kappa_{p(t)}})\mathbb{B}_{\kappa_{p(t)}}^{-\frac{1}{2}}|^2\right) \\ &+ \mu\int_\Omega\left((1-\beta)\delta_1|\mathbb{B}_{\kappa_{p(t)}}^{\frac{1}{2}} - \mathbb{B}_{\kappa_{p(t)}}^{-\frac{1}{2}}|^2 + \beta\delta_2|\mathbb{B}_{\kappa_{p(t)}}^{\frac{3}{2}} - \mathbb{B}_{\kappa_{p(t)}}^{\frac{1}{2}}|^2\right) \\ &+ \mu\int_\Omega((1-\beta)\delta_2 + \beta\delta_1)|\mathbb{B}_{\kappa_{p(t)}} - \mathbb{I}|^2 = \int_\Omega\mathbf{b}\cdot\mathbf{v}, \end{aligned} \tag{3.7}$$

where we used following identity:

$$-\int_\Omega\operatorname{div}(\mathbb{T}\mathbf{v} + \lambda\nabla\Psi) = -\int_{\partial\Omega}(\mathbb{T}\mathbf{v} + \lambda\nabla\Psi)\cdot\mathbf{n} = -\int_{\partial\Omega}(\mathbb{T}\mathbf{n})\cdot\mathbf{v} = \sigma\int_{\partial\Omega}|\mathbf{v}|^2.$$

The energy equality reveals appropriate choice of function spaces for the solution $(\mathbf{v}, \mathbb{B}_{\kappa_{p(t)}})$ and the form of the weak formulation of the solution of the closed set of equations (3.1), ..., (3.3).

3.3 Definition of a weak solution and its existence

Before stating the main result of the existence theory, we fix some notation. By $L^p(\Omega)$ and $W^{n,p}(\Omega)$, $1 \leq p \leq \infty$, $n \in \mathbb{N}$, we denote the usual Lebesgue and Sobolev space, with their usual norms denoted as $\|\cdot\|_p$ and $\|\cdot\|_{n,p}$, respectively. The trace operator that maps $W^{1,p}(\Omega)$ into $L^q(\partial\Omega)$, for certain $q \geq 1$, we denote by $\mathcal{T}$. Further, we set $W^{-1,p'}(\Omega) = (W^{1,p}(\Omega))^*$, where $p' = p/(p-1)$. We will use the same notation for the function spaces of scalar-, vector-, or tensor-valued functions, but we will distinguish the functions themselves using different fonts as before. Also, we denote the duality pairing by $\langle \cdot, \cdot \rangle$. Moreover, for certain subspaces of vector valued functions, we will use the following notation:

$$
\begin{aligned}
C^\infty_{\mathbf{n}} &= \{\mathbf{w} : \Omega \to \mathbb{R}^3 : \ \mathbf{w} \,\text{infinitely differentiable, } \mathbf{w}\cdot\mathbf{n} = 0 \text{ on } \partial\Omega\},\\
C^\infty_{\mathbf{n},\,\mathrm{div}} &= \{\mathbf{w} \in C^\infty_{\mathbf{n}} : \ \operatorname{div}\mathbf{w} = 0 \text{ in } \partial\Omega\},\\
L^2_{\mathbf{n},\,\mathrm{div}} &= \overline{C^\infty_{\mathbf{n},\,\mathrm{div}}}^{\|\cdot\|_2}, \quad W^{1,2}_{\mathbf{n},\,\mathrm{div}} = \overline{C^\infty_{\mathbf{n},\,\mathrm{div}}}^{\|\cdot\|_{1,2}}, \quad W^{-1,2}_{\mathbf{n},\,\mathrm{div}} = (W^{1,2}_{\mathbf{n},\,\mathrm{div}})^*.
\end{aligned}
$$

The Bochner spaces of mappings from $(0,\, T)$ to a Banach space X will be denoted as $L_p(0,\, T;\, X)$ with the norm $\|\cdot\|_{L_p(0,\,T;\,X)} = (\int_0^T \|\cdot\|_X^p)^{\frac{1}{p}}$.

Now, we state definition of a weak solution, that is motivated by the formal a priori estimate shown in the preceeding section.

Definition 1 (Bathory et al., 2020, page 507)**.** *Let $T > 0$ and assume that $\Omega \subset \mathbb{R}^3$ is a Lipschitz domain. Let $\beta \in (0,1)$, ν, σ, $\lambda > 0$, δ_1, $\delta_1 \geq 0$, $a \in \mathbb{R}$, and $\mathbf{b} \in L^2(0,T;W^{-1,2}_{\mathbf{n},\,\mathrm{div}})$, $\mathbf{v}_0 \in L^2_{\mathbf{n},\,\mathrm{div}}(\Omega)$. Furthermore, let $\mathbb{B}_{\kappa_{p(t)},0} \in L^2(\Omega)$ be such that*

$$
-\int_\Omega \ln(\det \mathbb{B}_{\kappa_{p(t)},0}) < \infty. \tag{3.8}
$$

Then, we say that a couple $(\mathbf{v},\, \mathbb{B}_{\kappa_{p(t)}}) : Q \longrightarrow \mathbb{R}^3 \times \mathbb{R}^{3\times 3}_{>0}$ is a weak solution to (3.1)-(3.3) if the following hold:

$$
\begin{aligned}
&\mathbf{v} \in L^2(0,T;W^{1,2}_{\mathbf{n},\,\mathrm{div}}) \cap L^\infty(0,T;L^2(\Omega)), \quad \frac{\partial \mathbf{v}}{\partial t} \in L^{\frac{4}{3}}(0,T;W^{-1,2}_{\mathbf{n},\,\mathrm{div}}),\\
&\mathbb{B}_{\kappa_{p(t)}} \in L^2(0,T;W^{1,2}(\Omega)) \cap L^\infty(0,T;L^2(\Omega)), \quad \frac{\partial \mathbb{B}_{\kappa_{p(t)}}}{\partial t} \in L^{\frac{4}{3}}(0,T;W^{-1,2}(\Omega));
\end{aligned} \tag{3.9}
$$

For all $\phi \in L^4(0,T;W^{1,2}_{\mathbf{n},\,\mathrm{div}})$ we have

$$
\begin{aligned}
&\int_0^T \langle \frac{\partial \mathbf{v}}{\partial t}, \phi\rangle + \int_Q (\mathbf{v}\cdot\nabla)\mathbf{v}\cdot\phi + \sigma\int_0^T\int_{\partial\Omega} \mathcal{T}\mathbf{v}\cdot\mathcal{T}\phi =\\
&-\int_Q (2\nu\mathbb{D} + 2a\mu((1-\beta)(\mathbb{B}_{\kappa_{p(t)}} - \mathbb{I}) + \beta(\mathbb{B}^2_{\kappa_{p(t)}} - \mathbb{B}_{\kappa_{p(t)}}))) \cdot \nabla\phi + \int_0^T \langle b, \phi\rangle;
\end{aligned} \tag{3.10}
$$

For all $\mathbb{A} \in L^4(0,T;W^{1,2}(\Omega))$, $\mathbb{A} = \mathbb{A}^T$, we have

$$
\begin{aligned}
&\int_0^T \langle \frac{\partial \mathbb{B}_{\kappa_{p(t)}}}{\partial t}, \mathbb{A}\rangle + \int_Q ((\mathbf{v}\cdot\nabla)\mathbb{B}_{\kappa_{p(t)}} + 2\mathbb{B}_{\kappa_{p(t)}}\mathbb{W} - 2a\mathbb{B}_{\kappa_{p(t)}}\mathbb{D})\cdot\mathbb{A}\\
&+ \int_Q (\delta_1(\mathbb{B}_{\kappa_{p(t)}} - \mathbb{I}) + \delta_2(\mathbb{B}^2_{\kappa_{p(t)}} - \mathbb{B}_{\kappa_{p(t)}}))\cdot\mathbb{A} + \lambda\int_Q \nabla\mathbb{B}_{\kappa_{p(t)}}\cdot\nabla\mathbb{A} = 0.
\end{aligned} \tag{3.11}
$$

The initial conditions are satisfied in the following sense

$$\lim_{t\to 0_+}\left(\|\mathbf{v}(t)-\mathbf{v}_0\|_2+\|\mathbb{B}_{\kappa_{p(t)}}(t)-\mathbb{B}_{\kappa_{p(t)},0}\|_2\right)=0. \tag{3.12}$$

Moreover, we say that the solution satisfies the energy inequality if, for all $t\in(0,T)$*:*

$$\begin{aligned}
&\int_\Omega\left(\frac{|\mathbf{v}(t)|^2}{2}+\Psi(\mathbb{B}_{\kappa_{p(t)}}(t))\right)+\int_0^t\left(2\nu\|\mathbb{D}\|_2^2+\sigma(\|\mathcal{T}\mathbf{v}\|_{2,\partial\Omega}^2\right)\\
&+\mu\lambda\int_0^t\left((1-\beta)\|\mathbb{B}_{\kappa_{p(t)}}^{-\frac{1}{2}}(\nabla\mathbb{B}_{\kappa_{p(t)}})\mathbb{B}_{\kappa_{p(t)}}^{-\frac{1}{2}}\|_2^2+\beta\|\nabla\mathbb{B}_{\kappa_{p(t)}}\|_2^2\right)\\
&+\mu\int_0^t\left((1-\beta)\delta_1\|\mathbb{B}_{\kappa_{p(t)}}^{\frac{1}{2}}-\mathbb{B}_{\kappa_{p(t)}}^{-\frac{1}{2}}\|_2^2+\beta\delta_2\|\mathbb{B}_{\kappa_{p(t)}}^{\frac{3}{2}}-\mathbb{B}_{\kappa_{p(t)}}^{\frac{1}{2}}\|_2^2\right)\\
&+\mu\int_0^t(\beta\delta_1+(1-\beta)\delta_2)\|\mathbb{B}_{\kappa_{p(t)}}-\mathbb{I}\|_2^2\\
&\le\int_\Omega\left(\frac{|\mathbf{v}_0|^2}{2}+\Psi(\mathbb{B}_{\kappa_{p(t)},0})\right)+\int_0^t\langle\mathbf{b}\cdot\mathbf{v}\rangle.
\end{aligned} \tag{3.13}$$

Next, we state the main theorem of this chapter. For the full explanation of the difficulties connected with such analysis, see Bathory et al. [2020].

Theorem 1 (Bathory et al., 2020, page 508)**.** *Let* $T>0$ *and assume that* $\Omega\subset\mathbb{R}^3$ *is a Lipschitz domain. Suppose* $\beta\in(0,1)$*,* ν*,* σ*,* $\lambda>0$*,* δ_1*,* $\delta_2\ge 0$*,* $a\in\mathbb{R}$*, and* $\mathbf{b}\in L^2(0,T;W^{-1,2}_{\mathbf{n},\mathrm{div}})$*,* $\mathbf{v}_0\in L^2_{\mathbf{n},\mathrm{div}}(\Omega)$*. Furthermore, let* $\mathbb{B}_{\kappa_{p(t)},0}\in L^2(\Omega)$ *be such that (3.8) holds. Then there exists a weak solution to (3.1)-(3.3) satisfying the energy inequality.*

Proof. The individual steps of the proof are described in detail in the work Bathory et al. [2020, p. 509], Chapter 3 Proof of the Theorem. □

3.4 Finite element method (FEM)

In this section we introduce details of finite element method of our implementation in open-source computing platform FEniCS as a finite element library for Python.

3.4.1 Weak formulation for FEM

For FEM we need to use a different weak fomulation than the one defined in the Definition 1 as it is not convenient to work with the space $W^{1,2}_{\mathbf{n},\mathrm{div}}$ within the FEniCS library. Thus we must modify the choice of spaces in (3.9) to a formulation with the pressure and we formally write for all admissible test functions $(\psi,\phi,\mathbb{A})$:

$$\begin{aligned}
\int_\Omega\operatorname{div}\mathbf{v}\psi&=0,\\
\int_\Omega\rho\left[\frac{\partial\mathbf{v}}{\partial t}+(\mathbf{v}\cdot\nabla)\mathbf{v}\right]\cdot\phi-\int_\Omega\mathbb{T}\cdot\nabla\phi+\int_{\Gamma_N}\mathbf{t}\cdot\phi-\int_\Omega\rho\mathbf{b}\cdot\phi&=0,\\
\mathbb{T}=-p\mathbb{I}+2\nu\mathbb{D}+aG\left[(1-\beta)(\mathbb{B}_{\kappa_{p(t)}}-\mathbb{I})+\beta(\mathbb{B}_{\kappa_{p(t)}}-\mathbb{I})\mathbb{B}_{\kappa_{p(t)}}\right],&\\
\int_\Omega\frac{\delta\mathbb{B}_{\kappa_{p(t)}}}{\delta t}\cdot\mathbb{A}+\left[\delta_1(\mathbb{B}_{\kappa_{p(t)}}-\mathbb{I})+\delta_2(\mathbb{B}^2_{\kappa_{p(t)}}-\mathbb{B}_{\kappa_{p(t)}})\right]\cdot\mathbb{A}+\lambda\int_\Omega\nabla\mathbb{B}_{\kappa_{p(t)}}\cdot\nabla\mathbb{A}&=0,
\end{aligned} \tag{3.14}$$

where we setted $G := 2\mu$ and $\mathbf{t} = \mathbb{T}\mathbf{n}$ is a traction, $\mathbf{n}$ is a unit outward normal.

3.4.2 Space discretization

We discretize system of equations (3.14) in each time step (or at a stationary state) using the FEM. We approximate computational domain Ω by a regular triangulation and approximate curved boundaries is such a way that the vertices of boundary triangle edges lie on $\partial\Omega$. We also occasionaly refine certain parts of the mesh by red-green refinement[1], which is based on empirical experiences, not on a posteriori error estimates. As a basis functions, we use Taylor-Hood elements for solution of a classical Navier-Stokes unknowns (p, $\mathbf{v}$), as it is a typical choice that satisfies Babuška-Brezzi (inf-sup) condition. We complete this basis with a standard continuous piecewise linear elements P_1 for each independent entry of the left Cauchy-Green tensor B_{ij} (6 elements in 3D). Moreover, for the problems with the ALE method, we use the very same elements for mesh deformation $\hat{\mathbf{u}}$ as it correspond to the velocity.

3.4.3 Numerical solver

We use a monolithic non-linear solver, which uses well-known Newton method with MUMPS as a linear solver based on LU decomposition.

3.4.4 Time discretization

In this section, we introduce time discretization of the evolutionary problem given by set of equations (3.1) that is solved in time-space cylinder Q. We split the time interval $[0, T]$ into N subintervals and denote $\Delta t^n := t^{n+1} - t^n$ the n-th time step, $n = 0, \ldots, N-1$. Note that system of equations is generally in the form:

$$\frac{\partial u(x,t)}{\partial t} + f(u(x,t)) = 0 \quad \text{in } Q, \tag{3.15}$$

and at every time level t^{n+1} we solve for $u^{n+1}(x) := u(x, t_0 + \sum_{i=0}^{n} \Delta t^i)$ by FEM. Basic first order unconditionally stable time scheme is the Implicit backward Euler scheme (BE):

$$\frac{u^{n+1}(x) - u^n(x)}{\Delta t^n} + f(u^{n+1}(x)) = 0. \tag{3.16}$$

We also experiment with the Implicit Glowinski three-step scheme, while using ALE method. For more details, see corresponding section in numerical results.

[1]Refinement iteration is done by finding the barycenter of the triangle and connecting it to each of its vertices, creating four triangles from one. And if the neighboring triangle is not refined also, then the new vertex on his edge is connected with its opposite vertex.

4. Numerical implementations

In this chapter we introduce results, that we obtained by simulating classical benchmark Fan et al. [1999] in 2D and well-known non-Newtonian phenomena using derived models, namely the model with **stress** diffusion. For simulation purposes, we use open-source computing platform FEniCS as a finite element library for Python. All used scripts are published in the Charles University Digital Repository, and they are available in public repository: `https://github.com/cachja/master-thesis`. Moreover, see Appendix A.1 for their description.

4.1 Flow past a cylinder

In this section, we simulate classical 2D benchmark of a planar viscoelastic flow around a cylinder in a narrow channel. For this purpose, the convex combination of the Oldroyd-B and Giesekus model with stress diffusion is used, governed by equations (3.1). Based on that simulations, we study the effects of stress diffusion, convex combinations of the models and various objective derivatives. Finally, these results are compared to the large data existence Theorem 1.

4.1.1 Definition of the benchmark

This benchmark was introduced by Fan et al. [1999], therefore the dimensions of the channel in this simulation correspond to this benchmark. In order to decrease computational cost, we assume problem to be symmetric along horizontal axis as the setting of the problem is symmetric and the only asymmetry may be induced by numerical errors. Hence the dimensions are the following: length of the channel $Len = 40$, width of the channel $Wid = 2$, and the radius of the cylinder $R = 1$, see sketch of the domain in Figure 4.1. Note that all quantities are dimensionless as the only parameter given is the Weissenberg number We.

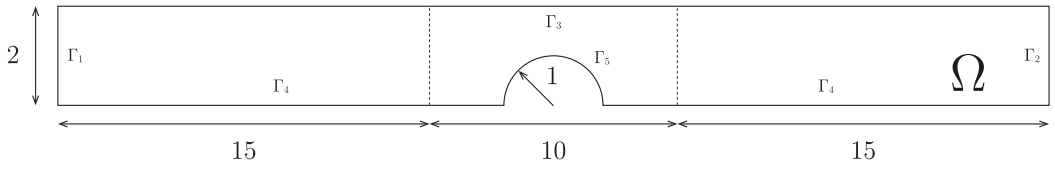

Figure 4.1: Sketch of the computational domain for the flow past cylinder benchmark.

The boundary of the computational domain is split into the following boundary parts: Γ_1, ..., Γ_5 denote in the same order inflow, outflow, upper wall, symmetric axis, and cylinder wall, see Figure 4.1. Part of the domain where the local refinement of the mesh is used due to the curvature of the boundary and the channel narrowing leading to the velocity increase is marked by the dashed line. Axis x, y are defined as usual, i.e., x horizontally, y vertically and the origin is placed at the lower left corner of the domain.

4.1.2 Boundary conditions

Boundary conditions are chosen naturally: no-slip condition on the upper wall Γ_3 and the cylinder wall Γ_5, free-slip condition due to the symmetry on Γ_4, condition $\mathbf{v} = (\frac{3}{8}(4-y^2), 0)$ at the inflow Γ_1, traction-free condition at the outflow Γ_2.

Given the inlet velocity, one can try to a priori obtain solution (used as a boundary condition later) for $\mathbb{B}_{\kappa_{p(t)}}$ on the velocity inlet Γ_1. This can be done by assumption that flow entering the domain is a Poiseuille flow. That is a laminar Stokes flow in the form $\mathbf{v} = (v_x(y), 0)$ in the 2D uniform rectangular channel, which is moreover steady, fully developed and the y-component of the velocity is zero. Note that as we assume flow to be steady, it implies $\partial\mathbb{B}_{\kappa_{p(t)}}/\partial t = 0$ on Γ_1. Moreover, we observe that $\mathbf{v}\cdot\nabla\mathbb{B}_{\kappa_{p(t)}} = 0$ on Γ_1. This simplify the equation (3.1) (specifically equation (2.23)) to the non-linear system of three ordinary non-linear differential equations as the matrix equation is symmetric:

$$\begin{aligned}\delta_2\mathbb{B}^2_{\kappa_{p(t)}}\Big|_{\Gamma_1} + (\delta_1-\delta_2)\mathbb{B}_{\kappa_{p(t)}}\Big|_{\Gamma_1} - (a\mathbb{D}+\mathbb{W})\mathbb{B}_{\kappa_{p(t)}}\Big|_{\Gamma_1} \\ -\mathbb{B}_{\kappa_{p(t)}}\Big|_{\Gamma_1}(a\mathbb{D}-\mathbb{W}) - \delta_1\mathbb{I} - \lambda\Delta\mathbb{B}_{\kappa_{p(t)}}\Big|_{\Gamma_1} = \mathbb{O},\end{aligned} \tag{4.1}$$

recall that a is a parameter of the Gordon-Schowalter family of objective derivatives. In practice, this cannot be solved analytically, hence we focus on a special case $\delta_2 = 0, \lambda = 0$ and for other cases this boundary condition is omitted. Finally, by substituting velocity inlet condition into the above equation we find the solution for $\mathbb{B}_{\kappa_{p(t)}}$:

$$\mathbb{B}\Big|_{\Gamma_1} = \frac{1}{9(1-a^2)y^2 + 16\delta_1^2}\begin{pmatrix} 16\delta_1^2 + 9(a+1)y^2 & -12ay\delta_1 \\ -12ay\delta_1 & 16\delta_1^2 + 9(1-a)y^2 \end{pmatrix}.$$

4.1.3 Stationary solution – quantities of interest

In this benchmark, we are interested in the steady solution. Hence we drop time derivatives in the equation (3.1). Moreover, in order to converge to the steady state as quickly as possible, we follow the work of Damanik [2011] and we drop the non-linear term in the material time derivative in the balance of linear momentum. This is the same approach as was used in the work by Walkington et al. [2016], where was the density ρ was set to zero.

In the steady state, we compute forces acting on the cylinder boundary Γ_5. From the symmetry, it is obvious that $lift = 0$. However, $drag$ is nonzero:

$$drag = -2\begin{pmatrix}1\\0\end{pmatrix}\cdot\int_{\Gamma_5}\mathbb{T}\cdot\mathbf{n}\,\mathrm{d}\Gamma_5, \tag{4.2}$$

where $\mathbf{n}$ in a unit outward normal vector. Note that in this case the forces are dimensionless and the multiplication by coefficient 2 is due to the symmetry of the domain. The effect of the Weissenberg number on the drag will be studied.

As was shown by Dostalík et al. [2019], even the internal viscoelastic flow faces instabilities for the high Weissenberg number. Regarding such instabilities in our simulation, we are also interested in the coefficient λ in the stress diffusion term. We expect that due to the instability and numerical errors there will be a lower bound λ^* for this coefficient under which we will not be able to converge to the steady solution. Hence for every solution, λ will be minimized to this bound monotonically from a greater estimate λ_0, see next section for details.

4.1.4 Continuation (homotopy) method

As discussed in the previous section, we are interested in the steady solution only. Hence it could seem that the choice of the initial condition (for a monolithic numerical solver) is not that important if we are able to converge to the solution from trivial initial condition on the whole domain: $\mathbf{v} = \mathbf{0}$, $p = 0$, $\mathbb{B} = \mathbb{I}$. However, this is not true for the high Weissenberg numbers and λ close to λ^*. Hence for increasing *We* and decreasing λ we use a continuation method, i.e., as an initial solution for the next problem, the previous solution is used.

Note that even though continuation method seems trivial, the proof of convergence of such approach for our complicated problem greatly exceeds this work. Also, this method does not work always, following cases may occur: 1) Change of parameters between two solutions must be sufficiently small, even close to the machine precision, which makes the problem so computationally demanding that it is practically unbearable. 2) The curve in the phase space of a solution parametrized by chosen parameter may contain a blow-up for some interval of parameters. One of these cases was observed in my bachelor thesis Cach [2021], where the problem could not be solved for any *We* using this method together with stabilization over edges. However, in this work, we were able to overcome these bounds by adding the stress diffusion. Also, since we know that the problem cannot be solved without the stress diffusion, we expect lower bound for $\lambda^* > 0$. We may consider the elliptic term with λ as a stabilization term, hence the value of $\lambda^* > 0$ may be mesh-size dependent.

Specifically, we use the continuation method for one parameter only, i.e., with fixed λ we solve for higher *We* and then with *We* fixed we solve for smaller λ where we use monotonic 1D minimizing method, that finds λ^* with 10 % relative error. Note that change of both parameters at once may cause solution to be outside of converging neighborhood of a direct solver.

4.1.5 Mesh

All computational meshes are generated by setting the following parameters in the scripts using FEniCS available in the appendix: $cr :=$ `cylinder_refinement`, $mr :=$ `mesh_refinement`, and $lri :=$ `local_refinement_iterations`, meaning: number of points on the cylinder boundary, refinement of the mesh in the whole domain, number of iterations of extra refinement of the mesh in the middle around the cylinder. Refinement iteration is done by finding the barycenter of the triangle and connecting it to each of its vertices, creating four triangles from one (red-green refinement). We generated in total three meshes, see Figure 4.2 and Figure 4.3. Also see Table 4.1 for the important parameters of these meshes: the smallest edge length of a triangle in the mesh h_{min}, the largest edge length of a triangle in the mesh h_{max} and the size of the problem, i.e., total number of degrees of freedom DoF. We recommend mesh No. 1 for quick tentative results, mesh No. 2 for minimizing λ as the minimizing method together with continuation method takes a lot of iterations and mesh No. 3 for very accurate results.

Mesh No.	cr	mr	lri	h_{min}	h_{max}	DoF
1	100	200	1	0.0222	0.3604	39882
2	150	300	2	0.0074	0.2402	229002
3	200	400	2	0.0056	0.1802	384902

Table 4.1: Overview of important parameters of used meshes.

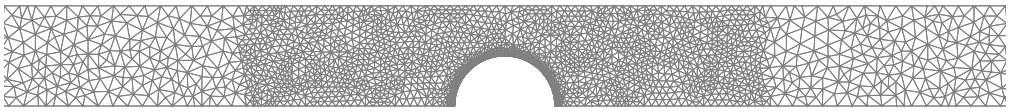

(a) Mesh No. 1.

(b) Mesh No. 2.

(c) Mesh No. 3.

Figure 4.2: Mesh cutout for $x \in (10, 30)$.

4.1.6 Fluid model parameters

The last, and the most important, piece of information needed for this benchmark are the properties of the fluid given by parameters occurring in the equation (3.1). These parameters are varied in order to investigate validity of the large data existence Theorem 1 by numerical experiment and possibly propose an extension of the parameters that are not stated there, however, are working in simulations.

From the work of Damanik et al. [2010] we took the parameters corresponding to the equation (3.1), note that $\hat{\mu}$ is a dummy parameter here, namely $\hat{\mu} + \nu = 1$, $\nu = 0.59$, $2\mu =: G = \hat{\mu}/\,We = (1-\nu)/\,We = 0.41/\,We$, where We is varied. Recall that the fluid is incompressible and homogeneous. These properties are common for all following simulations.

Then we distinguish following cases, see (2.21), for $a = 1$ and $\lambda = 0$: if $\delta_1 = 1/\,We$ and $\delta_2 = 0$ we obtain Oldroyd-B model while if $\delta_1 = 0$ and $\delta_2 = 1/\,We$ we obtain Giesekus-like model. For those models we vary $\beta \in [0, 1]$, $\lambda \in [\lambda^*, \lambda_0]$. We also use stabilization over edges parametrized by α coefficient if needed, and is not used unless otherwise stated. Eventually, one can also vary parameter a corresponding to Gordon-Schowalter derivatives. Obviously, for $a = 0$ there is no extra stress in Cauchy stress tensor and the equations (3.1) simplify to Naviers-Stokes equations. See Table (4.2) for used combinations of parameters.

Table 4.2: All coefficients combinations used in the simulations. The following problems are investigated: Giesekus *Combo 1* model, Giesekus *Combo 2* model, Oldroyd-B *Combo 1* model (all these models come with convex combinations of energies) and change of an objective derivative for Oldroyd-B *Combo 2* model.

Model	a	β	δ_1	δ_2	λ
Giesekus Combo 1	1	[0,1]	0	$1/We$	$[\lambda^*, \lambda_0]$
Oldroyd-B Combo 1	1	[0,1]	$1/We$	0	$[\lambda^*, \lambda_0]$
Giesekus Combo 2	1	[0,1]	$1/We$	$1/We$	$[\lambda^*, \lambda_0]$
Oldroyd-B Combo 2	[0,1]	0	$1/We$	0	$[\lambda^*, \lambda_0]$

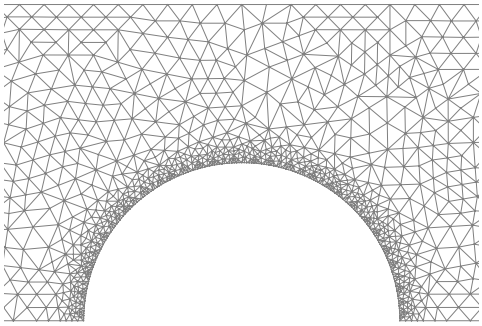

(a) Mesh No. 1.

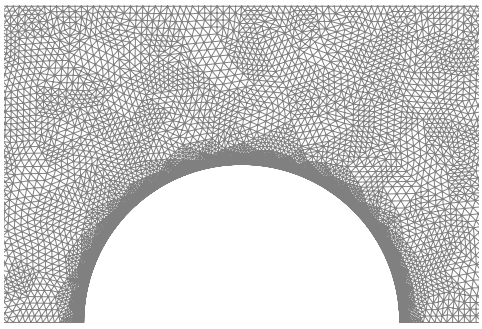

(b) Mesh No. 2.

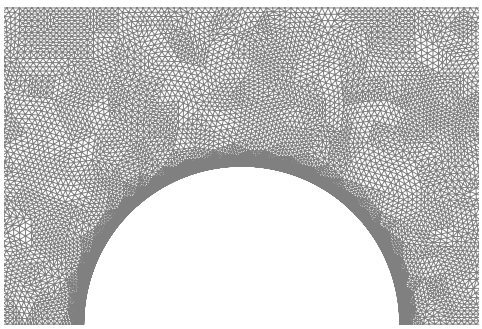

(c) Mesh No. 3.

Figure 4.3: Mesh cutout for $x \in (18.5, 21.5)$.

4.1.7 Giesekus Combo 1 model

In this section, we use parameters in the first line of the Table (4.2) corresponding to this model. Remaining parameters are specified later.

Finding minimal λ for Giesekus Combo 1 model

First of all, we are interested in the λ^* dependence w. r. t. *We* for varying β. Using approach mentioned above, we choose $\lambda_0 = 10$ together with parameters in the first line of the Table (4.2), where $\alpha = 0$, i.e., no additional stabilization over edges is used. See Figure (4.4) for the plot of such dependence. We observe fast growth at the beginning, which indicates that we will not be able to compute simulations for large *We* without stress diffusion. Also, the functions can be bounded by a relatively small constant $\lambda_{max} \approx 0.012$, hence stress diffusion may be seen as a reasonable stabilization.

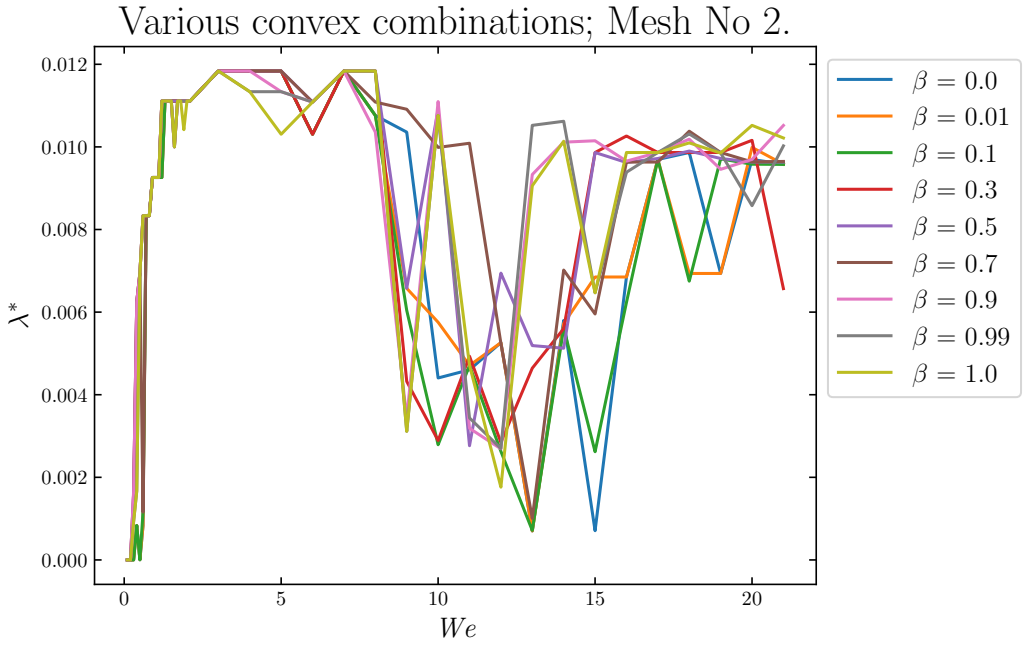

Figure 4.4: Plot for Giesekus Combo 1 model of λ^* versus *We* for varying β.

Effect of λ on *drag* for Giesekus Combo 1 model

Next, we check effect of $\lambda > 0$ on the solution by looking at *drag* dependence w. r. t. *We* for varying λ. Moreover, we set $\beta = 0$ and $\alpha = 0.01$. As can be seen from the Figure (4.5), even with the stabilization over edges we are not able to find solution for $We > 0.5$ (without this stabilization, we are not able to reach even $We = 0.4$). However, stabilization by stress diffusion works well and the difference between solution with $\lambda = 0$ and the solutions with $\lambda > 0$ is more than acceptable for λ_{max}.

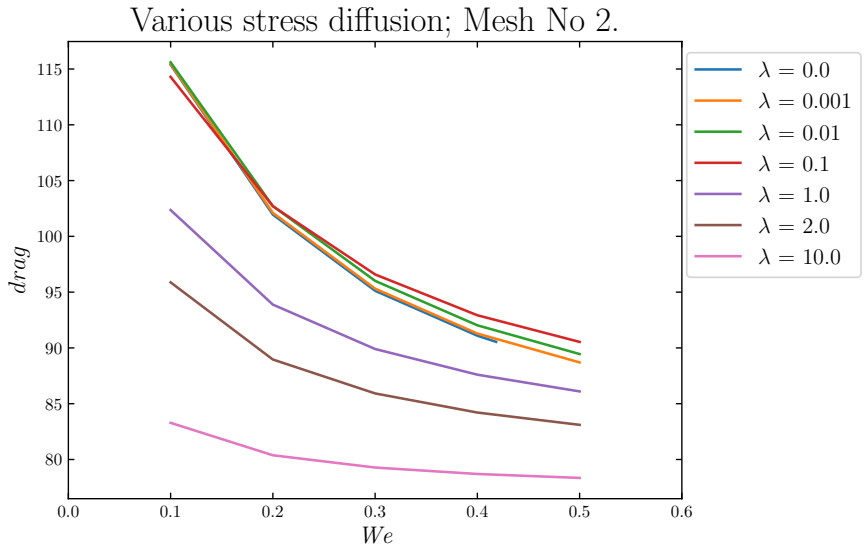

Figure 4.5: Plot for Giesekus Combo 1 model ($\beta = 0$, $\alpha = 0.01$) of *drag* versus *We* for varying λ.

Effect of β on *drag* for Giesekus Combo 1 model

Finally, we fix $\lambda = 0.02$ and study *drag* dependence w. r. t. *We* for varying β. Looking at Figure (4.6), one can state that all convex combinations of energies given by β are physically relevant. Note, that there is no bound for *We*, one can proceed for larger *We* than plotted.

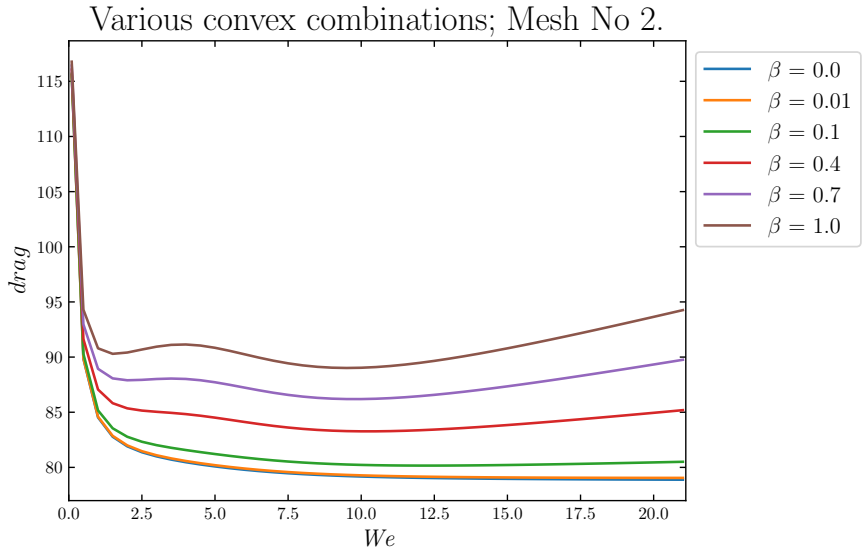

Figure 4.6: Plot for Giesekus Combo 1 model ($\lambda = 0.02$) of *drag* versus *We* for varying β.

Moreover, we plot streamlines in the domain colored by velocity magnitude for a few *We* with the last parameter choice, see Figure (4.7). We observe a vortex behind of the cylinder. With increasing β, it occurs for lower *We*, and hence we plot vortex for $\beta = 0.99$ as for this β the convex combination of energies takes into account both of them.

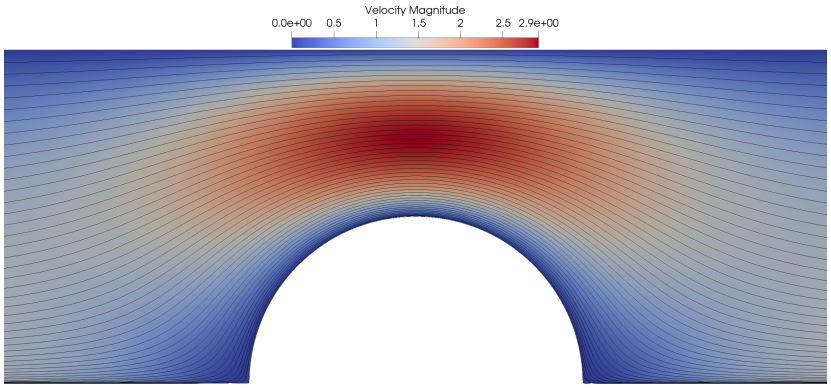

(a) For $\beta = 0$ and $We = 1$.

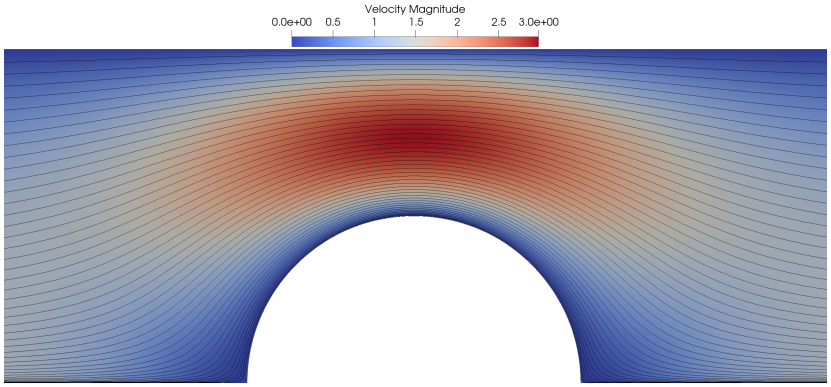

(b) For $\beta = 0$ and $We = 21$.

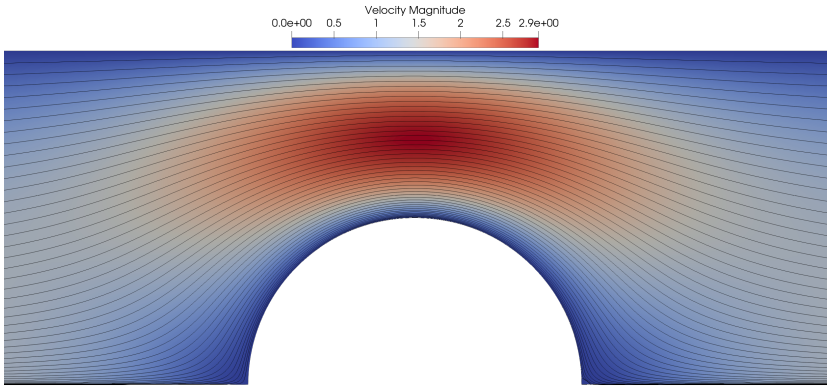

(c) For $\beta = 0.99$ and $We = 1$.

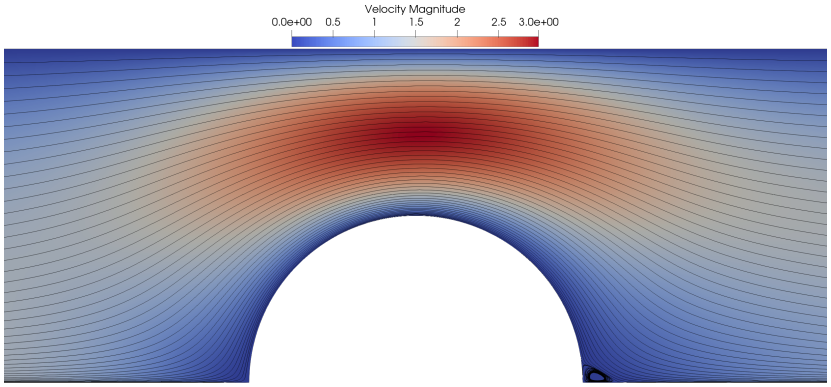

(d) For $\beta = 0.99$ and $We = 21$.

Figure 4.7: Plot of streamlines over velocity magnitude for Giesekus Combo 1 model.

4.1.8 Oldroyd-B Combo 1 model

In this section, we use parameters in the second line of the Table (4.2) corresponding to this model. Remaining parameters are specified later.

Finding minimal λ for Oldroyd-B Combo 1 model

For Oldroyd-B model, we are interested in the same dependencies as in the case of Giesekus model. Hence we plot λ^*versus We for varying β, see Figure (4.8). However in this case, we observe quick jump for $We \approx (1.5, 2.0)$ following by linear growth for $\beta > 0.2$.

Looking on streamlines plotted over domain colored by velocity magnitude, see Figure (4.9) for $\beta = 0$, Figure (4.10) for $\beta = 0.2$, Figure (4.11) for $\beta = 0.9$, and Figure (4.12) for $\beta = 1$, it is obvious that growth of λ^* is connected with the need of stabilization of growing vortex downstream from the cylinder. Moreover, for $\beta = 0.0$ there is quick change of velocity profile between $We = [2.0, 2.1]$ connected with the jump change of λ^*. Same behavior is observed for $\beta = 0.9$ and $We = [1.5, 1.6]$. Moreover, for this β, we observe that linear growth of λ^* after the jump is connected to the growth of the vortex **upstream** in front of the cylinder. Finally, we observe that for $\beta = 1$ the vortex appears for the first time for lesser We than in the case of $\beta = 0.9$. Note that this physical behavior is correct as it was experimentally observed for viscoelastic fluids in the works of Kenney et al. [2013] and Hopkins et al. [2022], see Appendix A.2.

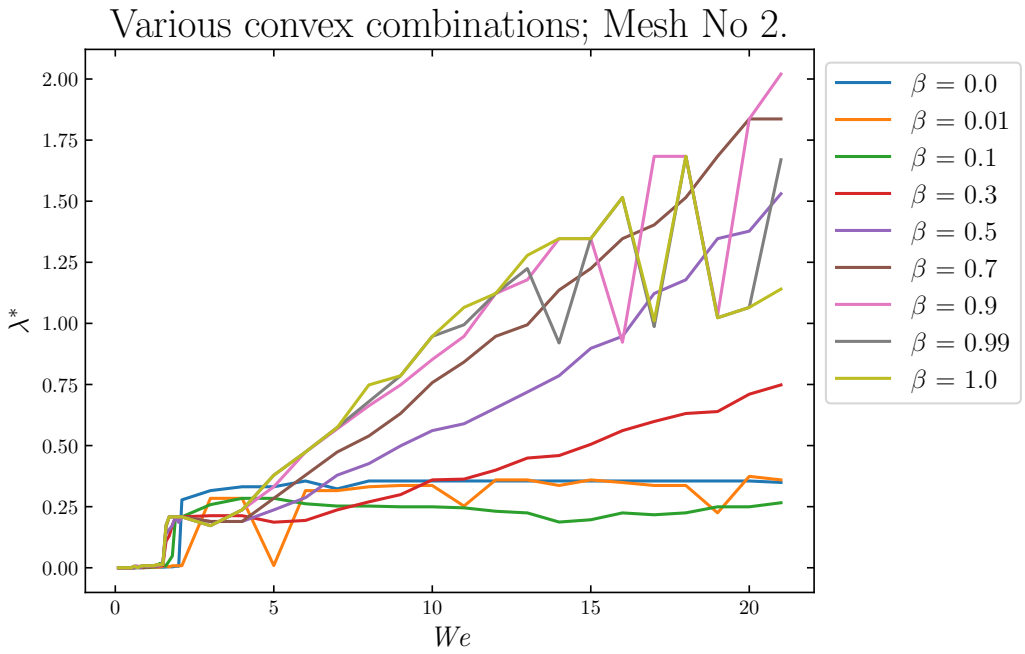

Figure 4.8: Plot for Oldroyd-B Combo 1 model of λ^* versus We for varying β.

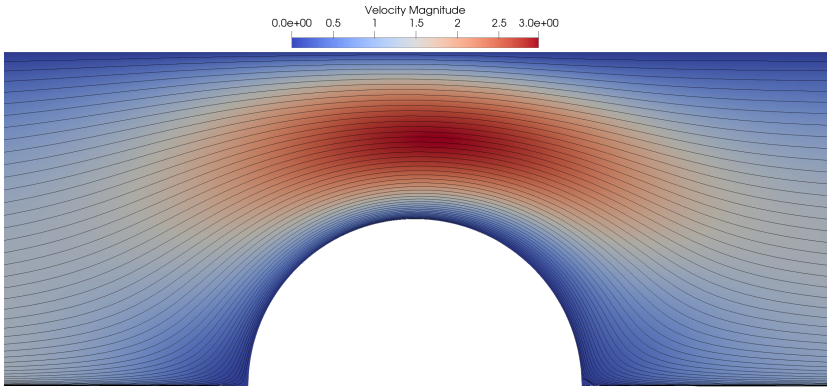

(a) For $\beta = 0$ and $We = 1.0$.

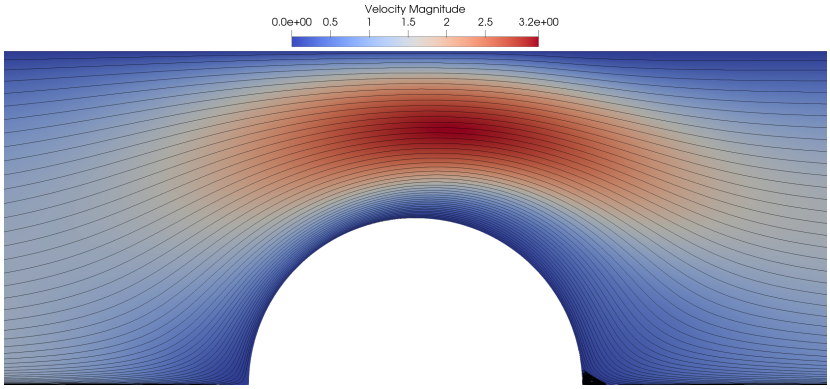

(b) For $\beta = 0$ and $We = 1.5$.

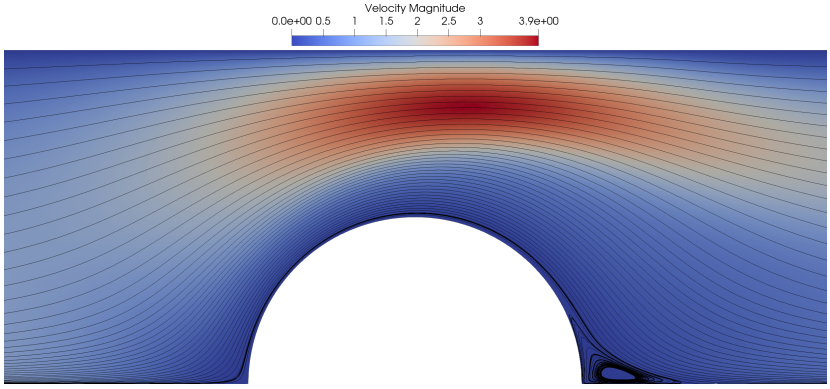

(c) For $\beta = 0$ and $We = 2.0$.

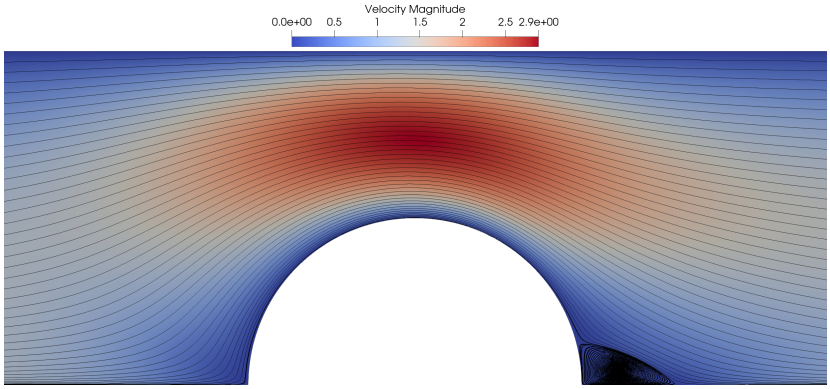

(d) For $\beta = 0$ and $We = 2.1$.

Figure 4.9: Plot of streamlines over velocity magnitude for Oldroyd-B Combo 1 model. Observe growing vortex downstream from the cylinder and how it changes its shape w. r. t. We and velocity profile around the cylinder.

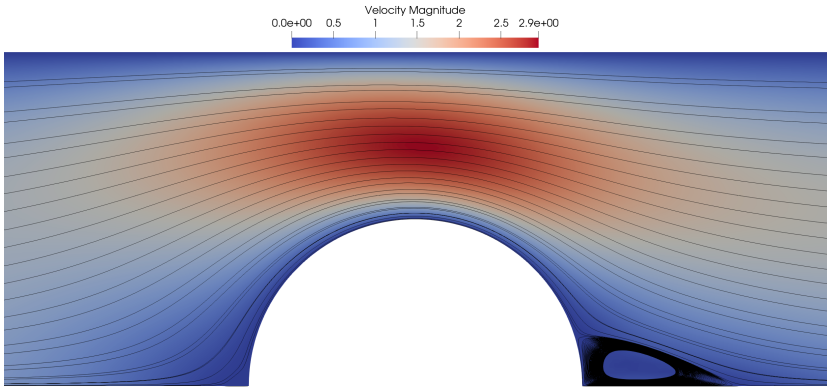

(a) For $\beta = 0.2$ and $We = 5.0$.

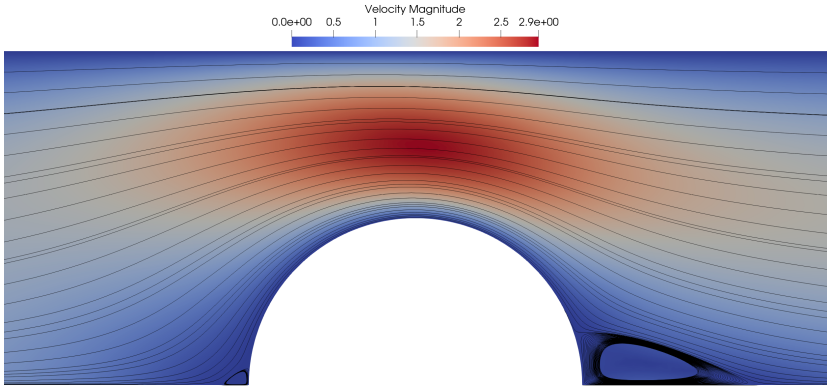

(b) For $\beta = 0.2$ and $We = 5.5$.

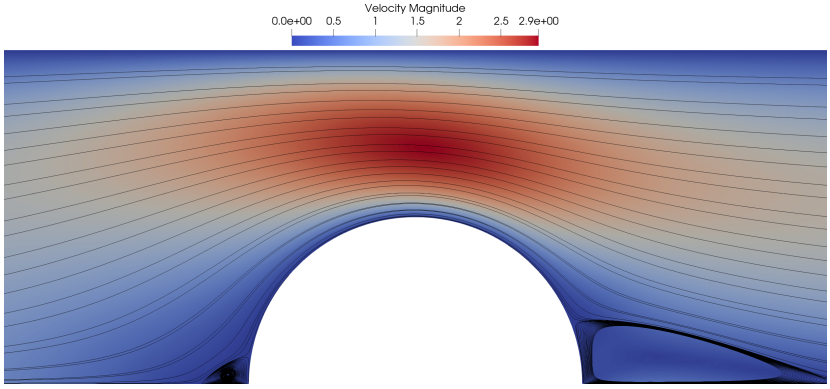

(c) For $\beta = 0.2$ and $We = 8.0$.

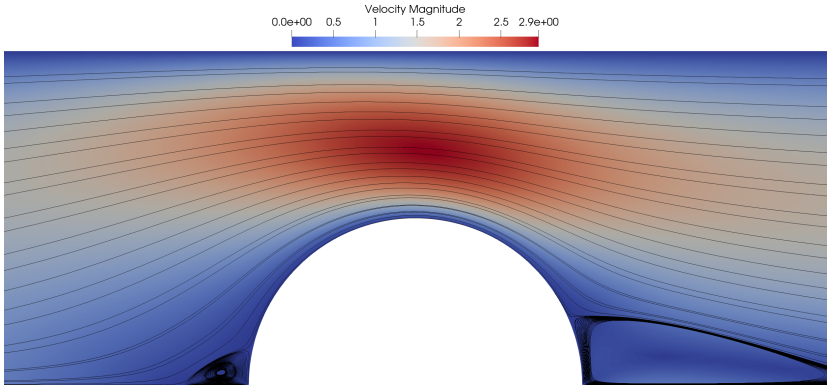

(d) For $\beta = 0.2$ and $We = 10.0$.

Figure 4.10: Plot of streamlines over velocity magnitude for Oldroyd-B Combo 1 model. Observe growing vortex both downstream and **upstream** from the cylinder and how it changes its shape w. r. t. We and velocity profile around the cylinder.

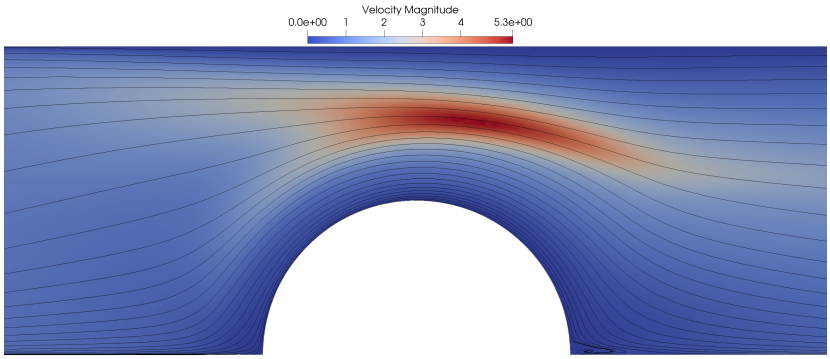

(a) For $\beta = 0.9$ and $We = 1.5$.

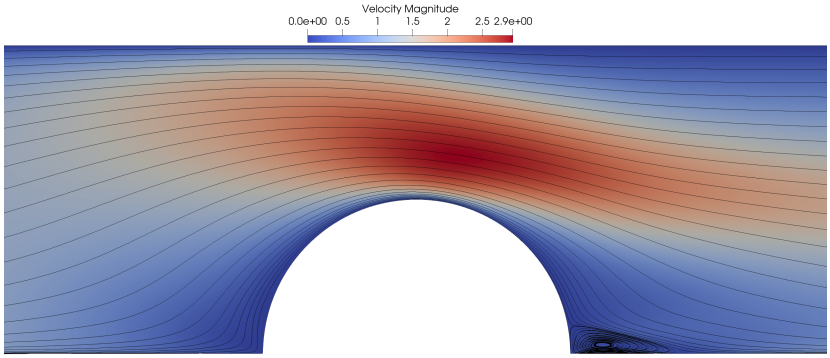

(b) For $\beta = 0.9$ and $We = 1.6$.

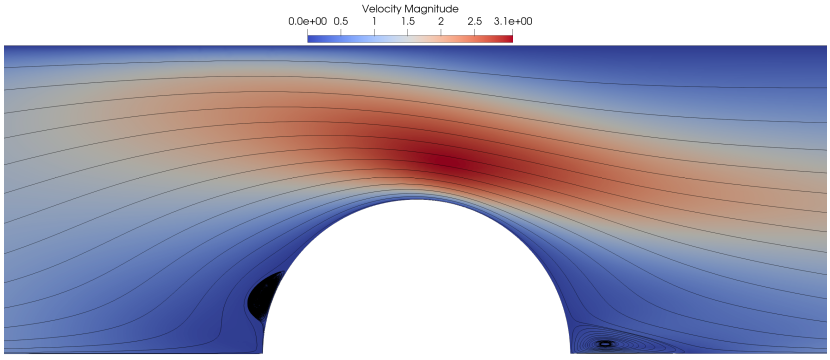

(c) For $\beta = 0.9$ and $We = 1.8$.

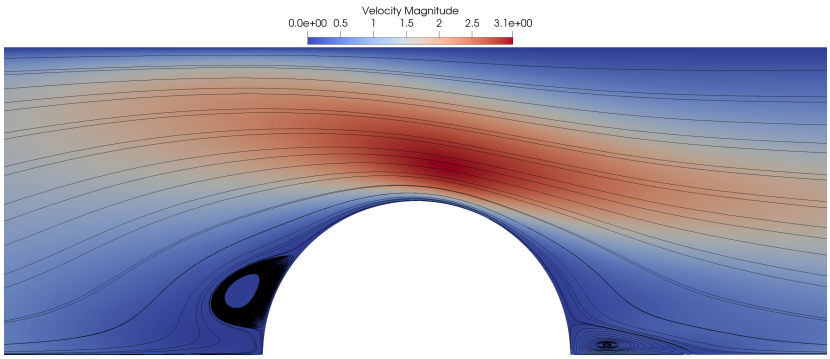

(d) For $\beta = 0.9$ and $We = 2.1$.

Figure 4.11: Plot of streamlines over velocity magnitude for Oldroyd-B Combo 1 model. Observe growing vortex both downstream and **upstream** from the cylinder and how it changes its shape w. r. t. We and velocity profile around the cylinder.

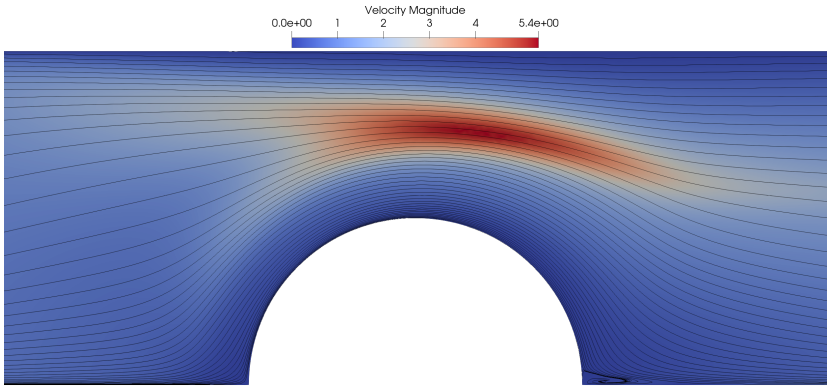

(a) For $\beta = 1$ and $We = 1.5$.

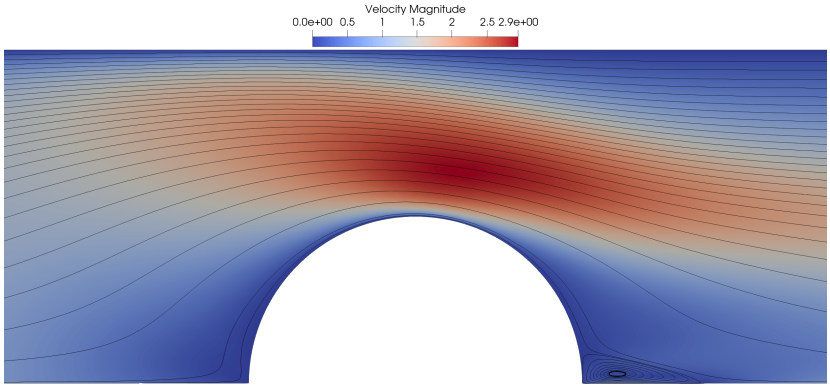

(b) For $\beta = 1$ and $We = 1.6$.

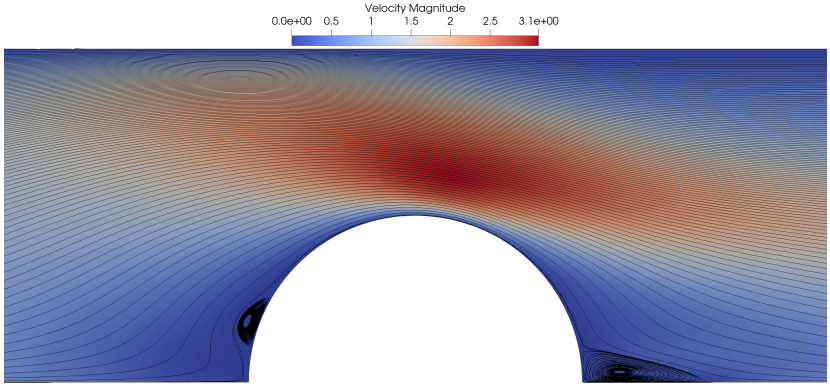

(c) For $\beta = 1$ and $We = 1.7$.

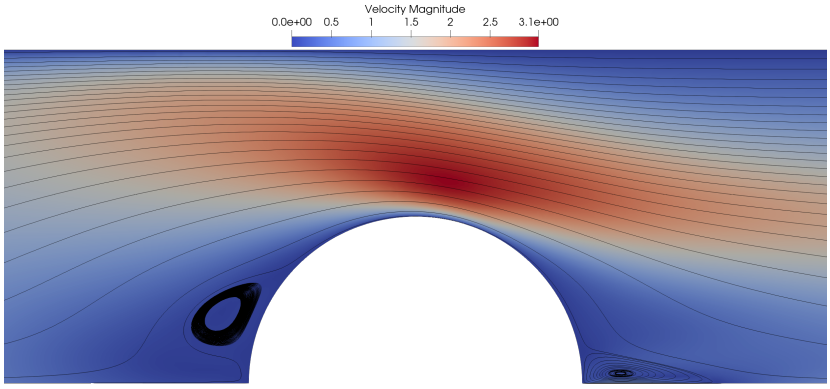

(d) For $\beta = 1$ and $We = 2.1$.

Figure 4.12: Plot of streamlines over velocity magnitude for Oldroyd-B Combo 1 model. Observe growing vortex both downstream and **upstream** from the cylinder and how it changes its shape w. r. t. We and velocity profile around the cylinder.

Effect of λ on *drag* for Oldroyd-B Combo 1 model

Before further investigation of this different behavior, we check impact of $\lambda > 0$ on the solution by looking at *drag* dependence w. r. t. *We* for varying λ. Moreover, we set $\beta = 0$ and $\alpha = 0.01$. As can be seen from the Figure (4.13), $\lambda > 0$ spoils the stabilization over edges until we reach λ^*, however $\lambda \approx \lambda^*$ affect *drag* greatly. Note that stabilization over edges does not work for $We > 2.1$ and that without both stabilizations, we are not able to reach even $We = 0.6$. Also note, that for $\lambda = 0$ the comparison with the benchmarks was successfully done in my bachelor thesis Cach [2021].

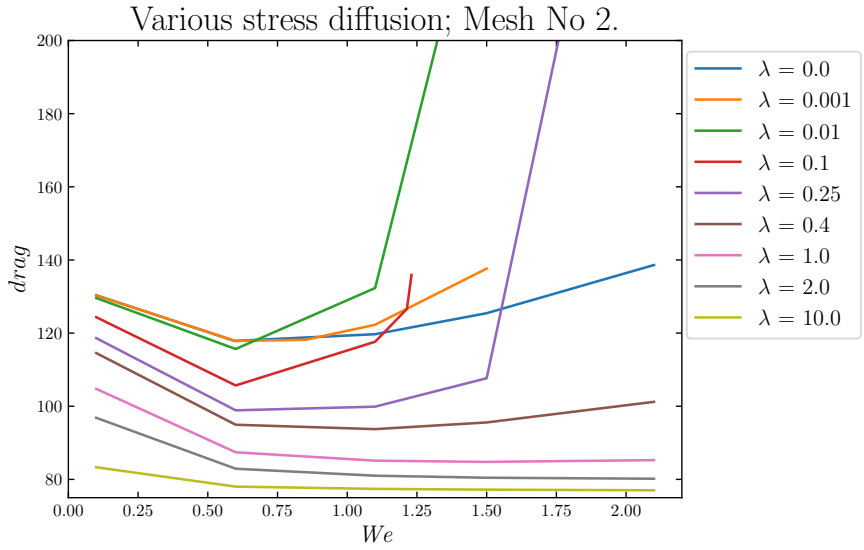

Figure 4.13: Plot for Oldroyd-B Combo 1 model ($\beta = 0$, $\alpha = 0.01$) of *drag* versus *We* for varying λ.

Effect of β on *drag* for Oldroyd-B Combo 1 model

Now, we fix $\lambda = 2.0$ and study *drag* dependence w. r. t. *We* for varying β. Looking at Figure (4.14), one can state that all convex combination of energies given by β are physically relevant, however, there is qualitatively different behavior for $\beta \to 1$.

Note, that there is no bound for *We*, one can proceed for larger *We* than plotted, if the sufficient λ is chosen. This we demonstrate by computing on Mesh No. 3. See Figure (4.15), where for $\beta = 0$ we fix $\lambda = 0.5$ and for $\beta = 0.99$ we set $\lambda = We/10 + 0.1$ (proper fit of obtained data leads to the $\lambda = 0.075\,We + 0.11$, hovewer, we overestimate this fit in order to make sure that the simulation will work for untested high *We*) as it is much cheaper than solving for λ^* for each *We*. Note that we use the very same fit for $\beta = 0.3$, otherwise solution does not converge. This is due to the fact that the vortex for such β eventually grows to the same size with given *We* as for $\beta = 0.99$.

However, it allows us to simply solve for high *We* and plot streamlines in the domain colored by velocity magnitude with nearly as small stress diffusion as possible and investigate flow properly, see Figure (4.16), see Figure (4.18) (compare formation of vortices with $\beta = 0.2$ (Figure (4.10))) and Figure (4.19).

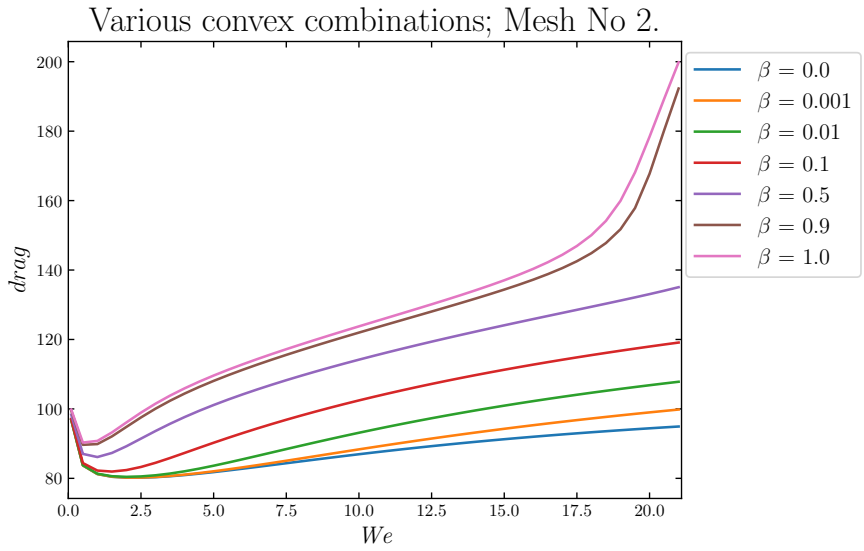

Figure 4.14: Plot for Oldroyd-B Combo 1 model ($\lambda = 2.0$) of *drag* versus *We* for varying β.

For $\beta = 0$ we do not observe any vortices upstream from the cylinder even for very high *We*. For $\beta = 0.99$ we observe shift of vortex towards the symmetry axis (compare with Figure (4.12)), which is connected with *drag* drop at $We \approx 3$, see Figure (4.15). For higher *We*, vortex is growing upstream. One can measure upstream vortex size as the distance on x-axis at $y = 0$ from the cylinder to the point where the velocity changes its direction, i.e., $v_x = 0$. We observe that vortex stops growing at $We \approx 200$, see Figure (4.17), where the error is given by edge length in the specific part of the mesh.

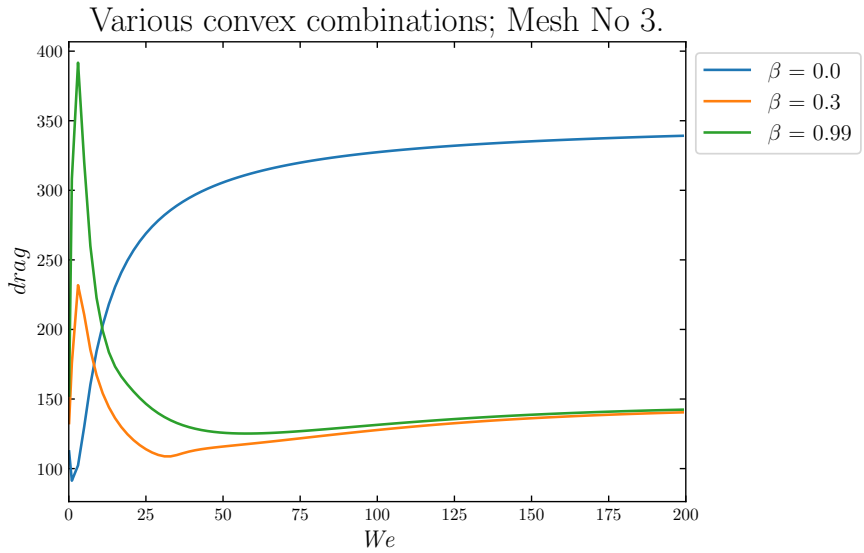

Figure 4.15: Plot for Oldroyd-B Combo 1 model ($\beta = 0 : \lambda = 0.5$, $\beta \in \{0.3, 0.99\} : \lambda = We/10 + 0.1$) of *drag* versus *We* for varying β.

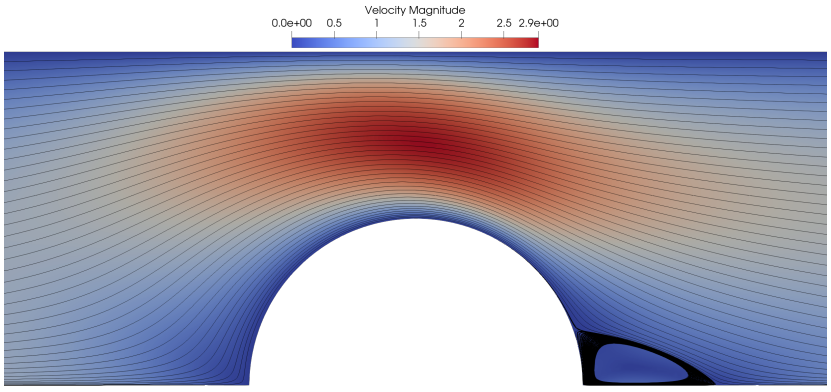

(a) For $\beta = 0$ and $We = 5$.

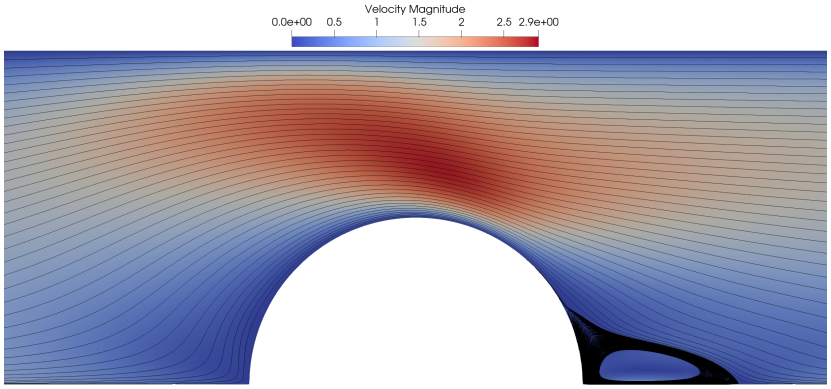

(b) For $\beta = 0$ and $We = 200$.

Figure 4.16: Plot of streamlines over velocity magnitude for Oldroyd-B Combo 1 model. Observe growing vortex downstream from the cylinder. Also notice, that for $\beta = 0$ there is no upstream vortex even for huge $We = 200$.

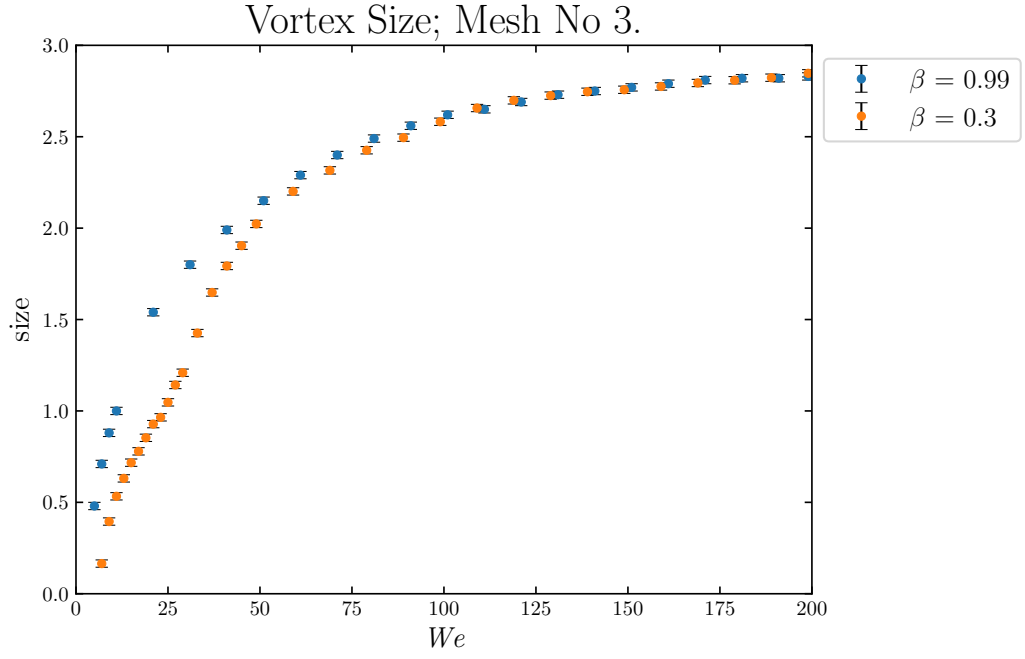

Figure 4.17: Plot for Oldroyd-B Combo 1 model ($\beta \in \{0.3, 0.99\}$, $\lambda = We/10 + 0.1$) of upstream vortex size versus We.

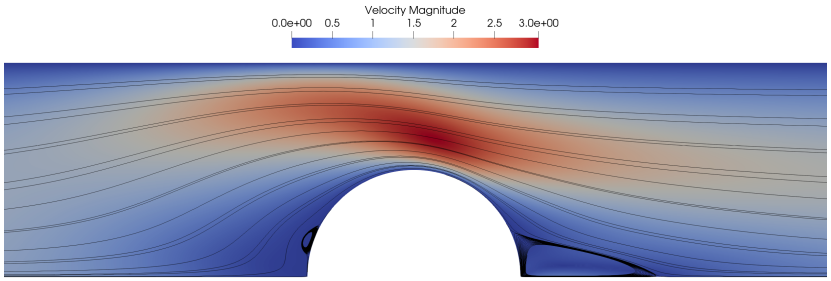

(a) For $\beta = 0.3$ and $We = 5$.

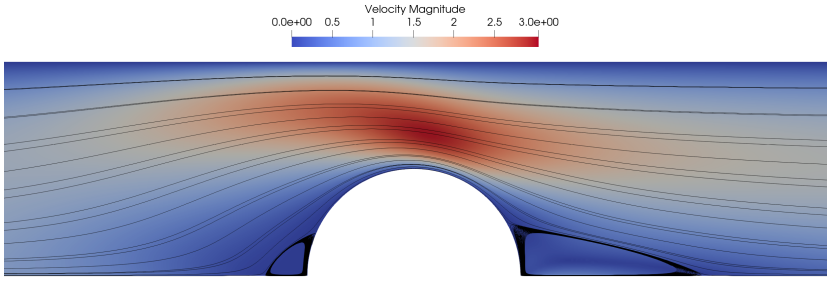

(b) For $\beta = 0.3$ and $We = 10$.

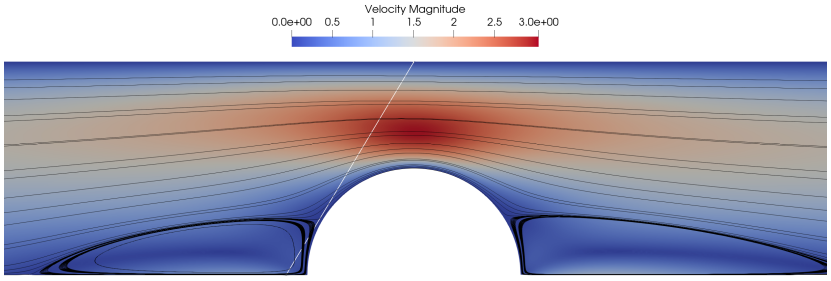

(c) For $\beta = 0.3$ and $We = 100$.

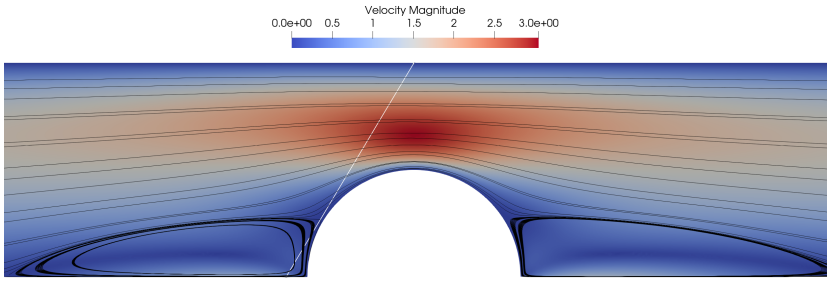

(d) For $\beta = 0.3$ and $We = 200$.

Figure 4.18: Plot of streamlines over velocity magnitude for Oldroyd-B Combo 1 model. Observe growing vortex both downstream and **upstream** from the cylinder.

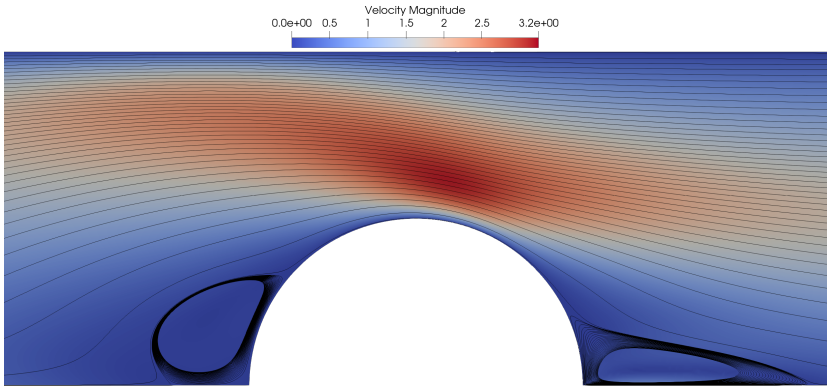

(a) For $\beta = 0.99$ and $We = 5$.

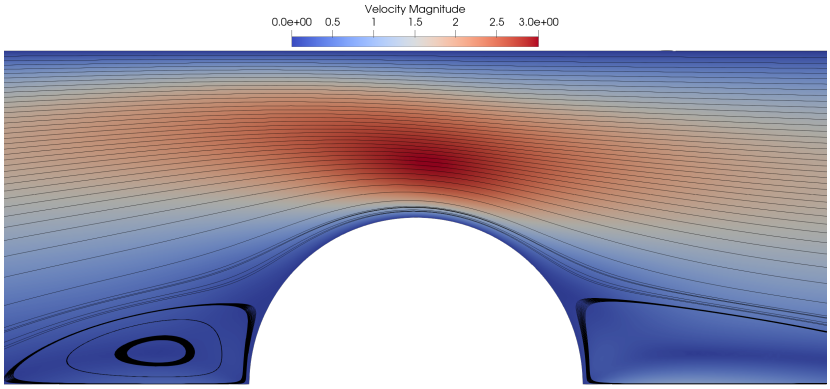

(b) For $\beta = 0.99$ and $We = 21$.

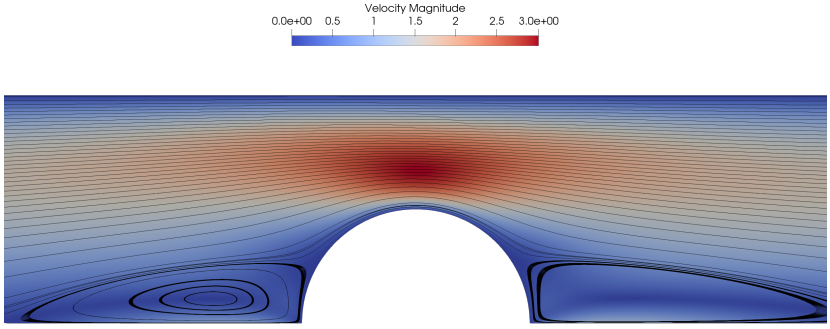

(c) For $\beta = 0.99$ and $We = 100$.

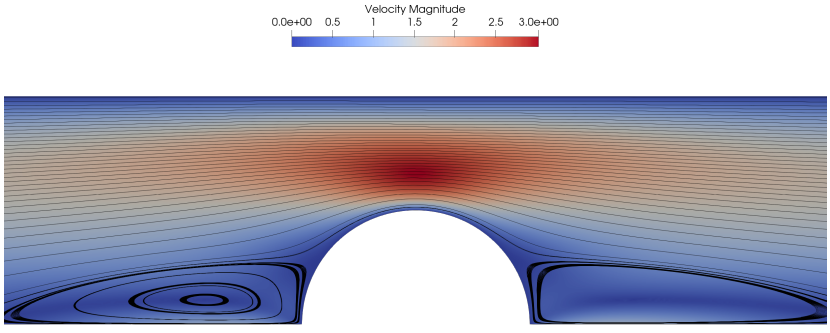

(d) For $\beta = 0.99$ and $We = 200$.

Figure 4.19: Plot of streamlines over velocity magnitude for Oldroyd-B Combo 1 model. Observe growing vortex both downstream and **upstream** from the cylinder.

Oscillations of λ^* during linear growth for Oldroyd-B Combo 1 model

Regarding the oscillations in the plot of λ^* w. r. t. *We* that starts to appear for $\beta \geq 0.9$ and high *We*, see Figure (4.8). On the mesh No. 3 for $\beta = 1$ we compute very same procedure for $\beta = 1$ and compare results with the results obtained on Mesh No. 2, see Figure (4.20). We observe very same jump for $We \in (1.5, 1.6)$. Moreover, slope of the function is the same for finer mesh and we observe similar oscillation for $We > 15$ as in the previous case.

By comparison of the plots of streamlines on the Mesh No. 3 during the oscilation, see Figure (4.21), we observe differently shaped vortices. This means that the solution for high *We* is very sensitive on the chosen continuation method, which can face difficulties around real λ^* where the stationary solution may stops to exist.

This can be explain by several reasons. Recall that the main idea of continuation method is to follow the curve in the space of a solution parametrized by chosen parameter and approach convergent neighborhood of the endpoint of the curve. However, following situations may occur: a) Continuation method may contain bifurcation that results into non-uniqueness of the solution. And we may follow different solutions for different *We*. b) Trajectory of the solution may be discontinuous in the sense, that there exists blow-up, i.e. there exist an interval $I \subset [\lambda^*, \lambda_0]$ s.t. $\lambda^* \notin I$ for which solution does not exist. And our continuation method may not use step large enought to cross this interval. Hence with our approach we may not find the smallest λ. Such research exceeds this work, and we suggest this direction as another possible topic of interest.

Lastly, we observe basic turbulence behaviour. If the vortex surrounds large portion of surface of the obstacle (cylinder), then the *drag* is several times larger than if the vortex is positioned before the cylinder and touches the obstacle only on the small amount of its surface, see peaks of *drag* in the Figure (4.22), which corresponds to the first formation of the vortex (Figure (4.12) d)) and the differently shapes vortices during oscilations of λ^* (Figure (4.21)).

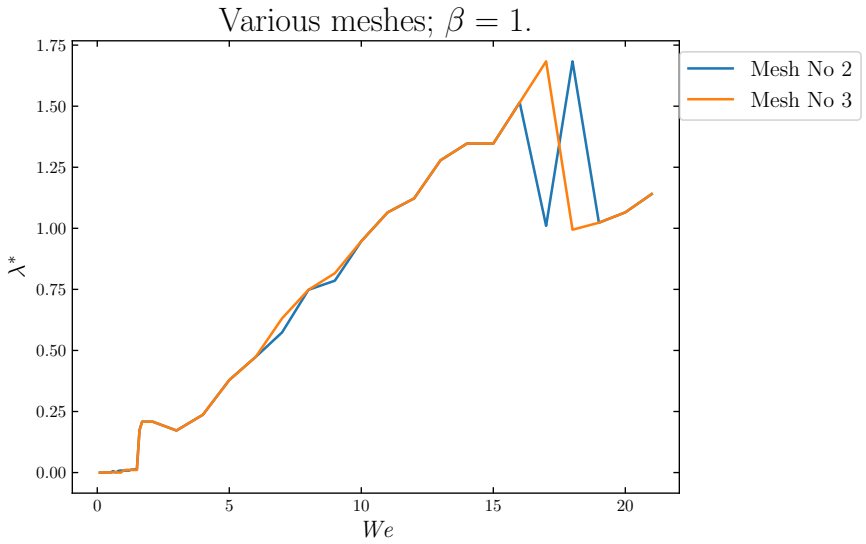

Figure 4.20: Plot for Oldroyd-B Combo 1 model ($\beta = 1$) of λ^* versus *We*.

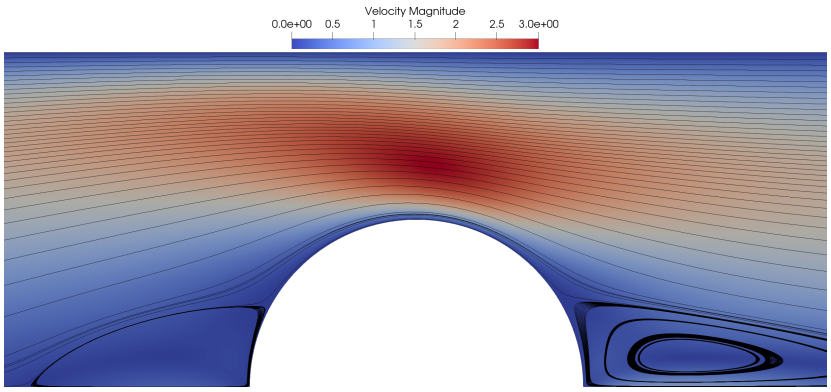

(a) For $\beta = 1$ and $We = 17$, $\lambda^* \approx 1.68$. Here $drag = 158.48$.

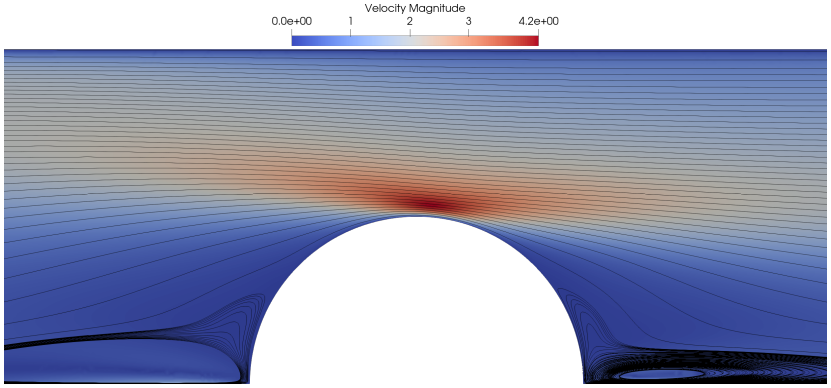

(b) For $\beta = 1$ and $We = 18$, $\lambda^* \approx 0.99$. Here $drag = 3957.58$.

Figure 4.21: Plot of streamlines over velocity magnitude for Oldroyd-B Combo 1 model. Observe change of the vortex shape with a small change of We but a significant drop of λ^*.

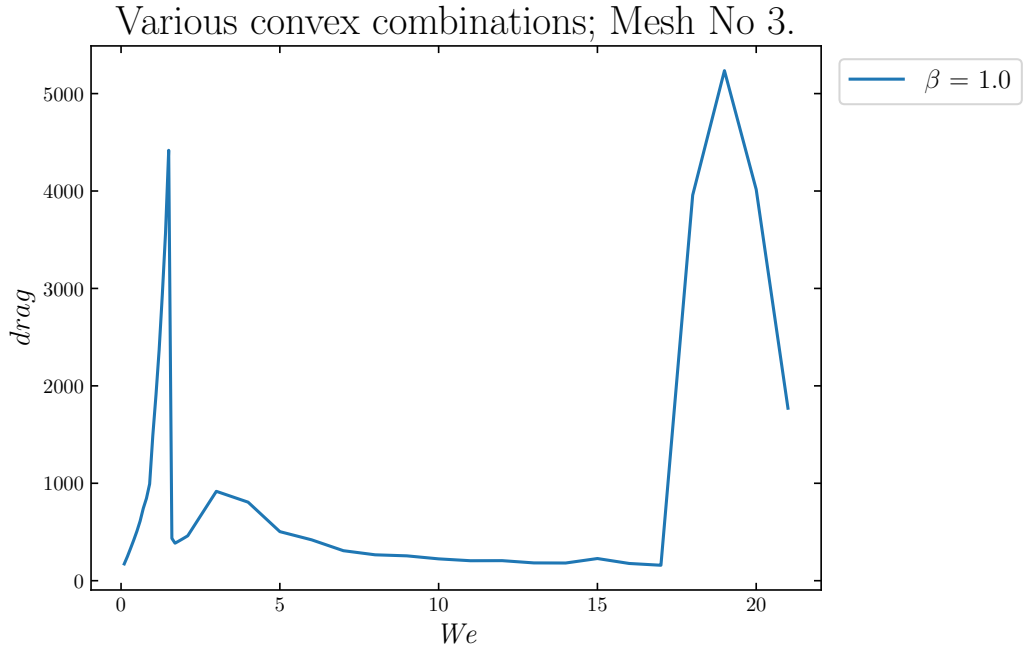

Figure 4.22: Plot for Oldroyd-B Combo 1 model ($\beta = 1$, $\lambda = \lambda^*$) of $drag$ versus We.

4.1.9 Giesekus Combo 2 model

In this section, we investigate the case of $\delta_1 \neq 0$, $\delta_2 \neq 0$, and we set $\delta_1 = \delta_2 = 1/We$, see the third line of Table (4.2). Note that this is a special case as in general one can have $\delta_1 \neq \delta_2$. Also, this model may be seen as a combination of Giesekus Combo 1 model and Oldroyd-B Combo 1 model. However we call it Giesekus Combo 2 as there is quadratic term in the rate-type equation that is typical for Giesekus-like models.

Finding minimal λ for Giesekus Combo 2 model

Looking on graph of λ^* versus We for varying β, see Figure (4.23), one can observe similarities with Giesekus Combo 1 model, which means that either the instabilities of Oldoyd-B Combo 1 model are shifted to the highest We or none will even arise.

Effect of β on $drag$ for Giesekus Combo 2 model

For $\lambda = 0.011$ we plot $drag$ versus We, see Figure (4.24), as the λ^* does not change significantly and one can also observe effect of λ on $drag$ in one plot. The dependence resembles Giesekus Combo 1 model with faster growth for higher We and β inherited from Oldroyd-B Combo 1 model. We get the best from both worlds.

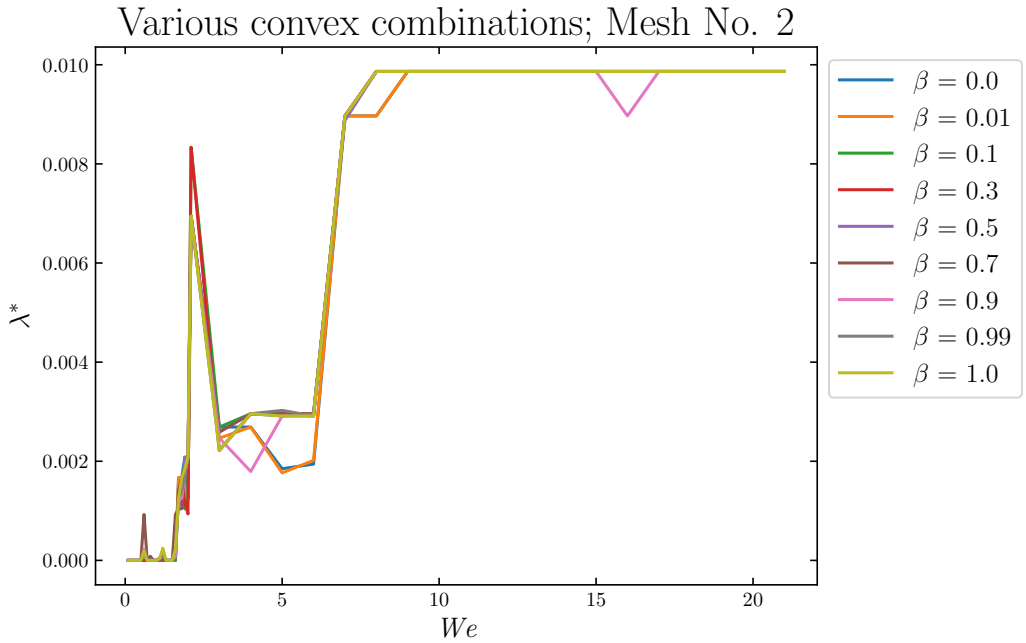

Figure 4.23: Plot for Giesekus Combo 2 model of λ^* versus We for varying β.

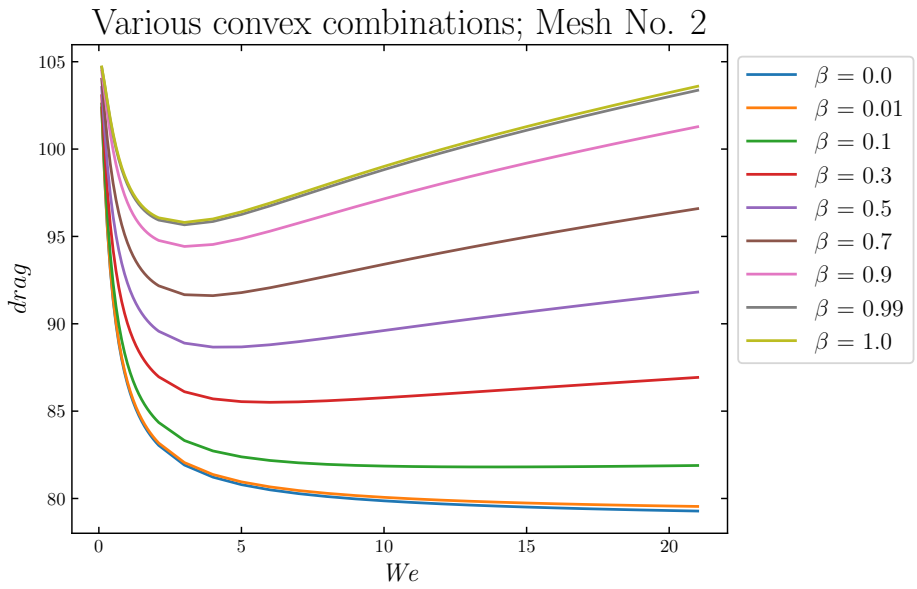

Figure 4.24: Plot for Giesekus Combo 2 model ($\lambda = 0.011$) of *drag* versus *We* for varying β.

4.1.10 Oldroyd-B Combo 2 model

Finally, let us investigate impact of different objective derivatives. Above all we are interested in the transition between Jaumann-Zaremba derivative to upper convected derivative, i.e., $a \in [0, 1]$. As discussed in the Section 4.1.6 Fluid model parameters, for $a = 0$, there is no extra stress in the Cauchy stress tensor, hence the solution corresponds to the Navier-Stokes. In this section, we use parameters in the fourth line of the Table (4.2) corresponding to this model. Remaining parameters are specified later.

Finding minimal λ for Oldroyd-B Combo 2 model

For $a \to 1$ flow starts to exhibit viscoelastic properties, see Figure (4.25) of λ^* versus *We*, as there is needed $\lambda^* > 0$. Results were obtained using parameters in the fourth line of the Table (4.2). Moreover notice that there is either bound for a for which the viscoelasticity comes to play or for small a the viscoelasticity takes effect for higher *We* than plotted.

Effect of a on *drag* for Oldroyd-B Combo 2 model

Finally, for $\lambda = 0.4 > \lambda^*$ we plot *drag* versus *We*, see Figure (4.26). We observe that for $\beta = 0$ the *drag* does not depend greatly on *We* until $a \to 1$. This must be connected with the properties of derivative itself in the rate-type equation as for $a = 0.8$ there is no growth of *drag* even thought that the difference between values of $a \in \{0.8, 1.0\}$ in the extra stress of the Cauchy stress are relatively close to each other and may be compensated by a small change of elastic modulus G.

Also notice, that the results for $\beta = 0$, $a = 1$ are different from the results in the Figure (4.14) even though for this choice of parameters the Oldroyd-B Combo 2 model and Oldroyd-B Combo 1 model are the same. That is because the choice

of λ is different and it highlights how sensitive the solution is to the magnitude of the stress diffusion.

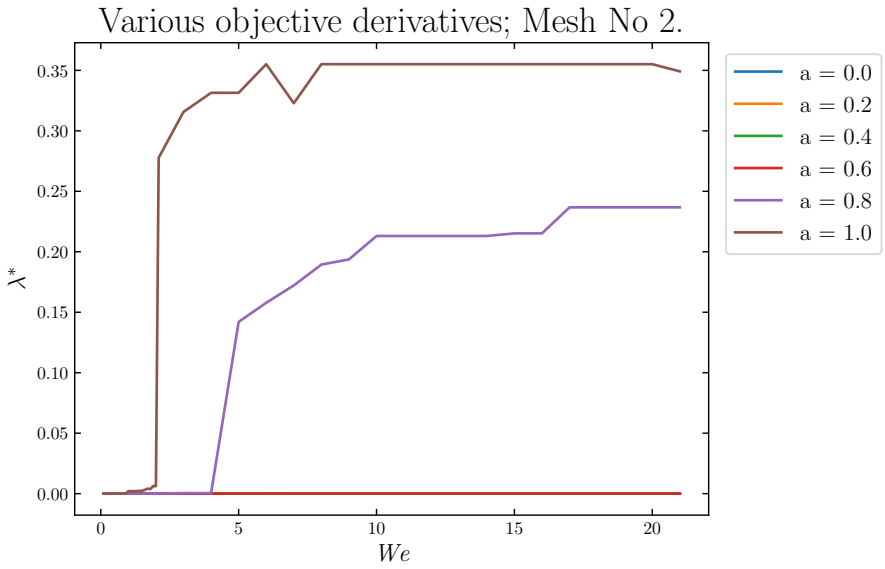

Figure 4.25: Plot for Oldroyd-B Combo 2 model, i.e. transition of Jaumann-Zaremba to upper convected derivative, ($\beta = 0$) of λ^* versus *We*.

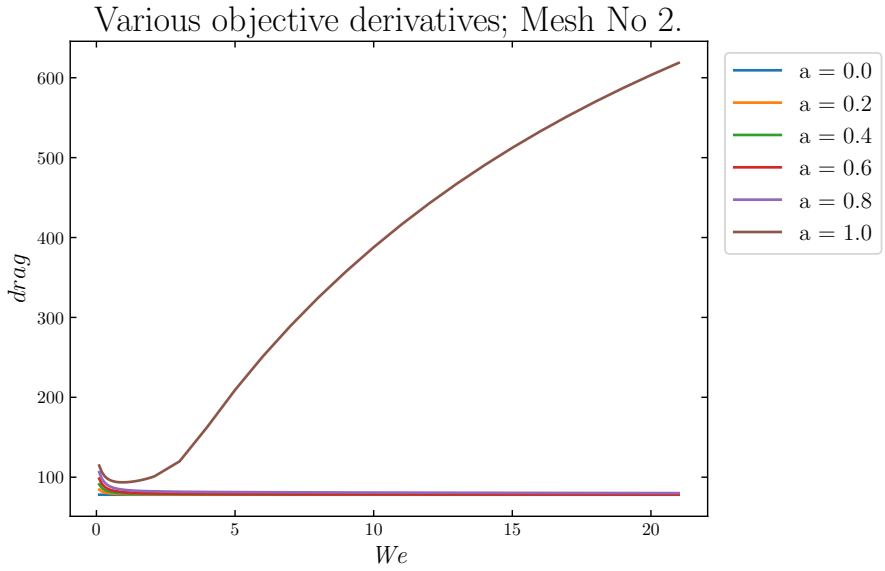

Figure 4.26: Plot for Oldroyd-B Combo 2 model, i.e. transition of Jaumann-Zaremba to upper convected derivative ($\beta = 0$, $\lambda = 0.4$) of *drag* versus *We*.

4.1.11 Conclusion for the flow past the cylinder

Giesekus Combo 1 model, Giesekus Combo 2 model

For the Giesekus Combo 1 model and the Giesekus Combo 2 model, we observed that the **stress diffusion** may play a role as the stabilization, instead of stabilization over edges, since minimal parameter λ needed for solver to converge is relatively small and the change of the solution due to this stabilization is negligible. Moreover, we observed that there is a smooth transition of $\beta \to 0$ and $\beta \to 1$, hence the weak solution existence theory could be expanded for these values.

Oldroyd-B Combo 1 model

For the Oldroyd-B Combo 1 model, we observed that the **stress diffusion is essential** for the problem, as the minimal λ needed for solver to converge to the steady state is huge and such values affect the solution greatly.

Moreover, for $\beta \to 1$ we observed together with downstream instability from the cylinder the **upstream instability** from the cylinder of the flow in the form of vortex. Despite the surprising nature of this behavior, it was already experimentally observed such upstream instable behavior for viscoelastic fluids in the works of Shi et al. [2015] and Hopkins et al. [2022]. However, in these works their authors observed vanishing of the downstream vortex when the upstream vortex appeared. This may be due to the fact that their experiments were performed for smaller Reynolds number than our benchmark was defined. We suggest further investigation of this behavior for lesser Reynolds numbers by means of time-dependent simulations also.

Furhermore, for $\beta \to 1$ the minimal λ growed linearly with *We* and we attribute this behavior to the mentioned upstream instability of the flow.

Nevertheless, for $\beta \to 0$ the situation was better in the terms of λ as there was only one jump w. r. t. *We* in the minimal λ connected with the formation of downstream vortices. And, after that, the value stayed approximatelly constant.

Oldroyd-B Combo 2 model

For the Oldroyd-B Combo 2 model we observed that transition of Jaumann-Zaremba to upper convected derivative is essentail for the viscoelastic effects. And that was not due the fact that the parameter from the derivative also appears in the extra stress in the Cauchy stress tensor as there may be compensated by the elastic modulus.

It can be seen from the computation of normal stress differences in a simple shear flow (details are given at the beggining of the next chapter). Solving the equation:

$$-a(\mathbb{D}\mathbb{B}_{\kappa_{p(t)}} + \mathbb{B}_{\kappa_{p(t)}}\mathbb{D}) - (\mathbb{W}\mathbb{B}_{\kappa_{p(t)}} - \mathbb{B}_{\kappa_{p(t)}}\mathbb{W}) + \delta_1(\mathbb{B}_{\kappa_{p(t)}} - \mathbb{I}) = \mathbb{O}, \tag{4.3}$$

given the velocity field $\mathbf{v} = (v(y), 0, 0)^T$, leads to the following:

$$\mathbb{B}_{\kappa_{p(t)}} = \begin{pmatrix} \frac{(a+1)(v')^2+\delta_1^2}{(1-a)(1+a)(v')^2+\delta_1^2} & \frac{av'\delta_1^2}{(1-a)(1+a)(v')^2+\delta_1^2} & 0 \\ \frac{av'\delta_1^2}{(1-a)(1+a)(v')^2+\delta_1^2} & 1+\frac{(a-1)a(v')^2}{(1-a)(1+a)(v')^2+\delta_1^2} & 0 \\ 0 & 0 & 1 \end{pmatrix} \overset{a=0}{=} \begin{pmatrix} 1 & 0 & 0 \\ 0 & 1 & 0 \\ 0 & 0 & 1 \end{pmatrix}. \tag{4.4}$$

4.2 Axisymmetric problems with a free surface

Now we turn our interest to the more complex problems – axisymmetric viscoelastic problems with a free surface. Firstly, for such problem we need to rewrite equations in the cylindrical coordinates. Secondly, we need to introduce a method for flows with a free surface. We choose arbitrary Lagrangian-Eulerian (ALE) method. Both components for our simulations of rod climbing effect will be tested separately. For all simulations, we focus on classical Oldroyd-B model and Giesekus model as these models exhibit non-zero normal stress differences in a simple shear flow.

Presence of non-zero normal stress differences in a simple shear flow for viscoelastic model (3.1)

We need to investigate constitutive relation for Cauchy stress tensor $\mathbb{T}$ for prescribed velocity $\mathbf{v} = (v(y), 0, 0)^T$. We focus on special case of Oldroyd upper convected derivative ($a = 1$) and $\beta = 0$. Notice that for the computation of normal stress differences $N_1 := T_{11} - T_{22}$, $N_2 := T_{22} - T_{33}$, and $N_3 := T_{33} - T_{11}$, it suffices to solve the stationary rate-type equation for the $\mathbb{B}_{\kappa_{p(t)}}$:

$$\begin{aligned} \mathbb{T} &= -p\mathbb{I} + 2\nu\mathbb{D} + G(\mathbb{B}_{\kappa_{p(t)}} - \mathbb{I}), \\ -\mathbb{L}\mathbb{B}_{\kappa_{p(t)}} - \mathbb{B}_{\kappa_{p(t)}}\mathbb{L}^T + \delta_1(\mathbb{B}_{\kappa_{p(t)}} - \mathbb{I}) + \delta_2(\mathbb{B}^2_{\kappa_{p(t)}} - \mathbb{B}_{\kappa_{p(t)}}) &= \mathbb{O}, \end{aligned} \tag{4.5}$$

as the pressure part does not contribute to the differences and $\mathbb{D}$ has zero diagonal entries. It leads to the non-linear system of 6 equations for 6 independent entries of the $\mathbb{B}_{\kappa_{p(t)}}$:

$$\begin{aligned} -\begin{pmatrix} B_{12}v' & B_{22}v' & B_{23}v' \\ 0 & 0 & 0 \\ 0 & 0 & 0 \end{pmatrix} - \begin{pmatrix} B_{12}v' & 0 & 0 \\ B_{22}v' & 0 & 0 \\ B_{23}v' & 0 & 0 \end{pmatrix} + \delta_1 \begin{pmatrix} B_{11}-1 & B_{12} & B_{13} \\ B_{12} & B_{22}-1 & B_{23} \\ B_{13} & B_{23} & B_{33}-1 \end{pmatrix} \\ +\delta_2(\mathbb{B}^2_{\kappa_{p(t)}} - \mathbb{B}_{\kappa_{p(t)}}) = \mathbb{O}. \end{aligned} \tag{4.6}$$

With general constants δ_1, δ_2 the Wolfram Mathematica 13 function `Solve[]` gives 8 solutions with common results $B_{13} = 0$, $B_{23} = 0$, and $B_{33} \in \{1, -\delta_1/\delta_2\}$. Other entries are very non-trivial. In the next section we use model with the choice $\delta_1 = \delta_2 =: \delta$, which simplifies the result as follows:

$$\begin{aligned} B_{11} &= \pm\frac{\sqrt{2}\sqrt{-v'\delta - \frac{\delta^3}{v'} - v'\sqrt{v'^2+\delta^2} \pm \frac{\delta^2\sqrt{v'^2+\delta^2}}{v'}}}{\sqrt{v'}\sqrt{\delta}}, \\ B_{12} &= \frac{-\delta \pm \sqrt{v'^2+\delta^2}}{v'}, \\ B_{22} &= \pm\frac{\sqrt{2}\sqrt{\delta}\sqrt{-v'\delta - \frac{\delta^3}{v'} - v'\sqrt{v'^2+\delta^2} \pm \frac{\delta^2\sqrt{v'^2+\delta^2}}{v'}}}{\sqrt{v'}\sqrt{v'^2+\delta^2}}, \\ B_{33} &= 1, \end{aligned} \tag{4.7}$$

with 8 correct combinations of $\pm$. However, we choose such solution where $\mathbb{B}_{\kappa_{p(t)}}$ is positive definite. This leads to the non-zero N_1, N_2, N_3 for a. e. choices of δ_1, δ_2, $v(y)$.

Futhermore, we are interested in the classical Oldroyd-B model, i. e., $\delta_1 \neq 0$, $\delta_2 = 0$ which makes the system linear, and the solution is unique:

$$\mathbb{B}_{\kappa_{p(t)}} = \begin{pmatrix} 1 + 2\frac{(v')^2}{\delta_1^2} & \frac{v'}{\delta_1} & 0 \\ \frac{v'}{\delta_1} & 1 & 0 \\ 0 & 0 & 1 \end{pmatrix} \quad \Longrightarrow \; N_1 = 2\frac{(v')^2}{\delta_1^2},\; N_2 = 0,\; N_3 = -2\frac{(v')^2}{\delta_1^2}. \quad (4.8)$$

The normal stress differences are non-zero as the velocity gradient in the simple shear flow is non-zero by definition.

4.2.1 Axisymmetric shear flow

In this simulation, we consider a rotating cylinder immersed in the center of cylindrical container filled with viscoelastic fluid and covered by a lid, see Figure (4.27). For this simulation, we use dimensionless quantities and we set the outer radius $R_{out} = 0.75$, the inner radius $R_{in} = 0.25$, the outer height $H_{out} = 0.9$, the inner height $H_{in} = 6/20 H_{out}$. We consider on all walls to be no-slip except tangent component of the velocity on the inner cylinder, which is equivalent with rotating cylinder with angular velocity $\omega = 0.2$ on whose surface the liquid adheres. Based on such setting, we assume flow to be axisymmetric and we solve for steady solution. Hence we formulate problem in the cylindrical coordinates.

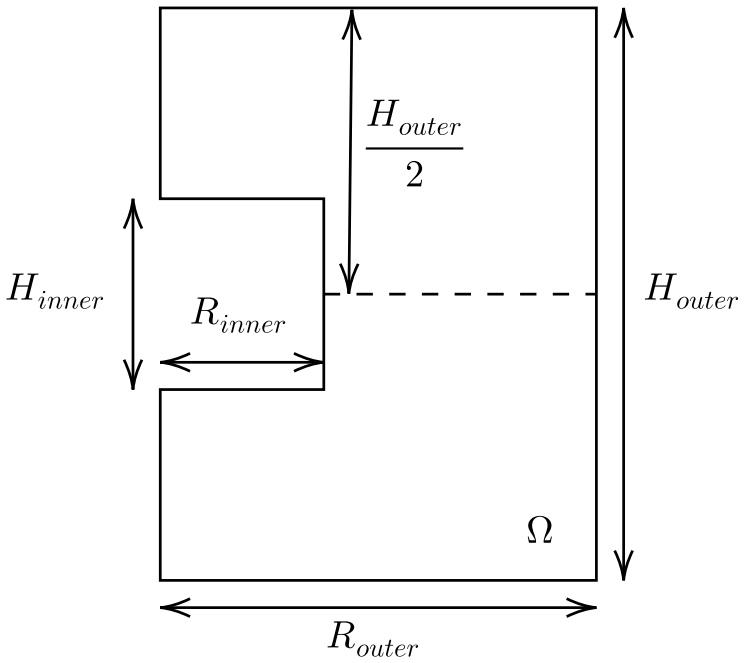

Figure 4.27: Sketch of the computational domain for the axisymmetric shear flow.

Cylindrical coordinates for axisymmetric problem

Let us denote the distance from the origin by $r \geq 0$, the signed angle from the unit vector in the direction of the positive x-axis by $\varphi \in [0, 2\pi)$ and the z-axis remains the same. We assume the most general axisymmetric setting, i.e., $\partial A/\partial\varphi = 0$,

hence the quantity (pressure, velocity and the left Cauchy-Green tensor) is in the form $A = A(r, z)$. Moreover, we assume the most general form of the velocity:

$$\mathbf{v}(r, z) = (v_r, v_\varphi, v_z)^T. \tag{4.9}$$

All we need is to convert gradients from cartesian coordinates to the polar coordinates and use the axisymmetric assumption. Let us start with the gradient of a scalar field:

$$\nabla p(r, z) = (\partial_r p, 0, \partial_z p)^T. \tag{4.10}$$

The gradient of a vector field is given by:

$$\nabla \mathbf{v}(r, z) = \begin{pmatrix} \partial_r v_r & -\frac{1}{r} v_\varphi & \partial_z v_r \\ \partial_r v_\varphi & \frac{1}{r} v_r & \partial_z v_\varphi \\ \partial_r v_z & 0 & \partial_z v_z \end{pmatrix}. \tag{4.11}$$

Finally, the gradient of a tensor field is given by:

$$\nabla \mathbb{B}(r, z) = \partial_r \mathbb{B} \otimes \mathbf{e}_r - \frac{1}{r} \begin{pmatrix} 2B_{r\varphi} & B_{\varphi\varphi} - B_{rr} & B_{\varphi z} \\ B_{\varphi\varphi} - B_{rr} & -2B_{r\varphi} & -B_{rz} \\ B_{\varphi z} & -B_{rz} & 0 \end{pmatrix} \otimes \mathbf{e}_\varphi + \partial_z \mathbb{B} \otimes \mathbf{e}_z, \tag{4.12}$$

where $\mathbf{e}_r$, $\mathbf{e}_\varphi$, $\mathbf{e}_z$ are basis vectors of cylindrical coordinates and

$$\partial_i \mathbb{B}(r, z) = \begin{pmatrix} \partial_i B_{rr} & \partial_i B_{r\varphi} & \partial_i B_{rz} \\ \partial_i B_{r\varphi} & \partial_i B_{\varphi\varphi} & \partial_i B_{\varphi z} \\ \partial_i B_{rz} & \partial_i B_{\varphi z} & \partial_i B_{zz} \end{pmatrix}. \tag{4.13}$$

One can also precompute the convective term:

$$\mathbf{v}(r, z) \cdot \nabla \mathbb{B}(r, z) = \\ \begin{pmatrix} \mathbf{v} \cdot \nabla B_{rr} - \frac{2v_\varphi}{r} B_{r\varphi} & \mathbf{v} \cdot \nabla B_{r\varphi} - \frac{v_\varphi}{r}(B_{\varphi\varphi} - B_{rr}) & \mathbf{v} \cdot \nabla B_{rz} - \frac{v_\varphi}{r} B_{\varphi z} \\ \mathbf{v} \cdot \nabla B_{r\varphi} - \frac{v_\varphi}{r}(B_{\varphi\varphi} - B_{rr}) & \mathbf{v} \cdot \nabla B_{\varphi\varphi} + \frac{2v_\varphi}{r} B_{r\varphi} & \mathbf{v} \cdot \nabla B_{\varphi z} + \frac{v_\varphi}{r} B_{rz} \\ \mathbf{v} \cdot \nabla B_{rz} - \frac{v_\varphi}{r} B_{\varphi z} & \mathbf{v} \cdot \nabla B_{\varphi z} + \frac{v_\varphi}{r} B_{rz} & \mathbf{v} \cdot \nabla B_{zz} \end{pmatrix}, \tag{4.14}$$

where the gradients on the right hand side are axisymmetric gradients of a scalar field.

Finally, notice that the integrals over 3D cylindrical domain $\hat{\Omega}$ for axisymmetric integrands $f(r, z)$ are simplified:

$$\int_{\hat{\Omega}} f(r, z)\, dV = \int_0^{2\pi} \int_\Omega r f(r, z)\, dr d\varphi dz = 2\pi \int_\Omega r f(r, z)\, dr dz, \tag{4.15}$$

where Ω is the 2D domain corresponding to the cylindrical symmetry of $\hat{\Omega}$. Integrals over surfaces $\hat{\Gamma}$ of the 3D cylindrical domain $\hat{\Omega}$ on the hyperplanes (r, φ) and (φ, z) are simplified in the same manner:

$$\int_{\hat{\Gamma}} f(r, z)\, dS(r, \varphi) = \int_0^{2\pi} \int_{R_1}^{R_2} r f(r, z)\, dr d\varphi = 2\pi \int_{R_1}^{R_2} r f(r, z)\, dr, \tag{4.16}$$

$$\int_{\hat{\Gamma}} f(r, z)\, dS(\varphi, z) = \int_0^{2\pi} \int_{Z_1}^{Z_2} r f(r, z)\, d\varphi dz = 2\pi \int_{Z_1}^{Z_2} r f(r, z)\, dz. \tag{4.17}$$

Model and parameters

For this problem we work with dimensionless quantities and choose a combination of Giesekus and Oldroyd-B model, see section 4.1.9. We set $\delta_1 = \delta_2 = 1/We$, $a = 1$, $\beta = 0$ and $\lambda = 0$. Moreover, we set $G = 0.1$, Reynolds number $Re := UL/\nu = 5.0$, where U is a characteristic velocity, L is a characteristic lenght and we modify Cauchy-stress tensor from the set of equations (3.1) as follows:

$$\mathbb{T} = -\frac{p}{Re}\mathbb{I} + \frac{2}{Re}\mathbb{D} + 2aG((1-\beta)(\mathbb{B}_{\kappa_{p(t)}} - \mathbb{I}) + \beta(\mathbb{B}^2_{\kappa_{p(t)}} - \mathbb{B}_{\kappa_{p(t)}})). \tag{4.18}$$

Finally, $We \in [0.01, 1.0]$ we choose.

Numerical results

We compute on the fine mesh that leads to the 212 966 degrees of freedom (DoFs). Numerical results show the expected behavior, that for a sufficiently large We the secondary flows change direction as the elastic forces due to the presence of non-zero normal stress differences in a simple shear flow overcome viscous forces, see Figure 4.28.

Observe that the direction of the secondary flow for large We above the inner cylinder is in the direction of the positive z-axis. This indicates that these models should be able to capture the Weissenberg (rod climbing) effect. For simplicity we choose classical Oldroyd-B model for such simulation and we show that the computations are possible in the section bellow.

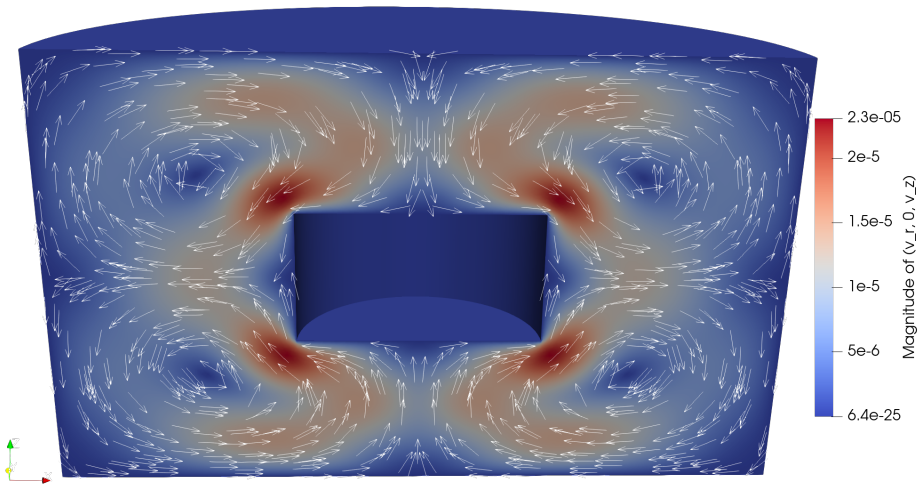

(a) We= 0.01.

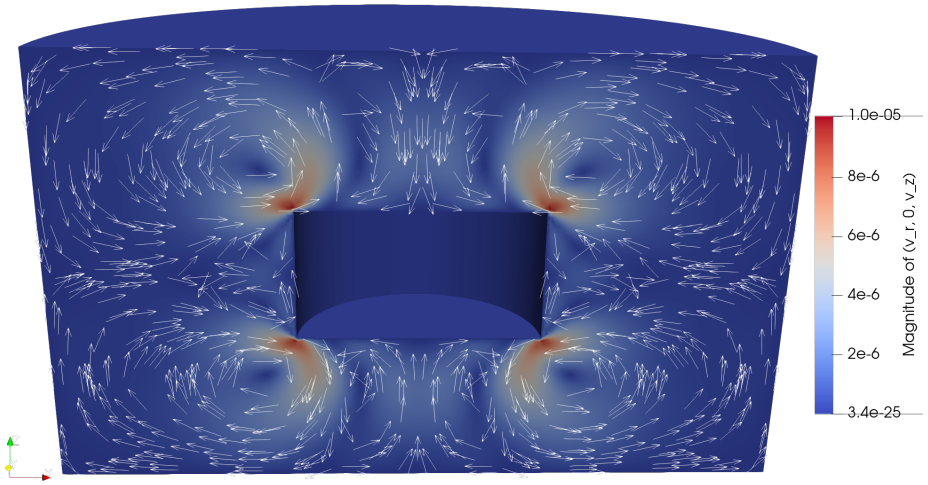

(b) *We*= 0.4.

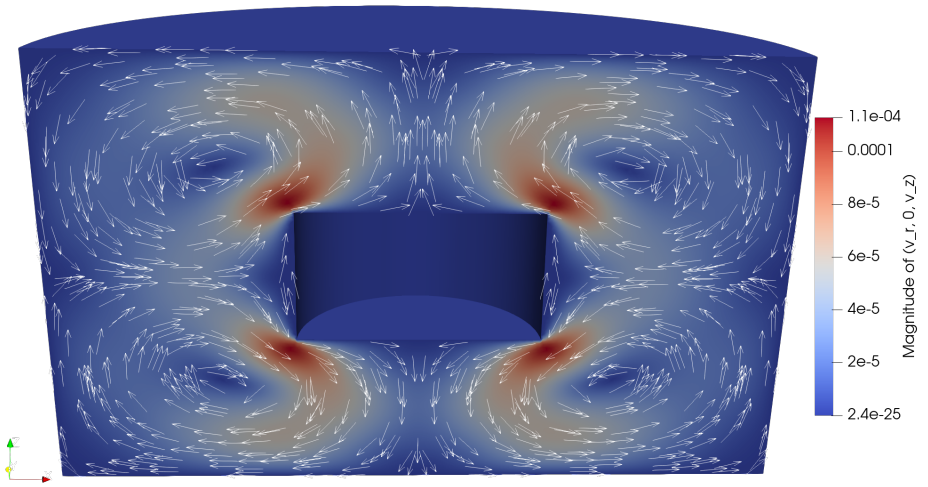

(c) *We*= 1.0.

Figure 4.28: Plots of the rotationaly extruded domain colored by the magnitude of the 2D velocity $\mathbf{v}_{2D}(r,z) = (v_r(r,z), 0, v_z(r,z))$ with the stream arrows of uniform size in every 10^{th} node. Notice different direction of vortices for highly viscoelastic flow. Direction changes around $We = 0.4$. Moreover, for such We there are four vortices in the one slice.

4.2.2 Pressing of the rectangular piece of viscoelastic material

In this simulation, we consider rectangular piece of viscoelastic material, which is infinitely long in the direction of z-axis. For this simulation, we use dimensionless quantities and we set the lenght of the rectangle $Len = 2$ and the width of the rectangle $Wid = 1$, see Figure 4.29. We consider boundary conditions on the boundary part of the rectangle, namely bottom to be no-slip wall, sides to be free-slip wall in y-direction and top to be a free surface, where we prescribe stress $T_{yy} = -0.5$ on the line segment Γ of the length of $Len/2$ centered in the middle. As we are interested purely in the classic Oldroyd-B model, we neglect the surface tension. Based on such setting, the free surface is going to deform, hence we need to compute on the time varying domain. This leads us to formulation of the problem with the use of ALE method.

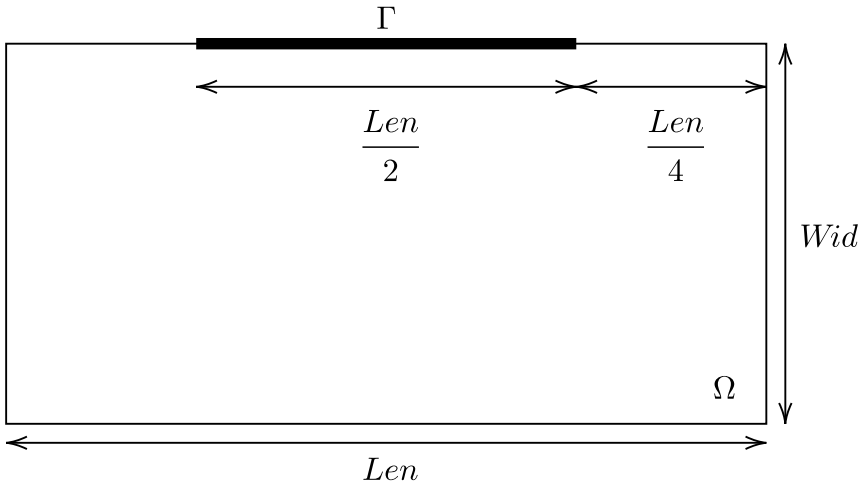

Figure 4.29: Sketch of the computational domain for the pressing of the viscoelastic rectangle.

Lagrangian formulation

From the technical point of view, to change the formulation is a straightforward task as we are using a robust finite element code (FEniCS) with a monolithic non-linear solver. Before we derive ALE formulation, it is instructive to start the derivation with a Lagrange formulation even though it is not suitable for our problem since every vertex in the mesh is a material point making the mesh prone to degenerate if the deformations contain vorticity. We follow the derivation by Tůma [2014] and extend it for our viscoelastic model.

We introduce a new variable physical deformation $\mathbf{u}$ and we identify the fixed computational mesh with the reference Lagrangian configuration κ_R (domain Ω_X), see Figure (1.1), Section 1.1. Now we connect deformation mapping with the physical deformation by setting:

$$\chi_{\kappa_R} : X \longrightarrow x := X + \mathbf{u}. \tag{4.19}$$

From the definion of Lagrangian velocity (1.2), deformation gradient (1.4) we compute:

$$\mathbf{V}(t,X) = \frac{\partial \mathbf{u}}{\partial t}(t,X), \tag{4.20}$$

$$\mathbb{F}_{\kappa_R} = \mathbb{I} + \nabla_X \mathbf{u}, \tag{4.21}$$

and we define $J := \det \mathbb{F}_{\kappa_R}$. Note, that we emphasize derivatives in the reference configuration by index ∇_X.

To transform the Eulerian weak formulation (3.14) into the Lagrangian, firstly, we substitute all derivatives with respect to x to derivatives with respect to X. Also, we need to transform the velocity gradient $\nabla \mathbf{v}$ and the material time derivatives:

$$\nabla_X \mathbf{V} = \frac{\partial \mathbf{V}(t, \chi_{\kappa_R}(t,X))}{\partial X} = \frac{\partial \mathbf{v}(t,x)}{\partial x}\frac{\partial \chi_{\kappa_R}}{\partial X} = (\nabla \mathbf{v})\mathbb{F}_{\kappa_R} \quad \Rightarrow \quad \nabla \mathbf{v} = (\nabla_X \mathbf{V})\mathbb{F}_{\kappa_R}^{-1}, \tag{4.22}$$

$$\left.\frac{\partial \alpha}{\partial t}\right|_X = \left.\frac{d\alpha(\chi_{\kappa_R}(t,X),t)}{dt}\right|_X = \left.\frac{\partial \alpha}{\partial t}\right|_x + \left.\frac{\partial \alpha}{\partial x}\frac{\partial \chi_{\kappa_R}}{\partial t}\right|_X = \dot{\alpha}. \tag{4.23}$$

Secondly, using integral substitution theorem we transform integrals over Ω to the integrals over Ω_X. Finally, we use Piola identity $\operatorname{div}_X \left((\det \mathbb{F}_{\kappa_R})\mathbb{F}_{\kappa_R}^{-T}\right) = 0$ in the balance of linear momentum:

$$\int_\Omega \operatorname{div} \mathbb{T} \cdot \varphi = \int_{\Omega_X} J(\nabla_X \mathbb{T})\mathbb{F}_{\kappa_R}^{-T} \cdot \varphi = \int_{\Omega_X} \operatorname{div}_X (J\mathbb{T}\mathbb{F}_{\kappa_R}^{-T}) \cdot \varphi \tag{4.24}$$

Altogether we obtain:

$$\begin{aligned}
\int_{\Omega_X} J \operatorname{tr}\left((\nabla_X \mathbf{V})\mathbb{F}_{\kappa_R}^{-1}\right)\psi = 0,\\
\int_{\Omega_X} J\rho\frac{\partial \mathbf{V}}{\partial t}\cdot\phi - \int_{\Omega_X} \operatorname{div}_X\left(J\mathbb{T}\mathbb{F}_{\kappa_R}^{-T}\right)\cdot\phi - \int_{\Omega_X} J\rho\mathbf{b}\cdot\phi = 0,\\
\mathbb{T} = -p\mathbb{I} + 2\nu\mathbb{D}_X + aG\left[(1-\beta)(\mathbb{B}_{\kappa_{p(t)}} - \mathbb{I}) + \beta(\mathbb{B}^2_{\kappa_{p(t)}} - \mathbb{B}_{\kappa_{p(t)}})\right],\\
\int_{\Omega_X} J\frac{\delta \mathbb{B}_{\kappa_{p(t)}}}{\delta t}\cdot\mathbb{A} + J\left[\delta_1(\mathbb{B}_{\kappa_{p(t)}} - \mathbb{I}) + \delta_2(\mathbb{B}^2_{\kappa_{p(t)}} - \mathbb{B}_{\kappa_{p(t)}})\right]\cdot\mathbb{A} = 0,
\end{aligned} \tag{4.25}$$

where for this particular equations for convenience we redefine family of Gordon-Schowalter derivatives to contain derivatives with respect to X by transformation (4.22), i.e., $2\mathbb{D}_X = \left[(\nabla_X \mathbf{V})\mathbb{F}_{\kappa_R}^{-1} + \mathbb{F}_{\kappa_R}^{-T}(\nabla_X \mathbf{V})^T\right]$ and analogically $\mathbb{W}_X$.

ALE method

Let us now derive ALE formulation, following the derivation by Tůma [2014] and extending it for our viscoelastic model. The difference between such formulation and the Lagrangian above is clear. We introduce a new variable deformation $\hat{\mathbf{u}}$ of the mesh which is arbitrary in the domain with the restriction that the deformation is physical on the boundary of the domain. Hence, we identify the mesh with a new configuration κ_χ (domain Ω_χ), see Figure (4.30), and we define mapping $\hat{\chi}$ from κ_χ into κ_t by:

$$\hat{\chi} : \hat{x} \longrightarrow x := \hat{x} + \hat{\mathbf{u}}. \tag{4.26}$$

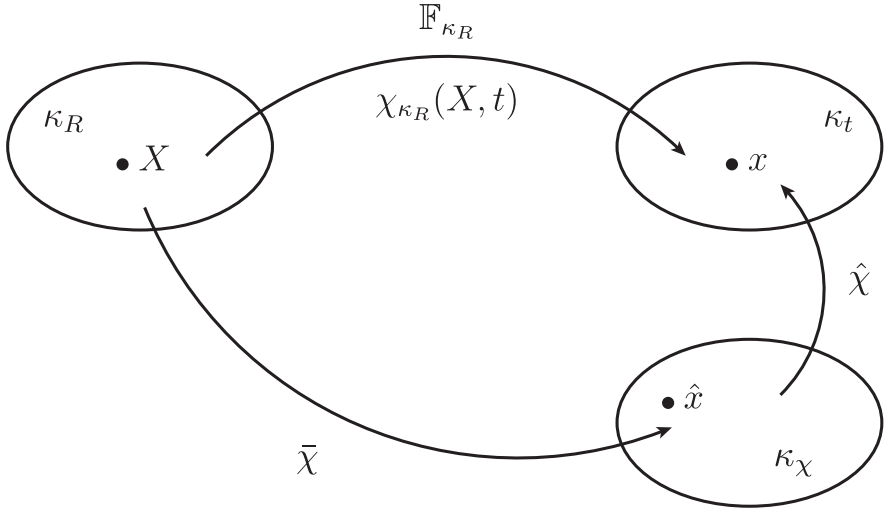

Figure 4.30: Sketch of the reference configuration κ_R and the current configuration κ_t and the ALE configuration κ_χ.

Now we prescribe mesh deformation $\hat{\mathbf{u}}$ in such a way, that the material points are only on the boundary $\partial\Omega_\chi$ and inside the domain we have an arbitrary but unique solution. Notice, that if we choose solution inside the domain such that the derivative of $\hat{\mathbf{u}}$ is equal to the velocity $\mathbf{v}$, then we obtain the Lagrangian formulation. However, we want the solution inside the domain be as simple as possible, hence we choose Laplace equation, and we obtain:

$$\begin{aligned} -\Delta_{\hat{x}}\hat{\mathbf{u}} &= 0 \quad \text{in}\,\Omega_\chi, \\ \frac{\partial\hat{\mathbf{u}}}{\partial t} &= \mathbf{v} \quad \text{on}\,\partial\Omega_\chi. \end{aligned} \tag{4.27}$$

Moreover, we define the deformation gradient $\hat{\mathbb{F}}$ and its Jacobian $\hat{J} = \det\hat{\mathbb{F}}$ by:

$$\hat{\mathbb{F}} := \frac{\partial\hat{\chi}}{\partial\hat{x}} = \mathbb{I} + \nabla_{\hat{x}}\hat{\mathbf{u}}. \tag{4.28}$$

Now, in the same manner as in case of the Lagrangian formulation, we transform the Eulerian weak formulation (3.14) into the ALE. We substitute the velocity gradient:

$$\nabla_{\hat{x}}\mathbf{v} = \frac{\partial\mathbf{v}(t,\hat{\chi}(t,\hat{x}))}{\partial\hat{x}} = \frac{\partial\mathbf{v}(t,x)}{\partial x}\frac{\partial\hat{\chi}}{\partial\hat{x}} = (\nabla\mathbf{v})\hat{\mathbb{F}} \;\Rightarrow\; \nabla\mathbf{v} = (\nabla_{\hat{x}}\mathbf{v})\hat{\mathbb{F}}^{-1}, \tag{4.29}$$

and the material time derivative:

$$\begin{aligned} &\frac{\partial\alpha}{\partial t}\Big|_{\hat{x}} = \frac{d\alpha(\hat{\chi}(t,\hat{x}),t)}{dt}\Big|_{\hat{x}} = \frac{\partial\alpha}{\partial t}\Big|_x + \frac{\partial\alpha}{\partial x}\frac{\partial\hat{\chi}}{\partial t}\Big|_{\hat{x}} = \frac{\partial\alpha}{\partial t}\Big|_x + \frac{\partial\hat{\mathbf{u}}}{\partial t}\cdot\nabla\alpha \quad \Rightarrow \\ &\dot{\alpha} = \frac{\partial\alpha}{\partial t}\Big|_{\hat{x}} + \left(\mathbf{v} - \frac{\partial\hat{\mathbf{u}}}{\partial t}\right)\cdot\nabla\alpha = \frac{\partial\alpha}{\partial t}\Big|_{\hat{x}} + \left[\hat{\mathbb{F}}^{-1}\left(\mathbf{v} - \frac{\partial\hat{\mathbf{u}}}{\partial t}\right)\right]\cdot\nabla_{\hat{x}}\alpha. \end{aligned} \tag{4.30}$$

Finally, using the integral substitution theorem and consequence of Piola identity

(4.24) we obtain:

$$\begin{aligned}
\int_{\Omega_\chi} \hat{J}\mathrm{tr}\left((\nabla_{\hat{x}}\mathbf{v})\hat{\mathbb{F}}^{-1}\right)\psi = 0,\\
\int_{\Omega_\chi} \hat{J}\rho\left[\frac{\partial \mathbf{v}}{\partial t} + (\nabla_{\hat{x}}\mathbf{v})\left(\hat{\mathbb{F}}^{-1}(\mathbf{v} - \frac{\partial \hat{\mathbf{u}}}{\partial t})\right)\right]\cdot\phi + \int_{\Omega_\chi} \hat{J}\hat{\mathbb{T}}\hat{\mathbb{F}}^{-T}\cdot\nabla_{\hat{x}}\phi\\
- \int_{\partial\Omega_\chi} (\hat{J}\hat{\mathbb{T}}\hat{\mathbb{F}}^{-T})\hat{\mathbf{n}}\cdot\phi - \int_{\Omega_\chi}\hat{J}\rho\mathbf{b}\cdot\phi = 0,\\
\hat{\mathbb{T}} = -p\mathbb{I} + 2\nu\mathbb{D}_{\hat{x}} + aG\left[(1-\beta)(\mathbb{B}_{\kappa_{p(t)}} - \mathbb{I}) + \beta(\mathbb{B}^2_{\kappa_{p(t)}} - \mathbb{B}_{\kappa_{p(t)}})\right],\\
\int_{\Omega_\chi} \hat{J}\frac{\delta \mathbb{B}_{\kappa_{p(t)}}}{\delta t}\Big|_{\hat{x}}\cdot\mathbb{A} + \hat{J}\left[\delta_1(\mathbb{B}_{\kappa_{p(t)}} - \mathbb{I}) + \delta_2(\mathbb{B}^2_{\kappa_{p(t)}} - \mathbb{B}_{\kappa_{p(t)}})\right]\cdot\mathbb{A} = 0,\\
\frac{\delta \mathbb{B}_{\kappa_{p(t)}}}{\delta t}\Big|_{\hat{x}} = \frac{\partial \mathbb{B}_{\kappa_{p(t)}}}{\partial t}\Big|_{\hat{x}} + (\nabla_{\hat{x}}\mathbb{B}_{\kappa_{p(t)}})\left(\hat{\mathbb{F}}^{-1}(\mathbf{v} - \frac{\partial \hat{\mathbf{u}}}{\partial t})\right)\\
-a(\mathbb{D}_{\hat{x}}\mathbb{B}_{\kappa_{p(t)}} + \mathbb{B}_{\kappa_{p(t)}}\mathbb{D}_{\hat{x}}) - (\mathbb{W}_{\hat{x}}\mathbb{B}_{\kappa_{p(t)}} - \mathbb{B}_{\kappa_{p(t)}}\mathbb{W}_{\hat{x}}),
\end{aligned} \tag{4.31}$$

where $2\mathbb{D}_{\hat{x}} = \left[(\nabla_{\hat{x}}\mathbf{v})\hat{\mathbb{F}}^{-1} + \hat{\mathbb{F}}^{-T}(\nabla_{\hat{x}}\mathbf{v})^T\right]$ and analogically $\mathbb{W}_{\hat{x}}$. This set of equations is closed by the formal weak formulation of equation (4.27):

$$\int_{\Omega_\chi} \nabla_{\hat{x}}\hat{\mathbf{u}}\cdot\nabla_{\hat{x}}\hat{\mathbf{w}} = 0. \tag{4.32}$$

Nitsche method

As it is not possible to prescribe boundary condition $\partial_t\hat{\mathbf{u}} = \mathbf{v}$ on $\partial\Omega_\chi$ directly in FEniCS, we use the Nitsche method introduced in the work by Nitsche [1971]. We discretize the Laplace equation in time as follows:

$$\begin{aligned}
-\Delta_{\hat{x}}\hat{\mathbf{u}}^{n+1} &= \mathbf{0} \quad \text{in}\,\Omega_\chi,\\
\hat{\mathbf{u}}^{n+1} - g(\mathbf{v}^{n+1}) &= \mathbf{0} \quad \text{on}\,\partial\Omega_\chi,
\end{aligned} \tag{4.33}$$

where $g(\mathbf{v}^{n+1})$ corresponds to the time discretization used. In the case of implicit three-step θ-scheme, which is introduced in the very next section, it reads:

$$g(\mathbf{v}^{new}) = \hat{\mathbf{u}}^{old} + \mathbf{v}^{new}\theta\Delta t^{old}. \tag{4.34}$$

We test the Laplace equation by $\hat{\mathbf{w}}$, integrate it over Ω, and use the Green's theorem. We integrate the Dirichlet boundary condition over $\partial\Omega$, test it by arbitrary test function $\widetilde{\mathbf{w}}$, and we immediately choose $\widetilde{\mathbf{w}} = (\nabla\hat{\mathbf{w}})\mathbf{n}$, which is the anti-symmetric Nitsche method with respect to the second term, which may be found in the work by Burman and Hansbo [2012]. Finally, we sum these equations together, and we add penatly term motivated by the last term. The weak formulation for a discrete FE space without any Dirichlet condition in it then changes as follows:

$$\begin{aligned}
\int_{\Omega_\chi}\nabla_{\hat{x}}\hat{\mathbf{u}}^{n+1}\cdot\nabla_{\hat{x}}\hat{\mathbf{w}} - \int_{\partial\Omega_\chi}(\nabla\hat{\mathbf{u}}^{n+1})\hat{\mathbf{n}}\cdot\hat{\mathbf{w}} + \int_{\partial\Omega_\chi}(\nabla\hat{\mathbf{w}})\hat{\mathbf{n}}\cdot(\hat{\mathbf{u}}^{n+1} - g(\mathbf{v}^{n+1}))\\
+\frac{\beta_{st}}{h_{min}}\int_{\partial\Omega_\chi}(\hat{\mathbf{u}}^{n+1} - g(\mathbf{v}^{n+1}))\cdot\hat{\mathbf{w}} = 0,
\end{aligned} \tag{4.35}$$

where h_{min} is the minimal edge length on the $\partial\Omega_\chi$ and β_{st} is the stabilization coefficient. We choose $\beta_{st} = 1000$.

Implicit Glowinski three-step scheme (GL)

To preserve the volume throughout evolution in time while using ALE method, BE scheme (3.16) turns out to be insufficient, hence one need to use more sophisticated time scheme. It turns out that a good choice is the Implicit Glowinski three-step scheme which is a special choice of the Implicit three-step θ-scheme for $\theta = 1 - 1/\sqrt{2}$:

$$\begin{aligned} &1. \quad \frac{u^{n+\theta}(x) - u^n(x)}{\theta \Delta t^n} + f(u^{n+\theta}(x)) = 0, \\ &2. \quad u^{n+1-\theta}(x) = \frac{1-\theta}{\theta} u^{n+\theta}(x) + \frac{2\theta - 1}{\theta} u^n(x), \\ &3. \quad \frac{u^{n+1}(x) - u^{n+1-\theta}(x)}{\theta \Delta t^n} + f(u^{n+1}(x)) = 0, \end{aligned} \tag{4.36}$$

which consists of two implicit Euler steps and one explicit Euler step. This scheme was proposed by Glowinski [2003], it is conditionally stable and almost a third order scheme.

Model and parameters

For this problem we choose the classical Oldroyd-B model, see Section 4.1.8, and we set $\delta_1 = 1/\,We$, $\delta_2 = 0$, $a = 1$, $\beta = 0$ and $\lambda = 0$. Moreover, we set $G = 0.41/\,We$, $\nu = 0.59$, and $We = 10$.

Numerical results

We compare BE scheme to the GL scheme with various time steps dt on a fine mesh leading to the 203 408 DoFs. We press the material with the constant force for $t < 5.0$ and at $t = 5.0$ we remove the force and let the material relax up to time $t < 100$. At these two times for GL scheme with step $dt = 0.1$, we plot the deformed domain, see Figure (4.31). Moreover, we plot the maximal mesh deformation $\hat{\mathbf{u}}$ over time for all schemes and chosen timesteps, see Figure (4.32) which is the deformation of the top of the rectangle in its middle (point $(Len/2, Wid)$) as can be seen from the previous figure. Finally, we plot ratio of the current volume of the domain $V(t)$ to the referential volume V_{ref} at time $t = 0$, see Figure (4.33). We compute this ratio as follows:

$$\frac{V(t)}{V_{ref}} = \frac{\int_\Omega \hat{J}(t)}{\int_\Omega \hat{J}(0)}. \tag{4.37}$$

Notice, that the GL scheme outpermorfs the BE scheme, hence we recommend to use the GL scheme in the viscoelastic flows with a free surface, especially in the next section about rod-climbing (Weissenberg) effect.

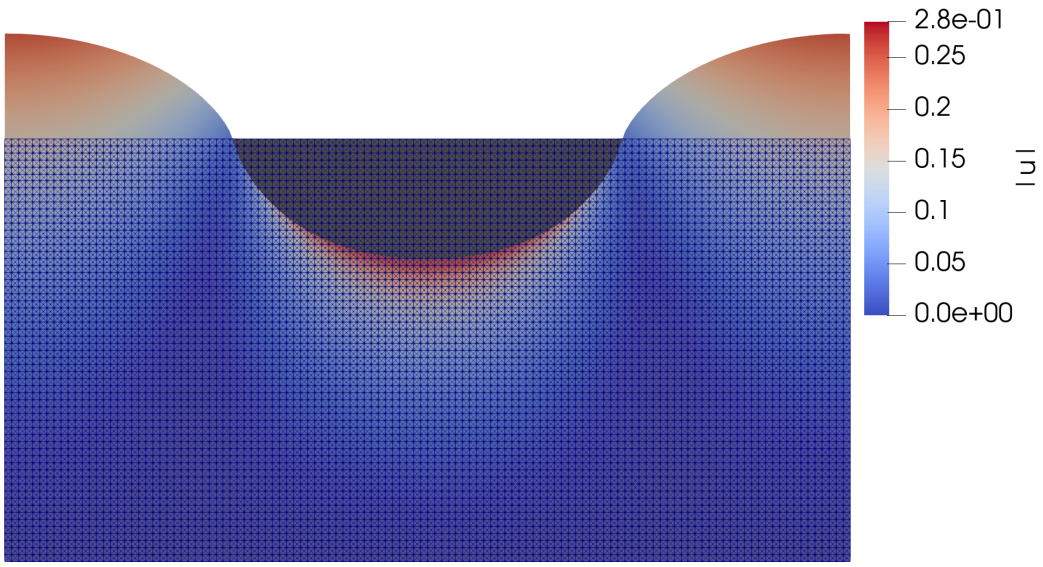

(a) t = 5.

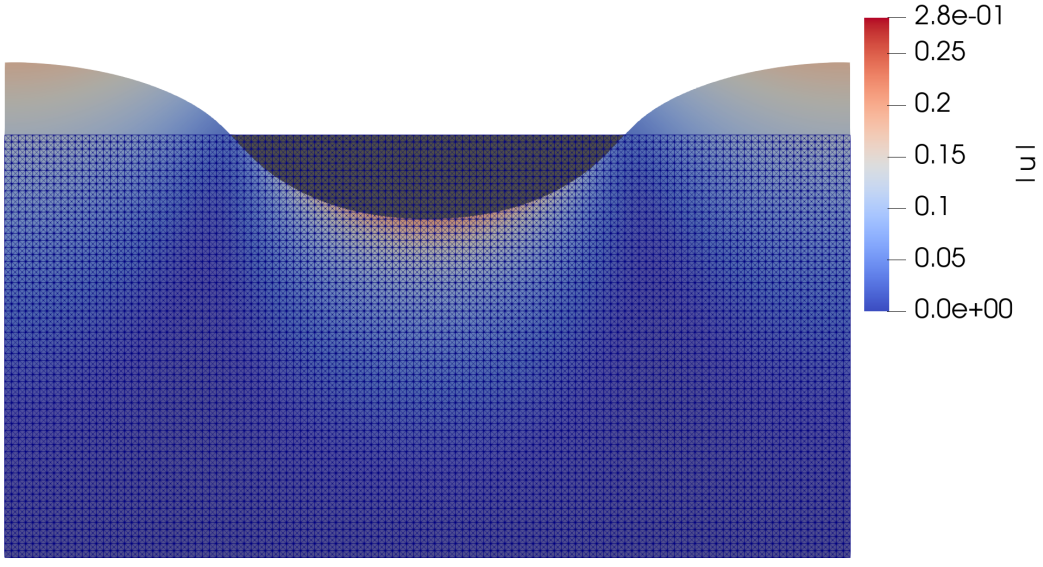

(b) t = 100.

Figure 4.31: Plots of the deformed domain colored by the magnitude of the mesh deformation $\hat{\mathbf{u}}$ in the comparison with domain at t = 0.

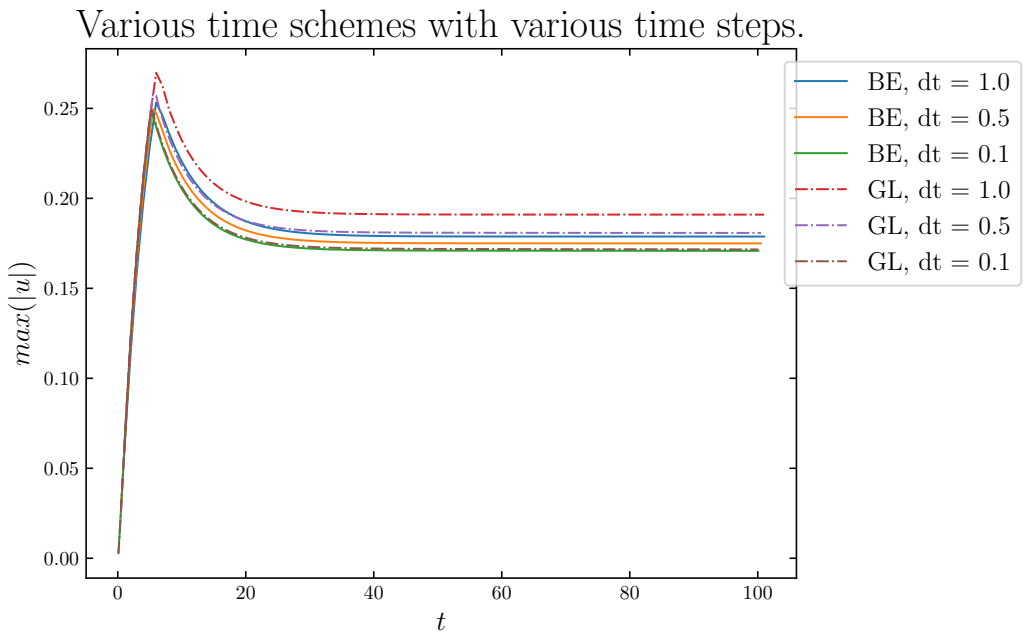

Figure 4.32: Plot of the maximal mesh deformation $\hat{\mathbf{u}}$ over time, i.e., so-called creep test.

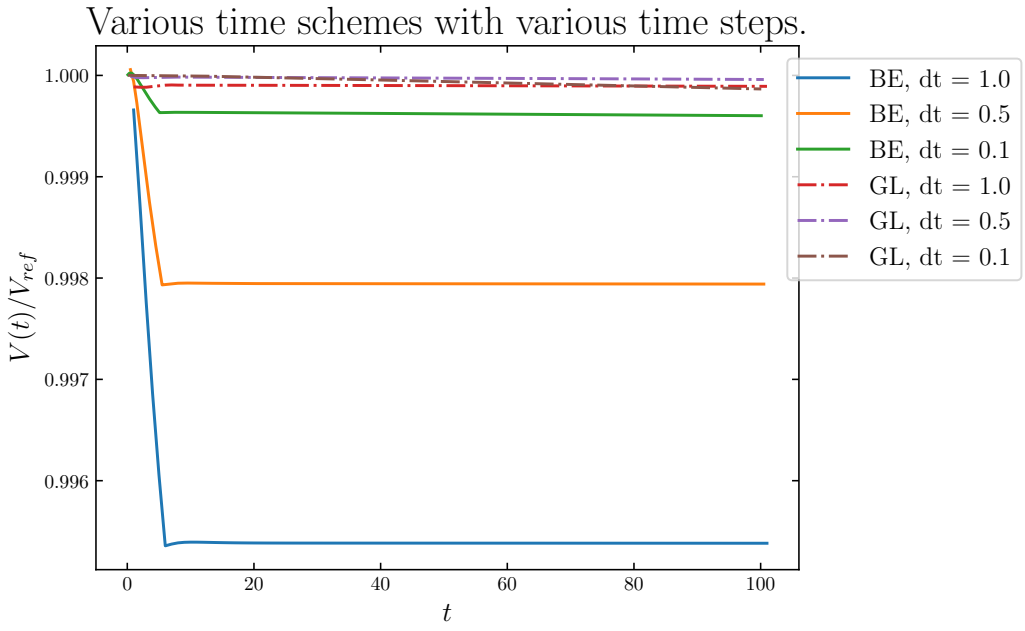

Figure 4.33: Plot of the volume ratio $V(t)/V(0)$ over time. The GL scheme outpermorfs the BE scheme.

4.2.3 Rod climbing (Weissenberg) effect

In this section we simulate the well-known rod climbing effect reduced from 3D to 2D by assumption on axisymmetry. We consider a cylindrical container filled with a viscoelastic fluid with a free surface. As we are intersted in the classical Oldroyd-B model itself, we neglect surface tension. In the center of the container, cylindrical rod is immersed such that it is not touching the bottom of the container. The rod is rotating along its z-axis with given rotations per minute RPM.

The computational domain with its proportions is plotted in the Figure (4.34). As the rod climbing effect is only slightly investigated and there are no clues for the best setting for such effect, we estimate proportions based on the experiment by MIT [2001]. Hence we set $R_{outer} = 5$ cm, $H_{outer} = 5$ cm, $R_{inner} = 1$ cm, $H_{inner} = 3$ cm. We estimate the $RPM = 100$ min^{-1} and we consider outer force $\mathbf{b}$ as the usual homogenous gravity field $\mathbf{g} = (0, 0, -10)$ m·s^{-2}.

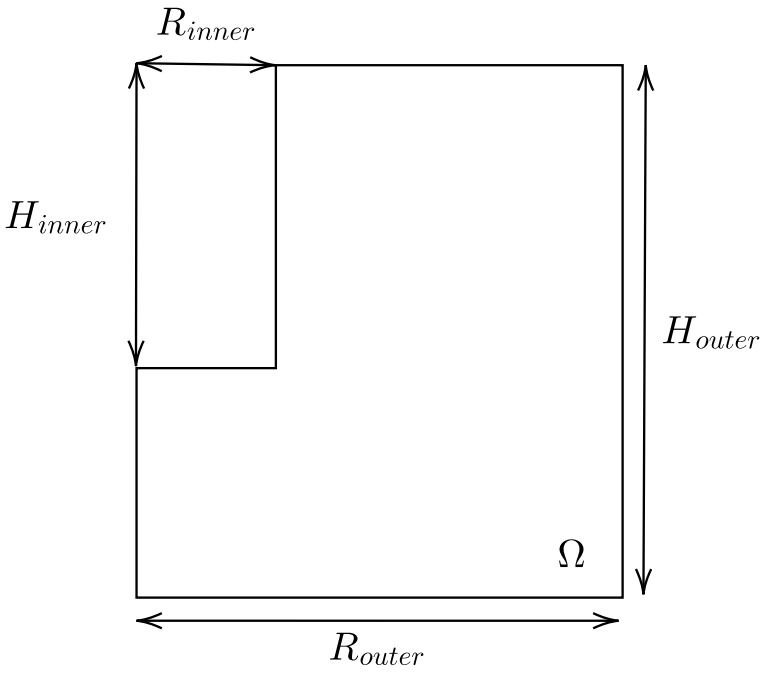

Figure 4.34: Sketch of the computational domain for the rod climbing effect.

Model and parameters

As it was mentioned, for this problem we choose the classical Oldroyd-B model, see Section 4.1.8, hence we set $\delta_1 = 1/We =: 1/\tau$, $\delta_2 = 0$, $a = 1$, $\beta = 0$ and $\lambda = 0$, where τ is the relaxation time. Moreover, we estimate fluid properties as $\rho = 1000$ kg·m^{-3}, $G = 1.0$ Pa, and $\tau = 1.0$ s. Finally, we choose $\nu = 30$ Pa·s which is the value that was used in the MIT experiment.

Weak formulation

We combine techniques tested in the previous sections, i. e., formulation in the cylindrical coordinates and the ALE method with the Nitsche method and the

GL time scheme. The key aspect of combination of the axisymmetric cylindrical coordinates (reduced to 2D) and the ALE method is that the deformation of the mesh in the φ-direction is setted to zero: $\hat{u}_\varphi = 0$. This is due to the fact, that the mesh would be virtually wrapped around the cylinder. And we may set it to zero as the vital component of the ALE method is that only the outter shape of the domain remains physical. Hence we consider the deformation in the form $\hat{\mathbf{u}} = (\hat{u}_r, 0, \hat{u}_z)$, and the weak formulation is the following:

$$
\begin{aligned}
\int_{\Omega_\chi} r\hat{J}\mathrm{tr}\left((\nabla_{\hat{x}}\mathbf{v})\hat{\mathbb{F}}^{-1}\right)\psi = 0,\\
\int_{\Omega_\chi} r\hat{J}\rho\left[\frac{\partial \mathbf{v}}{\partial t} + (\nabla_{\hat{x}}\mathbf{v})\left(\hat{\mathbb{F}}^{-1}\left(\mathbf{v} - \frac{\partial \hat{\mathbf{u}}}{\partial t}\right)\right)\right]\cdot\phi + \int_{\Omega_\chi} r\hat{J}\hat{\mathbb{T}}\hat{\mathbb{F}}^{-T}\cdot\nabla_{\hat{x}}\phi\\
- \int_{\partial\Omega_\chi} r(\hat{J}\hat{\mathbb{T}}\hat{\mathbb{F}}^{-T})\hat{\mathbf{n}}\cdot\phi - \int_{\Omega_\chi} r\hat{J}\rho\mathbf{b}\cdot\phi = 0,\\
\hat{\mathbb{T}} = -p\mathbb{I} + 2\nu\mathbb{D}_{\hat{x}} + aG\left[(1-\beta)(\mathbb{B}_{\kappa_{p(t)}} - \mathbb{I}) + \beta(\mathbb{B}^2_{\kappa_{p(t)}} - \mathbb{B}_{\kappa_{p(t)}})\right],\\
\int_{\Omega_\chi} r\hat{J}\frac{\delta \mathbb{B}_{\kappa_{p(t)}}}{\delta t}\bigg|_{\hat{x}}\cdot\mathbb{A} + \hat{J}\left[\delta_1(\mathbb{B}_{\kappa_{p(t)}} - \mathbb{I}) + \delta_2(\mathbb{B}^2_{\kappa_{p(t)}} - \mathbb{B}_{\kappa_{p(t)}})\right]\cdot\mathbb{A} = 0,\\
\frac{\delta \mathbb{B}_{\kappa_{p(t)}}}{\delta t}\bigg|_{\hat{x}} = \frac{\partial \mathbb{B}_{\kappa_{p(t)}}}{\partial t}\bigg|_{\hat{x}} + (\nabla_{\hat{x}}\mathbb{B}_{\kappa_{p(t)}})\left(\hat{\mathbb{F}}^{-1}\left(\mathbf{v} - \frac{\partial \hat{\mathbf{u}}}{\partial t}\right)\right)\\
-a(\mathbb{D}_{\hat{x}}\mathbb{B}_{\kappa_{p(t)}} + \mathbb{B}_{\kappa_{p(t)}}\mathbb{D}_{\hat{x}}) - (\mathbb{W}_{\hat{x}}\mathbb{B}_{\kappa_{p(t)}} - \mathbb{B}_{\kappa_{p(t)}}\mathbb{W}_{\hat{x}}),\\
\int_{\Omega_\chi} r\nabla_{\hat{x}}\hat{\mathbf{u}}^{n+1}\cdot\nabla_{\hat{x}}\hat{\mathbf{w}} - \int_{\partial\Omega_\chi} r(\nabla\hat{\mathbf{u}}^{n+1})\hat{\mathbf{n}}\cdot\hat{\mathbf{w}} + \int_{\partial\Omega_\chi} r(\nabla\hat{\mathbf{w}})\hat{\mathbf{n}}\cdot(\hat{\mathbf{u}}^{n+1} - g(\mathbf{v}^{n+1}))\\
+\frac{\beta_{st}}{h_{min}}\int_{\partial\Omega_\chi} r(\hat{\mathbf{u}}^{n+1} - g(\mathbf{v}^{n+1}))\cdot\hat{\mathbf{w}} = 0.
\end{aligned}
\tag{4.38}
$$

Here all spatial derivatives are modified to be in the cylindrical polar coordinates, see Section 4.2.1. Also, there is a possibility to prescribe the traction acting on the surface of the domain (surface integral in the balance of momentum), however, it is not used in this simulation. In the last equation, the term $g(\mathbf{v}^{n+1}) = \hat{\mathbf{u}}^n + \mathbf{v}^{n+1}\theta\Delta t^n$, where $\theta = 1 - 1/\sqrt{2}$ for the GL time scheme.

Comments on the extension of the model problem

Note that we may simplify the problem even further and set $\hat{\mathbf{u}} = (0, 0, \hat{u}_z)$ to prevent the mesh from degenerating as it has a tendency to be contracted towards the inner cylinder. However, the experiments suggest that the fluid climbing the rod is prone to bulge in the $r-$direction when it reaches its maximal climbing height. Also, the bulge is usually larger on the top. This cannot be described with $\hat{u}_r = 0$. Moreover, in our computation when the fluid reaches such state, the mesh degenerates in both cases. Hence we recommend to use $\hat{\mathbf{u}} = (\hat{u}_r, 0, \hat{u}_z)$ with remeshig. However, remeshing is not implemented in our scripts.

Also note that the bulging effect might be supported by the surface tension, which is not considered now. This also includes the contact angle boundary condition on the interface of solid rod, viscoelastic fluid and air. We suggest this topic as a future extension of this problem.

Boundary conditions

Container: We assume the mantles of the container to be free-slip in the z-direction. On the mantle we moreover assume no-slip in other directions. On the bottom of the container we assume full no-slip.
Rod: On the surface of the rod we prescribe velocity in the φ-direction based on RPM, i. e., $v_\varphi = 2\pi r \cdot RPM/60$. Moreover, on the mantle we assume zero velocity in the r-direction as the centrifugal force would have to be enormous to tear the liquid away from the rod. And we assume free-slip in the z-direction. On the bottom of the rod we assume zero velocity in the z-direction as the fluid can not penetrate the rod. Furthermore, we assume no-slip condition in the r-direction on the bottom of the rod otherwise computation domain would get destroyed.
Symmetry wall: This is the part of the boundary, that is not present in the full 3D problem and appears with the reduction to 2D. We assume that no fluid may cross this boundary in the r-direction as it would disrupt the assumption of axisymmetry. We also conclude that this part of the boundary lies in the axis of rotation of the rod, hence there is zero velocity in the φ-direction. Finally, we assume free-slip in the z-direction.
Deformation $\hat{\mathbf{u}}$: For all no-slip (zero velocity) condition we prescribe zero deformation on the corresponding boundary parts. Note that there is no $\hat{u}_\varphi$.

Numerical results

We compute on the mesh with 283 047 DoFs with quadruple red-green refinement close the free surface, see Figure 4.36. Results of the numerical experiment are shown in the Figure 4.37. Note that the rod is only postprocessing and is not present during the computation (is cut out). We observe that after transitional period $t > 0.5$ s fluid starts to climb the rod. The fluid reaches the maximal climbing height at $t = 5.0$ s and begins to bulge. At $t = 6.05$ s bulging destroys the mesh and simulation crashes. Note that GL time scheme conserved the volume exceptionally well – up to 8 digits, see Figure 4.35.

Finally, on the same mesh we compute the very same setup for the Navier-Stokes fluid, i. e., we set $G = 0$ Pa. Also we drop the rate-type equation for the left Cauchy-Green tensor $\mathbb{B}_{\kappa_{p(t)}}$, which reduces the number of DoFs to 210 783. Moreover, to magnify the negative rod climbing effect, we set $RPM = 1000\ \text{min}^{-1}$. We observe the expected behaviour, see Figure 4.38.

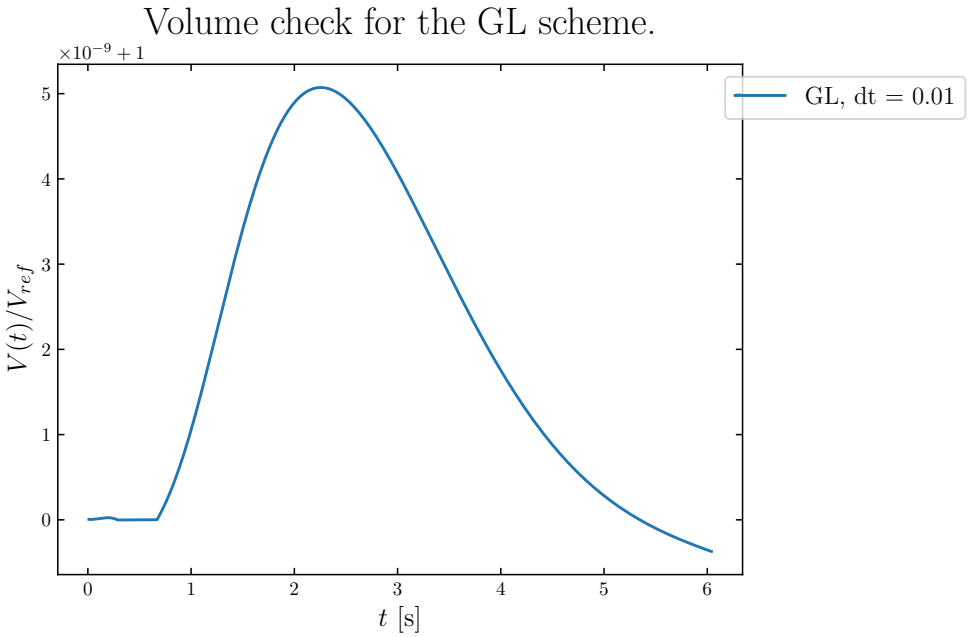

Figure 4.35: Plot of the volume ratio $V(t)/V(0)$ over time. The y-axis is in the range $(1, 1 + 5 \cdot 10^{-9})$.

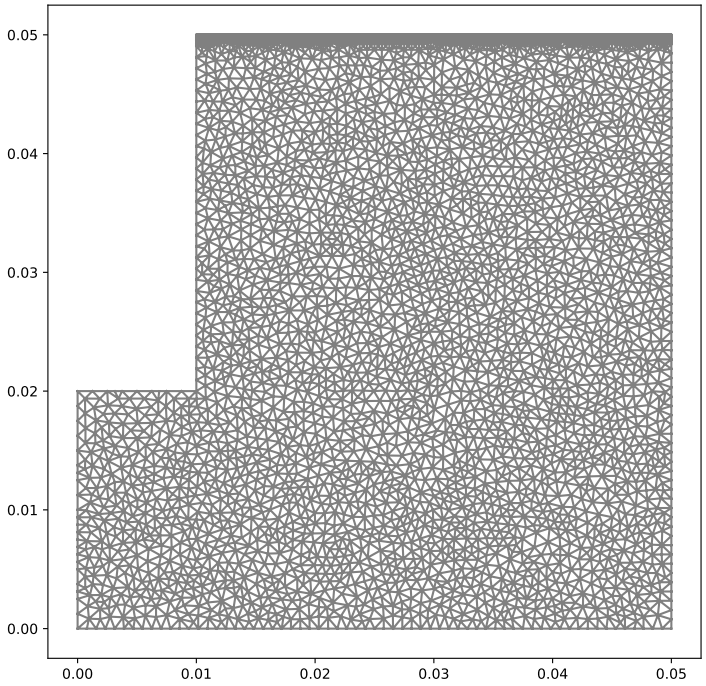

Figure 4.36: Computational mesh for the rod climbing effect with quadruple red-green refinement near the surface leading to the problem with 283 047 DoFs.

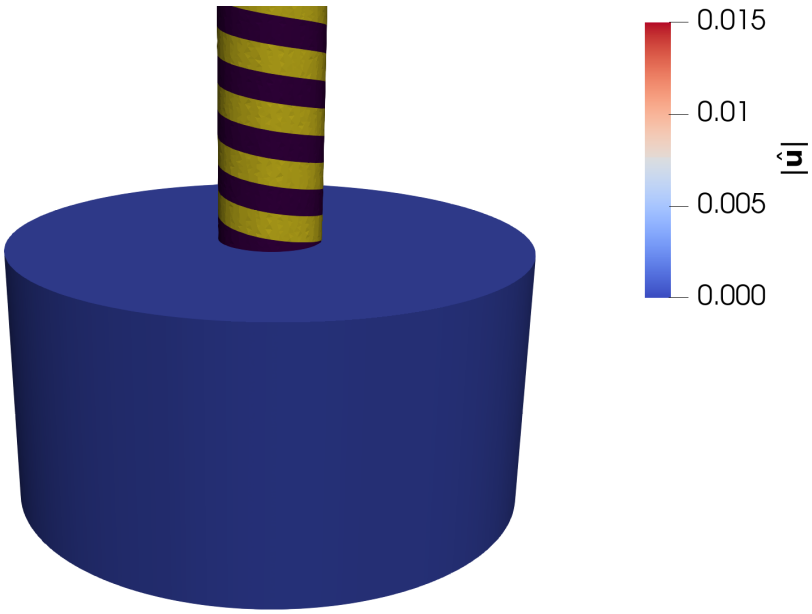

(a) t = 0.01 s.

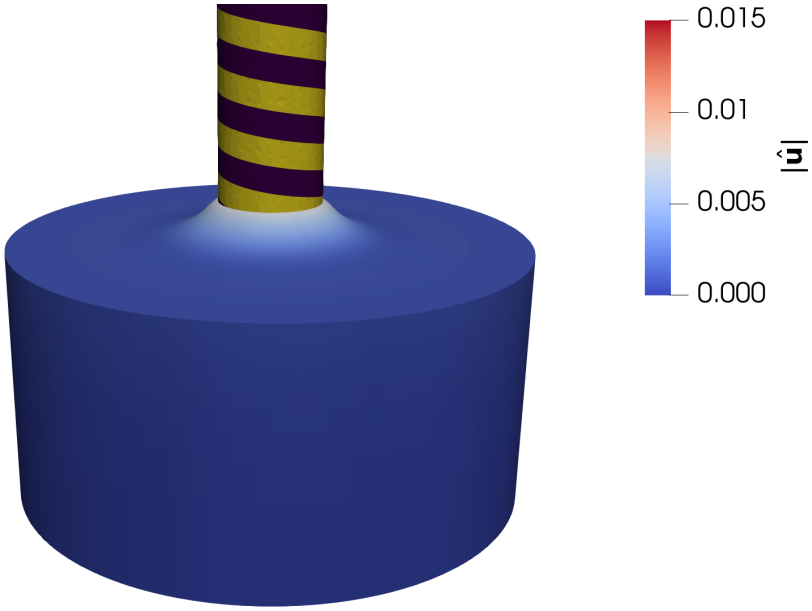

(b) t = 2.00 s.

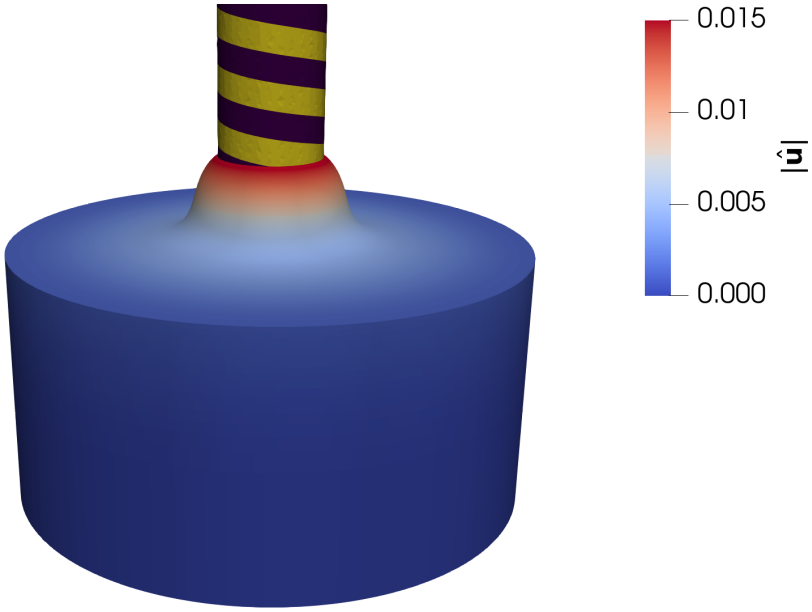

(c) t = 5.00 s.

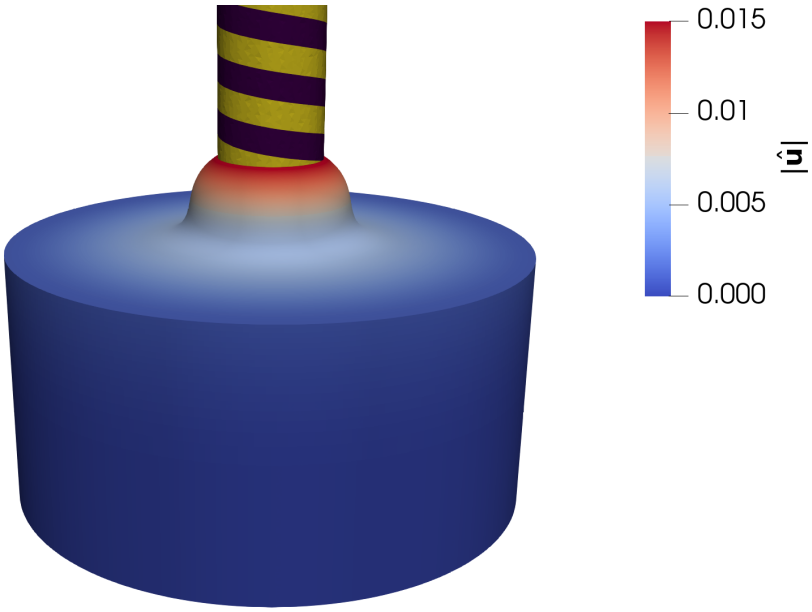

(d) t = 6.05s.

Figure 4.37: Plots of the rotationaly extruded domain colored by the magnitude of the mesh deformation $\hat{\mathbf{u}}$ for the non-Newtonian fluid. The rotating rod was add by postprocessing.

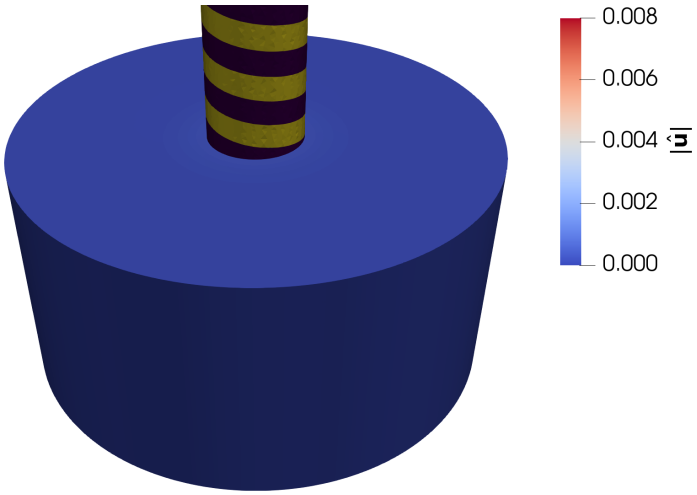

(a) t = 0.01 s.

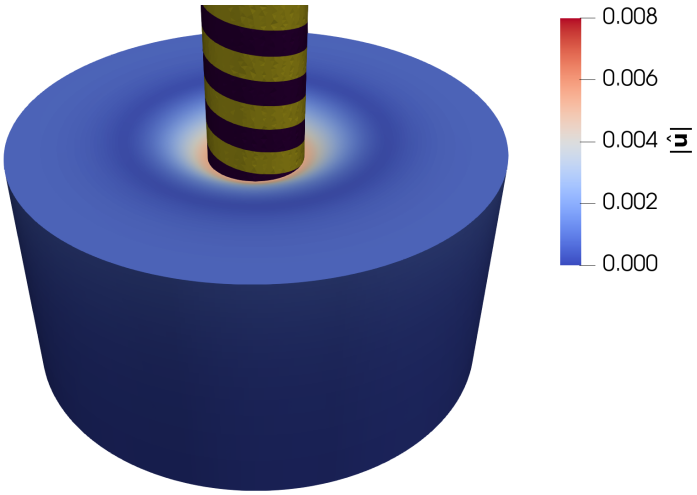

(b) t = 0.25 s.

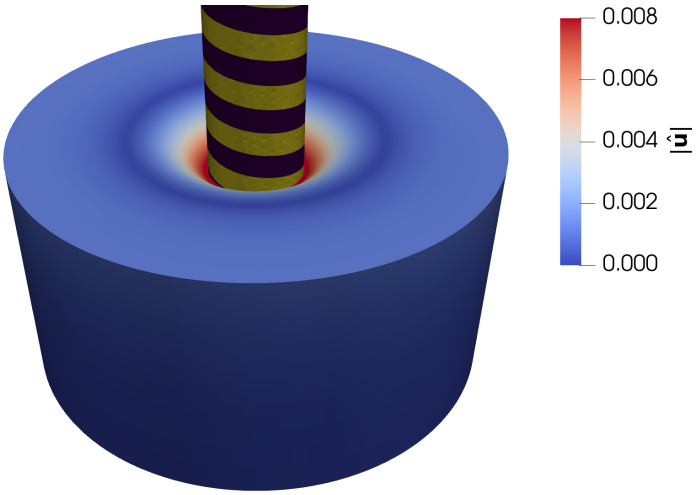

(c) t = 0.50 s.

Figure 4.38: Plots of the rotationaly extruded domain colored by the magnitude of the mesh deformation $\hat{\mathbf{u}}$ for the Newtonian fluid. The rotating rod was add by postprocessing.

Epilog

In this work, we have followed the derivation of viscoelastic models in a consistent thermodynamic framework. We have presented the numerical investigation of the model with the stress diffusion, that was considered as a stabilization in the benchmark of flow past the cylinder. For the stabilization, we have showed that there exists a minimal value of the stabilization coefficient, for which the equations can be solved.

We have chosen several special cases of the model that we investagated closely. We have showed that generalized Giesekus models may be stabilized with the stress diffusion well. Moreover, we have showed that the weak solution existence theory could be expanded for the convex combination of energies (how the fluid stores the energy) up to the ends of the interval, as the numerical results showed smooth transition to these values.

For the generalized Oldroyd-B model, we have observed that the minimal value of the stabilization coefficient grows linearly w. r. t. the Weissenberg number We. This is connected to the fact, that there was growing (w. r. t. We) upstream instability from the cylinder of the flow in the form of vortex. The vortex appeared when the convex combinations of energies contained the quadratic energy, and the growth was faster with the larger contribution of the quadratic energy to the convex combination. Despite the surprising nature of this behavior, it was already experimentally observed for the viscoelastic fluids.

Finally, we have investigated the classical Oldroyd-B model (no quadratic energy) with a different objective derivatives. We have observed that for the Jaumann-Zaremba derivative, there is no viscoelastic extra stress, and we have showed it also analytically in the case of the simple shear flow. The viscoelastic properties appeared with the transition from the Jaumann-Zaremba derivative to the upper convected Oldroyd derivative.

In this work, further, we have presented a method for simulating viscoelastic flows with specific non-Newtonian phenomena, including axisymmetric shear flow, free surface flow, and the rod-climbing (Weissenberg) effect. By using the arbitrary Lagrangian-Eulerian formulation, the non-symmetric stabilized Nitsche method, and the Implicit Glowinski three-step time scheme, we have demonstrated that our method is capable of producing computationally efficient and accurate simulations of these complex flows.

However, our method is currently limited by its tendency to produce mesh degeneration near the fluid surface, which can lead to blow-ups. We suggest that future work could focus on incorporating remeshing techniques to address this issue.

Furthermore, we have shown that our method is robust with respect to the choice of fluid model, as we have successfully simulated Navier-Stokes fluid with the expected results.

As an extension to the current model problem, we suggest adding surface tension, contact boundary conditions for the fluid surface angle, and Navier slip boundary conditions to better capture the behavior of viscoelastic fluids near boundaries.

Finally, we propose that future research could investigate the maximal climb-

ing height and shape of the fluid around a rotating rod, taking into account factors such as the material coefficient, spatial dimensions, and rotation speed. Such investigations could lead to a deeper understanding of the complex behavior of viscoelastic fluids and their applications in various fields.

Bibliography

Non-Newtonian Fluid Dynamics Group, 2001. URL https://nnf.mit.edu/home/billboard/topic-5.

M. Bathory, M. Bulíček, and J. Málek. Large data existence theory for three-dimensional unsteady flows of rate-type viscoelastic fluids with stress diffusion. *Advances in Nonlinear Analysis*, 10(1):501–521, sep 2020. doi: 10.1515/anona-2020-0144. URL https://doi.org/10.1515%2Fanona-2020-0144.

E. Burman and P. Hansbo. Fictitious domain finite element methods using cut elements: II. A stabilized Nitsche method. *Applied Numerical Mathematics*, 62(4):328–341, 2012. ISSN 0168-9274. doi: https://doi.org/10.1016/j.apnum.2011.01.008. URL https://www.sciencedirect.com/science/article/pii/S0168927411000298. Third Chilean Workshop on Numerical Analysis of Partial Differential Equations (WONAPDE 2010).

J. Cach. Numerické srovnání dvou matematických formulací viskoelastického Oldroyd-B modelu, 2021. URL http://hdl.handle.net/20.500.11956/128239.

H. Damanik. FEM Simulation of Non-Isothermal Viscoelastic Fluids. 2011.

H. Damanik, J. Hron, A. Ouazzi, and S. Turek. A monolithic FEM approach for the log-conformation reformulation (LCR) of viscoelastic flow problems. *Journal of Non-Newtonian Fluid Mechanics*, 165:1105–1113, 2010. doi: 10.1016/j.jnnfm.2010.05.008.

M. Dostalík, V. Průša, and K. Tůma. Finite Amplitude Stability of Internal Steady Flows of the Giesekus Viscoelastic Rate-Type Fluid. *Entropy*, 21(12), 2019. ISSN 1099-4300.

Y. Fan, R.I. Tanner, and N. Phan-Thien. Galerkin/Least-Square Finite-Element Methods for Steady Viscoelastic Flows. *Journal of Non-Newtonian Fluid Mechanics*, 84:233–256, 1999. doi: 10.1016/S0377-0257(98)00154-2.

R. Glowinski. Finite element methods for incompressible viscous flow. In *Numerical Methods for Fluids (Part 3)*, volume 9 of *Handbook of Numerical Analysis*, pages 3–1176. Elsevier, 2003. doi: https://doi.org/10.1016/S1570-8659(03)09003-3. URL https://www.sciencedirect.com/science/article/pii/S1570865903090033.

C. Hopkins, S. Haward, and A. Shen. Upstream wall vortices in viscoelastic flow past a cylinder. *Fluids*, 2022. ISSN 1744-683X. doi: 10.1039/D2SM00418F.

S. Kenney, K. Poper, G. Chapagain, and G. Christopher. Large Deborah number flows around confined microfluidic cylinders. *Rheol Acta*, 52:485–497, 05 2013. doi: 10.1007/s00397-013-0712-8.

J. Málek, K. R. Rajagopal, and K. Tůma. On a variant of the Maxwell and Oldroyd-B models within the context of a thermodynamic basis. *International*

Journal of Non-Linear Mechanics, 76:42–47, 2015. doi: 10.1016/j.ijnonlinmec.2015.03.009.

J. Málek, K. R. Rajagopal, and K. Tůma. Derivation of the Variants of the Burgers Model Using a Thermodynamic Approach and Appealing to the Concept of Evolving Natural Configurations. *Fluids*, 3(4), 2018. ISSN 2311-5521. URL https://www.mdpi.com/2311-5521/3/4/69.

J. C. C. Nitsche. Über ein Variationsprinzip zur Lösung von Dirichlet-Problemen bei Verwendung von Teilräumen, die keinen Randbedingungen unterworfen sind. *Abhandlungen aus dem Mathematischen Seminar der Universität Hamburg*, 36:9–15, 1971.

J. G. Oldroyd. On the formulation of rheological equations of state. *Proc. R. Soc. Lond. A200523–541*, 200:523–541, 1950. doi: 10.1098/rspa.1950.0035.

K. R. Rajagopal and A. R. Srinivasa. A thermodynamic frame work for rate type fluid models. *Journal of Non-Newtonian Fluid Mechanics*, 88:207–227, 2000. doi: 10.1016/S0377-0257(99)00023-3.

K. R. Rajagopal and A. R. Srinivasa. On thermomechanical restrictions of continua. *Proc. R. Soc. Lond. A.460631–651*, 88:207–227, 2004. doi: 10.1098/rspa.2002.1111.

X. Shi, S. Kenney, and G. Chapagain. Mechanisms of onset for moderate Mach number instabilities of viscoelastic flows around confined cylinders. *Rheol Acta*, 54, 2015. ISSN 0035-4511. URL https://doi.org/10.1007/s00397-015-0875-6.

K. Tůma. Identification of rate type fluids suitable for modeling geomaterials. 2014. URL http://hdl.handle.net/20.500.11956/67385.

N. Walkington, L. Perrotti, and D. Wang. Numerical approximation of viscoelastic fluids. *ESAIM: Mathematical Modelling and Numerical Analysis*, 51:1119 – 1144, 2016. doi: 10.1051/m2an/2016053.

A.S. Wineman and K.R. Rajagopal. *Mechanical Response of Polymers: An Introduction*. Mechanical Response of Polymers: An Introduction. Cambridge University Press, 2000. ISBN 9780521644099. URL https://books.google.cz/books?id=-FNES-_cowIC.

List of Figures

List of Tables

A. Appendix

A.1 Description of the FEniCS scripts

Following scripts are published in the Charles University Digital Repository, and they are available in public repository:
`https://github.com/cachja/master-thesis`:

Viscoelastic flow past the cylinder

MeshMaker.py: Generates meshes for symmetrical part of the classical benchmark flow past the cylinder.
Oldroyd-B_Giesekus_Combo_MinLambda.py: Provides minimal λ^* for the benchmark of flow past the cylinder using derived vsicoelastic models with the stress diffusion.
Oldroyd-B_Giesekus_Combo.py: Provides results for given λ for the benchmark of flow past the cylinder using derived viscoelastic models with the stress diffusion.

Viscoelastic axisymmetric problems and with a free surface

AxisymmetricShearFlow.py: Solves the axisymmetric shear flow problem for a viscoelastic fluid described by the classical Giesekus model.
ViscoelasticPush_time-study.py: Solves pressing of a rectangular piece of viscoelastic fluid with a free surface and gives data on volume preservation for different time schemes ((GL) and (BE)) and timesteps.
RodClimbing.py: Solves Rod Climbing (Weissenberg) problem for the classical Oldroyd-B model, but any convex combination of Oldroyd-B and Giesekus model with the stress diffusion is possible.

A.2 An experimental proof on viscoelastic instabilities upstream in front of the cylinder

Following figures are taken directly from an experimental papers and they demonstrate viscoelastic flow instabilities in microfluidic flow past the cylinder upstream in front of the cylinder.

In the work by Kenney et al. [2013] they show vortex forming upstream in front of the cylinder w. r. t. growing Deborah number De (which is the ratio of a solution's relaxation time to residence time in the flow) with fixed elasticity number El (which is the ratio of elastic to inertial stresses independent of kinematic processes), see Figure A.2. Their definitions of dimensionless numbers are following: $De = \tau U/R$, $We = \tau U/(Wid - 2R)$, $Re = \rho U 2R/\mu$, $El = We/Re$, where τ is the relaxation time, μ is the dynamic viscocity, ρ is the density, R is the radius of the cylinder in the channel, Wid is the width of the channel and U is the characteristic velocity on the inflow.

In the work by Hopkins et al. [2022] they observe the same result in a slightly different experimental setup (height of the channel in z-direction is many times

larger). They also observe non-symmetric solution, see Figure A.1. They denoted by BR the blockage ratio $BR = 2R/Wid$, where they denote by Wid the width of the whole channel, and $Wi = We$.

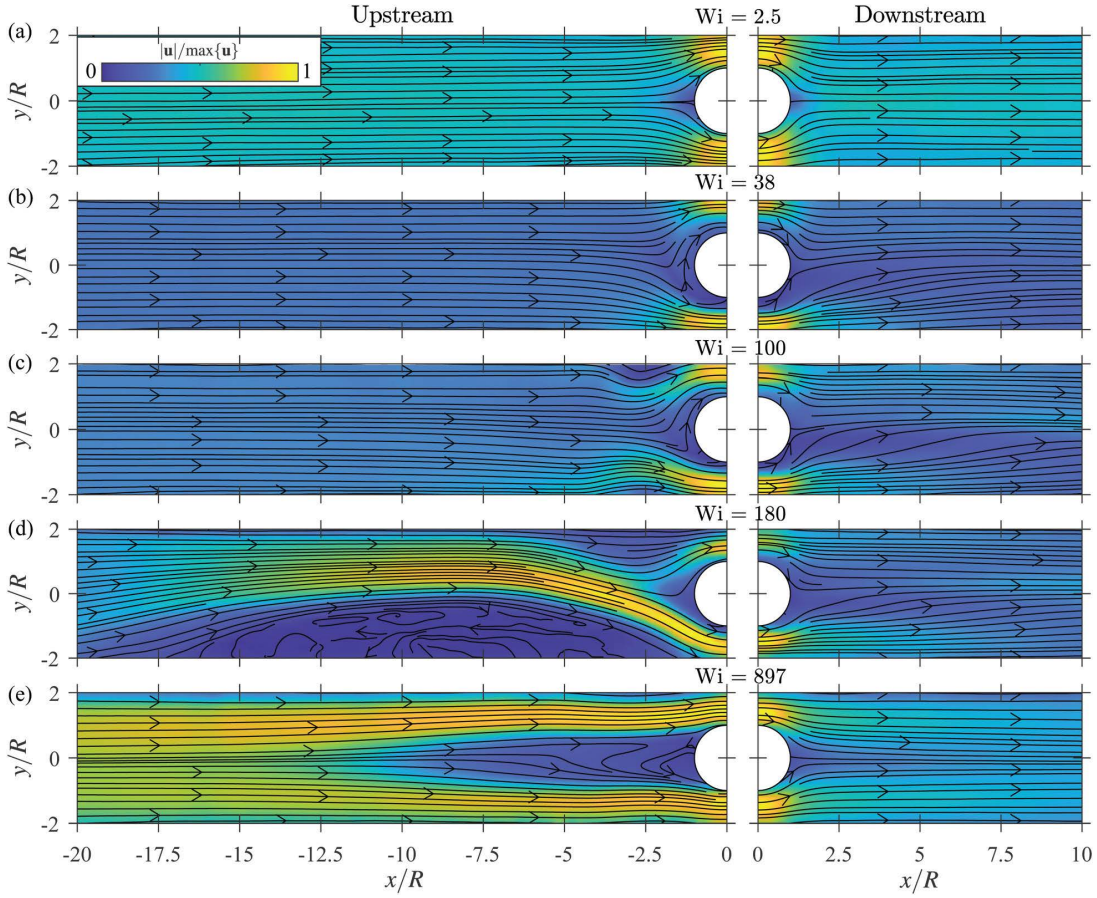

Figure A.1: Time-averaged velocity fields measured for flow of the wormlike micellar solution past a $BR = 0.5$ cylinder at (a) $Wi = 2.5$, (b) $Wi = 38$, (c) $Wi = 100$, (d) $Wi = 180$, (e) $Wi = 897$. The velocity fields are normalized by the maximum velocity in each respective case. Upstream and downstream velocity fields were measured in separate non-coincident experiments and are thus presented separately. Courtesy of Hopkins et al. [2022].

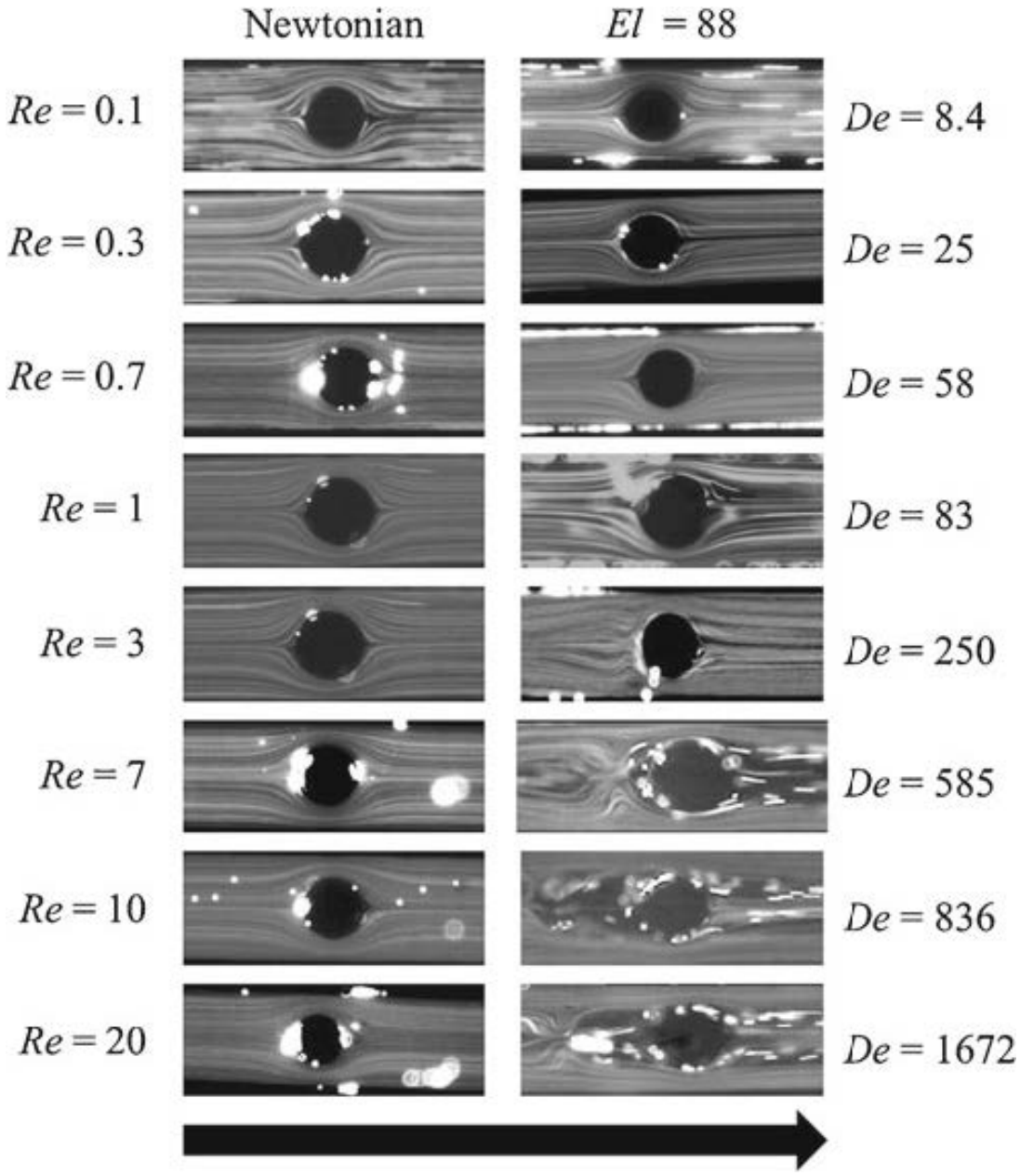

Figure A.2: Flow patterns for Newtonian control and $El = 88$ Boger fluid. Re on the left applies to both the Newtonian and $El = 88$ flows; De on the right only applies to $El = 88$. Values of Re and De are typical of experimental work conducted. Streakline images represent typical results from a given flow condition. All images here are shown at $\times 20$ magnification, but each image was taken at a frame rate necessary to accurately capture flow phenomenon. These frame rates varied from 10 fps to as high as 2,000 fps. Arrow indicates flow direction. Courtesy of Kenney et al. [2013].